1-1-2002

Miktoarm star block copolymers : effects of molecular architecture on morphology.

Lizhang, Yang

University of Massachusetts Amherst

MIKTOARM STAR BLOCK COPOLYMERS:

EFFECTS OF MOLECULAR ARCHITECTURE ON MORPHOLOGY

A Dissertation Presented

by

LIZHANG YANG

Submitted to the Graduate School of the
University of Massachusetts Amherst in partial fulfillment
of the requirements for the degree of

DOCTOR OF PHILOSOPHY

February 2002

Polymer Science and Engineering

MIKTOARM STAR BLOCK COPOLYMERS:
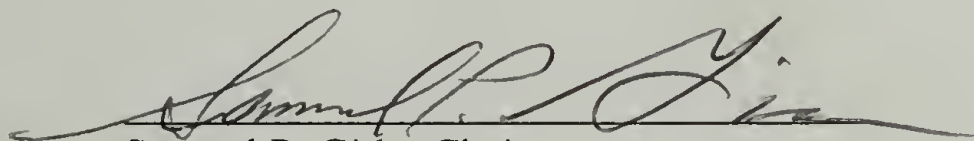
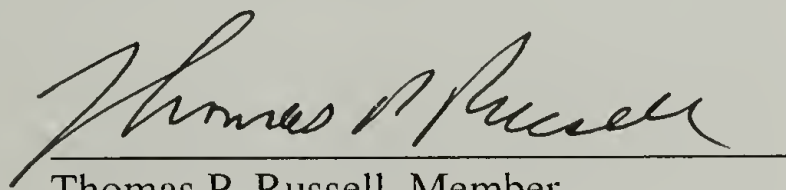EFFECTS OF MOLECULAR ARCHITECTURE ON MORPHOLOGY

A Dissertation Presented

by

LIZHANG YANG

Approved as to style and content by:

_____

Samuel P. Gido, Chair

_____

Thomas P. Russell, Member

_____

H. Henning Winter, Member

_____

Thomas J. McCarthy, Head
Polymer Science & Engineering

To my parents, Xi-yuan Yang and Cheng-rong Yan,

for their love and support.

ACKNOWLEDGEMENTS

It is such a pleasure and privilege to work in this department. Darrin, Chin, and Rick helped me on the initial stages of my research; Sheng gave me many excellent suggestions. Louis helped me greatly on Microscopy support; John helped me design and construct Roll Caster; Eileen, Sophia, and many other secretaries make the life around us easy. The janitors keep the place neat and clear. It is so enjoyable to work in such a place.

Finally and certainly not least among my academic colleagues, I am indebted to my dissertation advisor, Prof. Samuel P. Gido. Without doubt I have learned much from Sam, sometimes not of my choice, but always to my advantage. Sam has taught me much about scientific research, block copolymers, and the many practical matters, which will surely serve me well in the future.

I have been lucky to count many among my friends during the last four years, but a handful of these I know will be pestering me for years to come. Sheng helped me keep the sanity as we "compliment" each other. Susan, Lisa and John helped me to learn how difficult English can be. Xiaodong, Yong, and Chuntao showed me how much fun Poker Games could be in a hot summer evening. Tao Xie has been great for showing me how colorful life is in Umass. Kunlun, David, and Jinchun taught me the how versatile glasses were. True friends are rare, and I am fortunate to have so many.

To my family, I owe a debt I cannot express much less repay. Without fail, they have always been supportive of my academic undertakings; my success has been a family project from cradle through the current stage. Especially, I want to thank my great grant

father, Shi-gui Yang. He was a wise man and valued education. He sent children to school despite all the difficulties. His third son was the first university graduate in my hometown; my father was the second; and I am becoming the first Ph.D. of the town.

Finally, I would like to thank my wife Xiao Xie. Her love is true blessing having no explanation nor requiring one. Our relationship has become the foundation on which I've stood during the past five years. Her love has made me a better person, and that may be the best result of my time in graduate school.

ABSTRACT

MIKTOARM STAR BLOCK COPOLYMERS:

EFFECTS OF MOLECULAR ARCHITECTURE ON MORPHOLOGY

FEBRUARY 2002

LIZHANG YANG, B.S., BEIJING UNIVERSITY

M.S., UNIVERSITY OF MASSACHUSETTS AMHERST

PH.D., UNIVERSITY OF MASSACHUSETTS AMHERST

Directed by: Professor Samuel P. Gido

Three aspects of the effects of molecular architecture on block copolymer and block copolymer / homopolymer blends morphological behavior have been investigated. In the Chapter 2 and 3, the morphological behaviors of "Model" graft block copolymer / homopolymer blends was discussed. The morphological behaviors for two distinct types of graft architectures were investigated. The first type, I_2S block copolymers, which have 2 low polydispersity (PDI) polyisoprene arms and one low PDI polystyrene arm joint at a single junction point, has an asymmetry, non-linear molecular architecture. The second type, I_2S_2 block copolymers, which have 2 low PDI polyisoprene arms and two low PDI polystyrene arms joint at a single junction point, has a symmetry, non-linear molecular architecture. In the blend study, a slow co-casting procedure was developed to get single crystal structure of Gyroid morphology. The amazing scattering patterns of this sample provide the best evidence for Gyroid morphology observed so far.

In Chapter 4, morphological behavior of I_5S block copolymers was studied to investigate the systematic discrepancies between the theoretical predicated *miktoarm* star block copolymer morphology and the experimental observations. The current results indicate that geometrical packing constraints prevent the formation of morphologies such as spheres and cylinders in highly asymmetric miktoarm stars in which the minor volume fraction component would need to occupy the matrix phase. Unusual *broken chevron* tilt grain boundary morphologies were also observed in a lamellar I_5S material. We attribute these new structures to the asymmetric energy penalties for interfacial bending which result from the molecular asymmetry of the miktoarm stars.

Finally, irreversible morphology transformation from lamella to cylinder was investigated using selective solvent approach. Selective solvent can preferentially swell one of the components of block copolymers, increase the effective volume fraction of that component during solvent casting and thus affect the resulting block copolymer morphology. During the subsequent annealing, the kinetically trapped unstable morphology will transform to its stable morphology. By controlling the annealing temperature and the length of annealing time, we will be able to tract the detailed information about the morphology transformations.

TABLE OF CONTENTS

LIST OF TABLES

LIST OF FIGURES

CHAPTER 1

INTRODUCTION

1.1   Miktoarm Stars

Study of the morphological behavior of block copolymers with non-linear, grafted architectures has been extensive over the last seven years.[1-10] This work originated in part from an interest in finding new ways to control the formation of block copolymer mesophases other than by variations in temperature and relative volume fractions of the component materials.[2] Results of an early study examining the morphological behavior of a limited set of A_nB_m–type stars indicated that molecular architecture could significantly affect morphological behavior.[1] Figure 1.1 illustrates a model A_nB_m-type block copolymer, in this case having $n = 3$ and $m = 2$. This work was facilitated by developments in chlorosilane chemistry techniques, which allowed the coupling of blocks of living polymers in new ways.[1]

In 1994, Milner presented a mean-field model predicting the combined effects of architectural asymmetry, a difference in the number of arms of components A and B, and conformational asymmetry, the difference in space-filling characteristics of components A and B, on the morphological behavior of A_nB_m-type stars.[11] This work provided a guide to experimentally examine the morphological behavior of these materials, named "miktoarm" stars by Hadjichristidis. Miktoarm is a combination of the Greek μικτοσ, meaning "mixed", and arm. Both miktoarm star and A_nB_m-type star will be used through out this work to refer to block copolymers with this architecture.

1

The Milner model was relatively successful in predicting the morphological behavior of miktoarm stars with relatively low architecture asymmetry.[2,9,12] However, samples with relatively high architecture asymmetry were found to exhibit morphological behaviors differing from the predictions of the Milner model.[8] These discrepancies are shown in Figure 1.2. These discrepancies suggested that while the model correctly predicted the basic effects of architecture on morphological behavior, the specific details of the miktoarm star molecular architecture and its impact on morphology might not be properly described. The previous experimental studies at high asymmetry parameter did not indicate the morphology transformation volume fractions. Thus, a further study with high molecular asymmetry miktoarm stars to show exact morphology transformation is important, so that we will be able to see the degree of agreement between the theoretically calculated morphology diagram with the experimental data, and find the reasons for the observed discrepancies.

1.2 "Model" Graft Stars block copolymer / homopolymer blends

Linear diblock copolymer / homopolymer blends and linear multi block copolymer / homopolymer blends systems have been extensively studied.[13-25] Previously reported linear diblock copolymer / homopolymer blend results showed that the OOTs in the blends occur at about the same volume fractions as those of pure linear diblock copolymers.[17,18,20] However, for architecturally asymmetric graft copolymers, blending homopolymer into the one arm side or into the multi-arm side of the interface may produce different morphological results. For architecturally symmetric yet non-linear

2

star shaped block copolymers, blending homopolymer may not produce the same morphological behavior as that of linear block copolymers. In the present study, I_2S block copolymers and I_2S_2 block copolymers are blended with homopolymers of polystyrene (PS) or homopolymer polyisoprene (PI) to investigate their morphological behaviors. Blends of graft block copolymers and homopolymers are used widely in industrial applications where graft copolymers are used as compatibilizers to control the microphase separated morphology and thus the properties of blends.[26-30] The complex graft block copolymers can be viewed as a combination of their structure units, which are usually A_2B_2 and A_2B.[31] Therefore, it important to investigate to blends behavior of "model" A_2B, A_2B_2 star shaped lock copolymer homopolymer blends.

1.3 Block copolymer morphology transformations

Despite considerable interest in equilibrium diblock copolymer phase behaviors, the mechanisms of transitions between different morphologies have received comparatively little attention. However, an understanding of morphology transformation processes has implications for practical of morphology control. Both experimental and theoretical data indicate that in the vicinity of the order-disorder transition, phase boundaries acquire significant curvature in the composition (f) -segregation (χN) plane, and the system becomes thermotropic due to the temperature dependence of χ. This kind of heat transformation is usually thermal reversible and has been the focus of many recent studies.[32-40] The schematic of this kind of transformations are shown in Figure 1.3. Since temperature can only affects χN in a certain range, low molecular weight block

copolymers are usually used, and these low MW polymers have fast kinetics at elevated temperatures. Temperature affects both morphology and the kinetics, making it difficult to deconvolute these two factors. At high χN value, order-order transition phase boundaries become nearly independent of segregation. In this regime, non-equilibrium morphologies can be prepared though casting from a selective solvent and their relaxation can be followed. The schematic is also shown in Figure 1.3. Selective solvent can preferentially swell one of the components of block copolymers, increase the effective volume fraction of that component during solvent casting and thus affect the resulting block copolymer morphology. During the subsequent annealing, the kinetically trapped unstable morphology will transform to its stable morphology. By controlling the annealing temperature and the length of annealing time, the detailed information about the morphology transformations can be tracked. This kind of morphology transformation is not reversible. Comparing with heat transformations, selective solvent approach to study morphology has many advantages: First, higher molecular weight polymers can be used; Second, wider range of molecular composition can be used, since we can adjust the effective volume fraction of the system by choosing different selective solvents; Third, at these high χN range, the order-order transition is nearly unaffected by changes in segregation, and temperature only affects the kinetics, thus deconvolute kinetics and thermodynamics is not necessary; Finally, it is also possible to get accurate information about morphology-property relationships, since different morphologies can be achieved from the same material and high MW polymer, which is a requirement for many mechanical testing, can be used.

4

1.4   Background

The following sections are offered as a brief introduction to the basic principles applied in this dissertation. The reader is advised to refer to the cited references for a more complete discussion of these topics.

1.4.1   Self-Assembly of Linear Diblock Copolymers

The mechanism for self-assembly of linear (AB) diblocks into ordered mesophases derives from the basic tendency of immiscible systems to phase separate when unfavorable enthalpic interactions overcome the entropic benefits of mixing.[41] In block copolymers, however, the joining of immiscible blocks into one molecule prevents conventional, macroscopic phase separation. Instead, the driving force to minimize unfavorable A-B contacts produces a system that forms mesomorphic structures on the nanoscopic level.[42,43]

A variety of interesting morphologies are formed when block copolymers self-assemble. These include alternating lamellae of A and B, cylinders of one component in a matrix of the other, and spheres of one component in a matrix of the other. Other morphologies that have been observed include cubic bicontinuous morphologies, perforated lamellae, and undulating lamellae.

A microphase separated, bicontinuous, block copolymer structure with a cubic symmetry was identified as ordered bicontinuous double diamond (OBDD) with Pn3m symmetry by Thomas and coworkers,[44] and the Hashimoto group,[45] in the mid-1980's. In

1994, Thomas and co-workers[46] and Bates and co-workers[38] amended the structure of the cubic bicontinuous morphology, proposing that it was actually a gyroid structure with $Ia\bar{3}d$ symmetry. SAXS evidence for the gyroid structure was provided by powder patterns with up to 13 reflections,[38] and single crystal scattering patterns with up to 10 reflections.[37-39,47]

Hexagonally perforated lamellae, which resemble the cantenoid-lamellar structure derived by periodic area-minimizing surfaces calculations,[48] were also observed recently in linear diblock systems[35,37-39,46,49-52] in a narrow volume fraction region between HEX and LAM and in block copolymer / homopolymer blends.[22,53,54] Controversy exists regarding some structure details of the perforated lamella structure and the stability of the morphology. Both ABC stacking of the hexagonally perforated layers[38,52] and a combination of an ABC and AB stacking[39] were suggested for the perforated lamellar morphology. The experimental studies by Hajduk *et.al.* suggest that perforated lamella is an unstable morphology involved in lamella to Gyroid transition. However, in a recent study by Yang, Gido and coworkers, perforated lamella was observed in a solvent cast blend sample of graft block copolymer and homopolymer, and the morphology persisted during thermal annealing. These observations suggest that perforated lamella can be stable or meta-stable. Using the methods of Semenov[55] to estimate the free energy of perforated lamella in the strong segregation limit, Fredrickson[56] showed that the perforated lamella is metastable with respect of cylinders and lamella at $\phi=0.35$. Qi and Wang[57-59] showed that the perforated lamellae appear as a "pseudostable" morphology

during the lamellar to cylinder transition. However, this prediction has not been proved experimentally.

The selection of morphology is based simply on the free energy of the system. The total free energy of a block copolymer system which has microphase separated is a sum of competing effects, the energy required to create a surface between microphase separated domains, and the energy resulting from the stretching of the polymer chains away from the newly formed interface.

Figure 1.4 shows a morphology diagram calculated by Matsen and Bates.[60] This diagram predicts AB diblock copolymer morphology as a function of f, the relative volume fraction of one component of an AB diblock copolymer, and the product χN, where χ is the Flory-Huggins binary segmental interaction parameter[61] and N is the total degree of polymerization of the block copolymer. Polymers A and B in this case have identical conformational behavior, leading to a morphology diagram symmetric about $f = 0.5$. This morphology diagram reflects the results of nearly 30 years of both theoretical and experimental work toward understanding the morphological behavior of block copolymers, beginning with a model proposed by Helfand,[62-72] and with significant refinements by Leibler[73] and Semenov.[55] It predicts the formation of the "classical" morphologies, alternating lamellae (L), hexagonally packed cylinders (H), spheres (Q_{Im3m}) on a body-centered cubic (BCC) lattice, as well as more complicated morphologies such as the "gyroid" cubic bicontinuous morphology (Q_{Ia3d}).[46,74] Below a critical level of $\chi N = 10.5$ for a block copolymer with equal volume fractions of A and B, a diblock copolymer is predicted to form a homogenous, disordered morphology.

7

Three regimes in Figure 1.4 are commonly defined. These are the weak segregation regime (WSR), the intermediate segregation regime (ISR), and the strong segregation regime (SSR). The divisions between these regimes are based on the change in scaling behavior of mesophase period with degree of polymerization.[43] Typically, the WSR is defined by $\chi N < 15$, the ISR by $15 < \chi N < 100$, and the SSR by $\chi N > 100$. For the purposes of most block copolymer morphology studies, samples that fall in the SSR are preferred as their behavior has been most extensively modeled and examined. In the SSR, the interface between the microphase-separated domains is a sharp division between essentially pure domains of components A and B. This condition, utilized by Helfand as the narrow interphase approximation[69] is only possible when the unfavorable enthalpic interactions dominate the free energy of the system, such as occurs at high χN.

1.4.2 The Milner Model

Microphase separated block copolymers have been successfully represented as polymer brushes grafted to the dividing surface between mesophases[11,75-82] The model proposed by Milner applies these arguments to construct a self-consistent, mean-field theory for miktoarm star morphological behavior[11,83] The free energy of a mesophase is calculated for a single molecule confined in a wedge representing the Wigner-Seitz unit cell for each morphology,[72] and is the sum of the interfacial energy required to create the interface between microphase separated domains of A and B, and the stretching energy resulting from the incompressibility boundary condition for a bulk polymer.

The shape of the wedge is determined by the mesophase, as illustrated in Figure 1.5. The height of the wedge is the radius of the round unit cell. The location of the dividing surface between microphase separated A and B domains is shown as a shaded plane. Wedge height is determined by a technique developed for polymer brushes, and is limited only by the number of chains confined to the wedge at a given surface density (chains per unit area). Chains are added incrementally until the appropriate number is present on each side of the wedge. The height of the interface determines the surface area of the interface, and is governed by the conformational properties of the constituent materials. Such round unit cell models are recognized as giving non-physical results in certain limits[55] but are successful in predicting general behavior.

The stretching free energy contribution to the free energy is also determined using models developed for polymer brushes. The chain ends for each arm of the star are assumed to be found at any distance from the dividing surface within the wedge. This assumption justifies use of a quadratic chemical potential function with distance from the interface[76,77] To calculate the stretching energy, chemical potential is integrated with respect to interface surface area.

Combining the stretching free energy component with the interfacial free energy term yields a set of equations giving free energy for the four morphologies considered, lamellae, hexagonal cylinders, BCC spheres, and the ordered, bicontinuous double-diamond (OBDD) morphology.[44] These are given as equations 1, 2, and 3,

$$\frac{f_{lam}}{f_0} = \left[\varepsilon(1-\phi) + \frac{\phi}{\varepsilon} \right]^{1/3} \qquad (1)$$

9

$$\frac{f_{cyl}}{f_0} = \left[\frac{2\varepsilon\phi(1-\phi^{1/3})^3(3+\phi^{1/2})}{(1-\phi)^2} + \frac{2\phi}{\varepsilon} \right]^{1/3} \qquad (2)$$

$$\frac{f_{sph}}{f_0} = \left[\frac{27\varepsilon\phi^{4/3}(1-\phi^{1/3})^3(\phi^{2/3}+3\phi^{1/3}+6)}{10(1-\phi)^2} + \frac{27\phi}{10\varepsilon} \right]^{1/3} \qquad (3)$$

where f is free energy, f_0 is the free energy of a lamellar morphology for a sample with 50 volume % of each component, ϕ is the volume fraction of the minority component, and ε is a unified molecular asymmetry parameter describing the architectural and conformational characteristics of the molecule. An analytical solution in terms of f and ε for the OBDD morphology is not possible; free energy must be calculated numerically in this case.

Milner's model in fact finds the OBDD morphology to be unstable.[11,83,84] Recent work by Matsen and Bates has verified this result, and attributes the instability of both the OBDD and the gyroid morphologies to packing frustration[60,85,86] arising from a combination of the confinement of the block copolymer junction point to the interface between A and B domains, and the incompressibility boundary condition. The geometries of the gyroid and OBDD morphologies are such that for the polymers to fill space as required, the junction point between blocks must deviate from its preferred position at the interface. This raises the total free energy of the morphology, and makes it unstable when the penalty for this deviation is great (in the SSR). The solution for the OBDD phase in the Milner model is multiplied by a small constant prefactor (0.99) to generate a window of stability.

Figure 1.6 shows the morphology diagram generated using the Milner model, including the unstable OBDD phase. Morphology is given for A_nB_m stars characterized by volume fraction, ϕ_B, and the unified molecular asymmetry, ε. The molecular asymmetry parameter, ε, combines architectural asymmetry, the difference in number of arms of components A and B, with conformational asymmetry, the disparity in the space-filling characteristics of components A and B. The molecular asymmetry parameter is given as

$$\varepsilon = \left(\frac{n_A}{n_B}\right) \cdot \left(\frac{l_A}{l_B}\right)^{1/2} = \left(\frac{n_A}{n_B}\right) \cdot \left(\frac{\dfrac{V_A}{R_A^{2}}}{\dfrac{V_B}{R_B^{2}}}\right)^{1/2} = \left(\frac{n_A}{n_B}\right) \cdot \left(\frac{\dfrac{v_A}{b_A^{2}}}{\dfrac{v_B}{b_B^{2}}}\right)^{1/2} \tag{4}$$

where n_i is the number of arms of component i, and l_i is a material parameter describing the conformational behavior of component i. This material parameter is defined as $l_i = V_i/(R_i^2)$, where V_i is the volume of component i having radius of gyration, R_i. Both terms are proportional to chain length, N, and the equation defining ε reduces to a function of arm number, n_i, segmental volume, v_i, and statistical segment length, b_i.

The model predicts that the volume fraction range in which a given morphology is predicted to be observed shift to higher volume fraction with increasing molecular asymmetry. This arises from the effect of confining multiple arms to one side of an interface. To illustrate, consider a conformationally symmetric linear diblock of equal volume fractions A and B ($\phi_B = 0.5$), such as illustrated in Figure 1.7a. If the single arm of A is then replaced by two arms of A exactly ½ the length of the original arm of A, to maintain a flat interface (lamellar morphology), the two arms must be stretched more

than the single arm of A in the AB diblock (Figure 1.7b). This results in an increase in free energy, which may be partially alleviated by curvature of the interface away from the two A arms (Figure 1.7c). Volume fraction remains unchanged, but morphology has been dramatically altered by architecture. This effect produces the shift to higher volume fractions, with increasing molecular asymmetry, ε, of the volume fraction ranges in which block copolymer morphologies are predicted. As illustrated in Figure 1.6, for a series of A_nB stars, as n increases the change in predicted morphological behavior is significant.
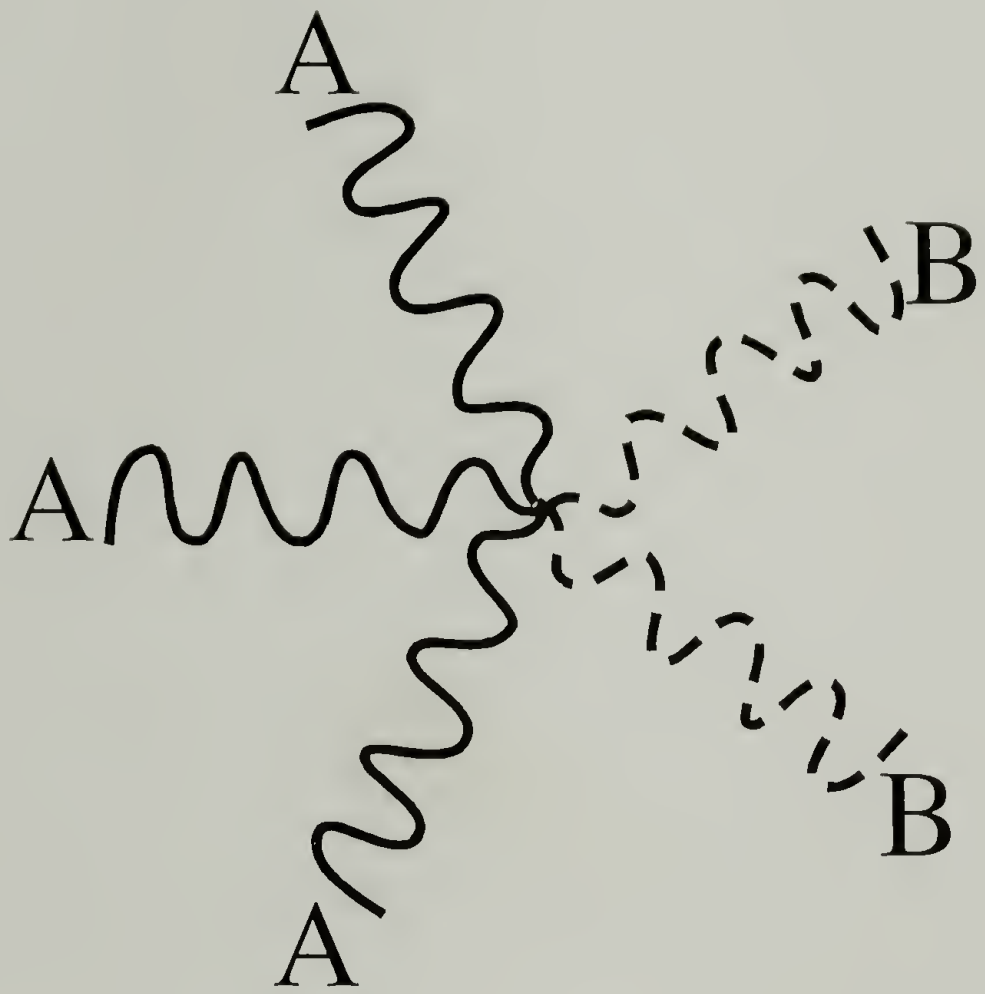
Figure 1.1. Schematic of an A_3B_2 miktoarm star comprised of three arms of polymer A and two arms of polymer B.
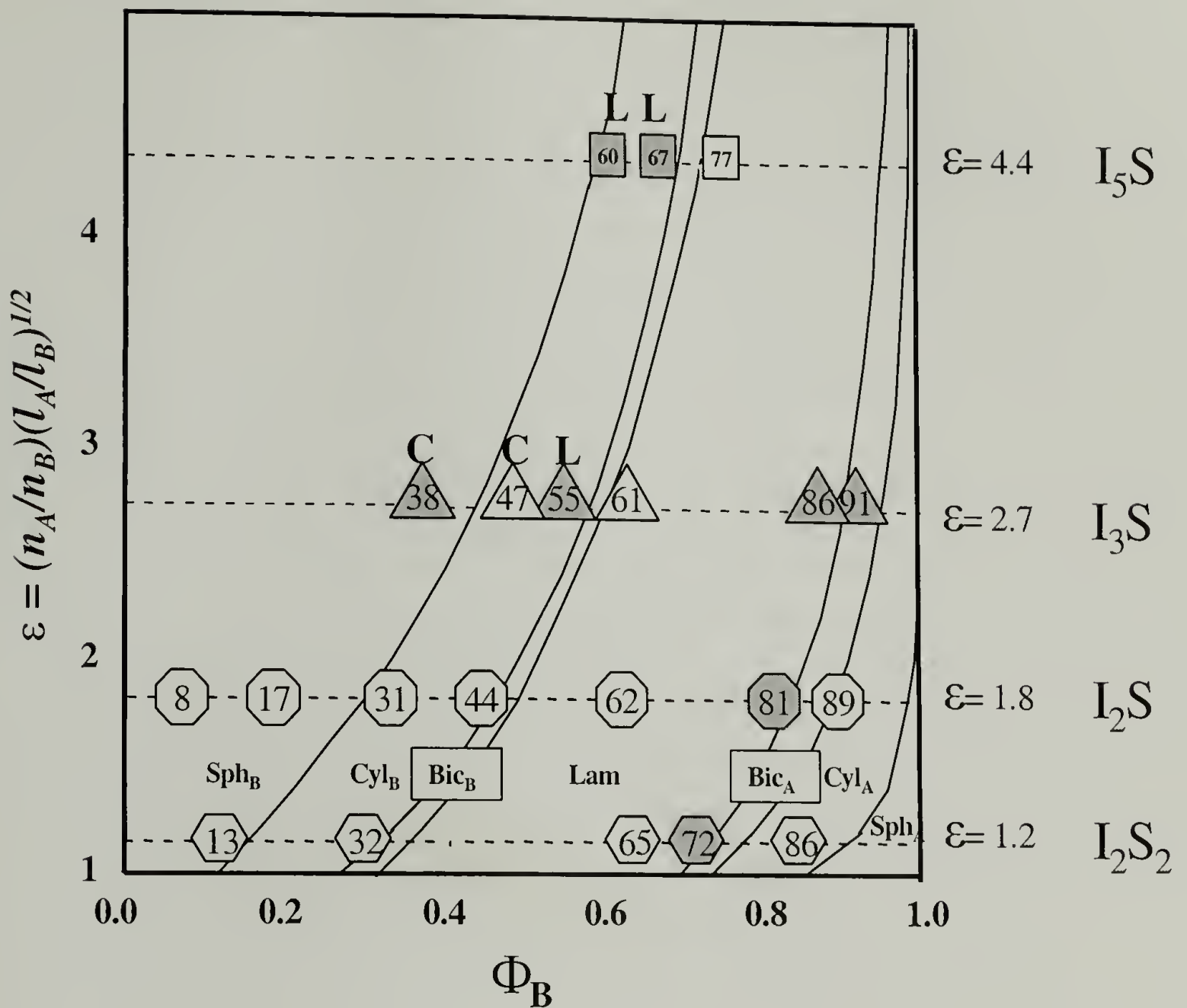
Figure 1.2. Strong segregation regime morphology diagram generated using the Milner model. Miktoarm star morphology is given as a function of volume fraction, ϕ_B, and molecular asymmetry. Shaded symbols indicate a sample whose morphology disagrees with that predicted by theory. The numbers in the symbols are the volume fraction of these samples. (For I_2S, I_3S, I_5S, these numbers are PS volume percentage, for I_2S_2 samples, the numbers are PI volume percentage).
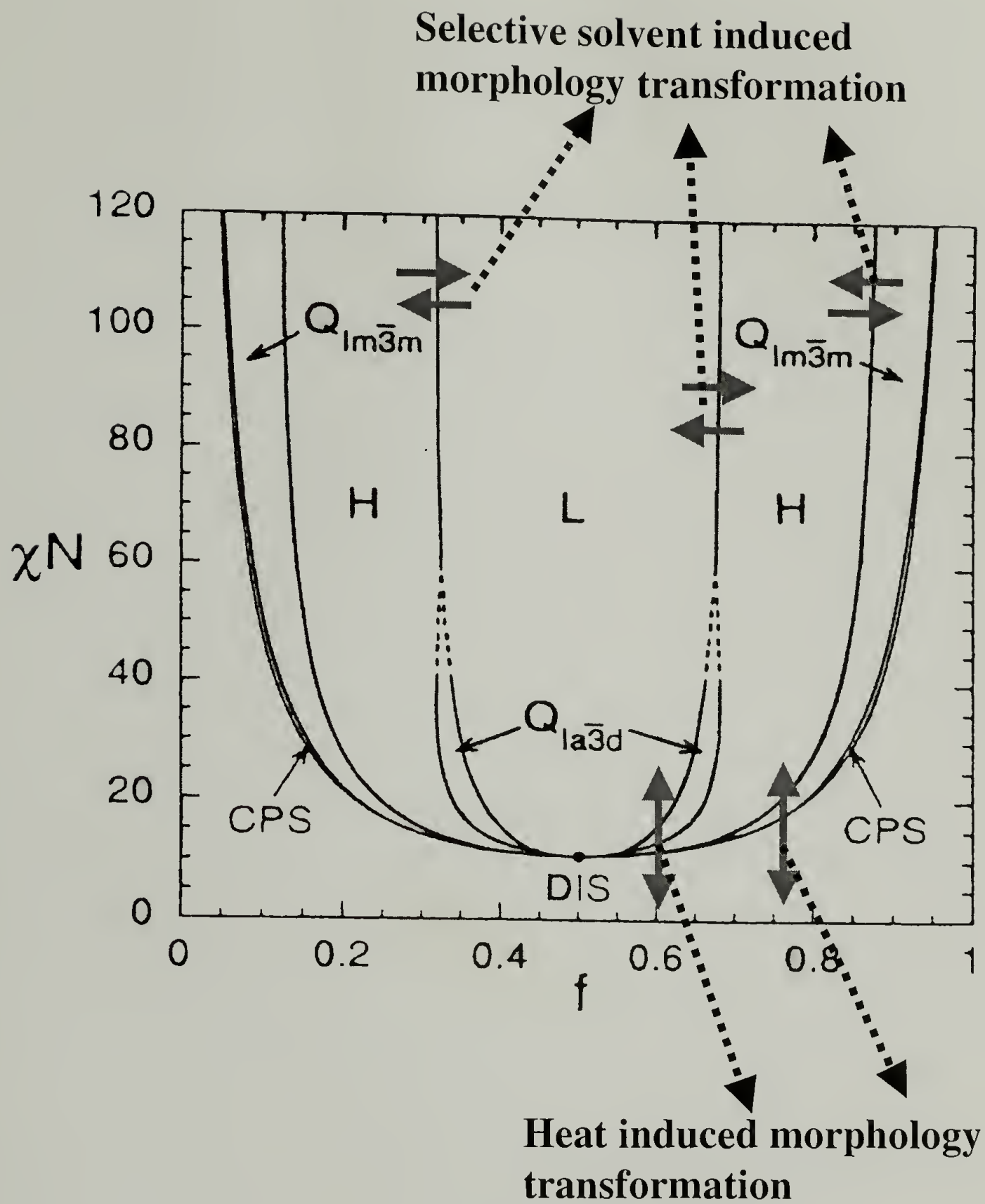
Figure 1.3. Schematics of morphology transformations. The vertical arrows indicate the schematics of reversible heat induced morphology transformation; well the horizontal arrows indicate the schematics of selective solvent induced irreversible morphology transformation.
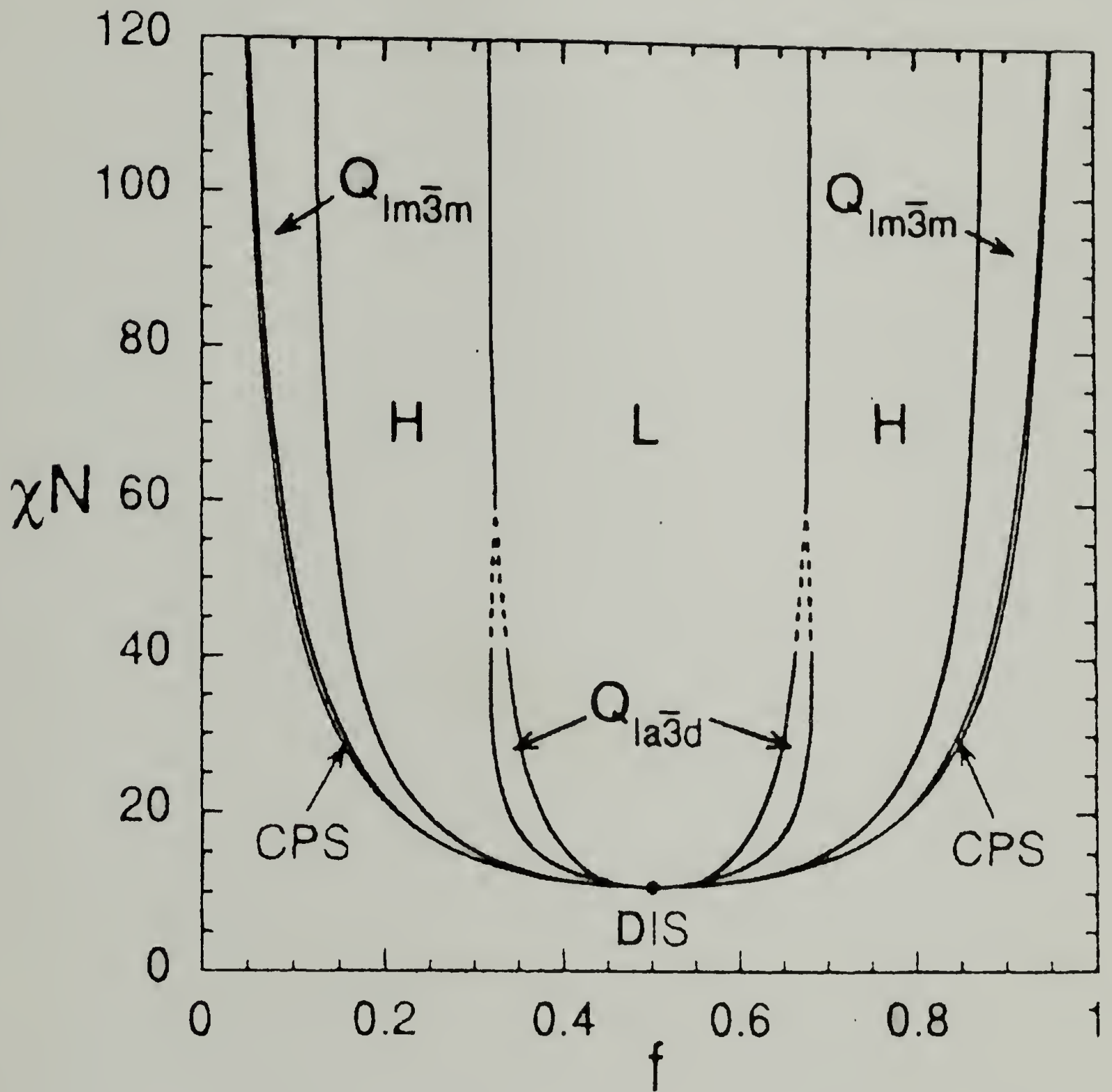
Figure 1.4. Morphology diagram for a linear AB diblock copolymer calculated by Matsen and Bates, spanning from the order-disorder transition into the strong segregation regime.

Sphere   Cylinder   Bicontinuous   Lamella
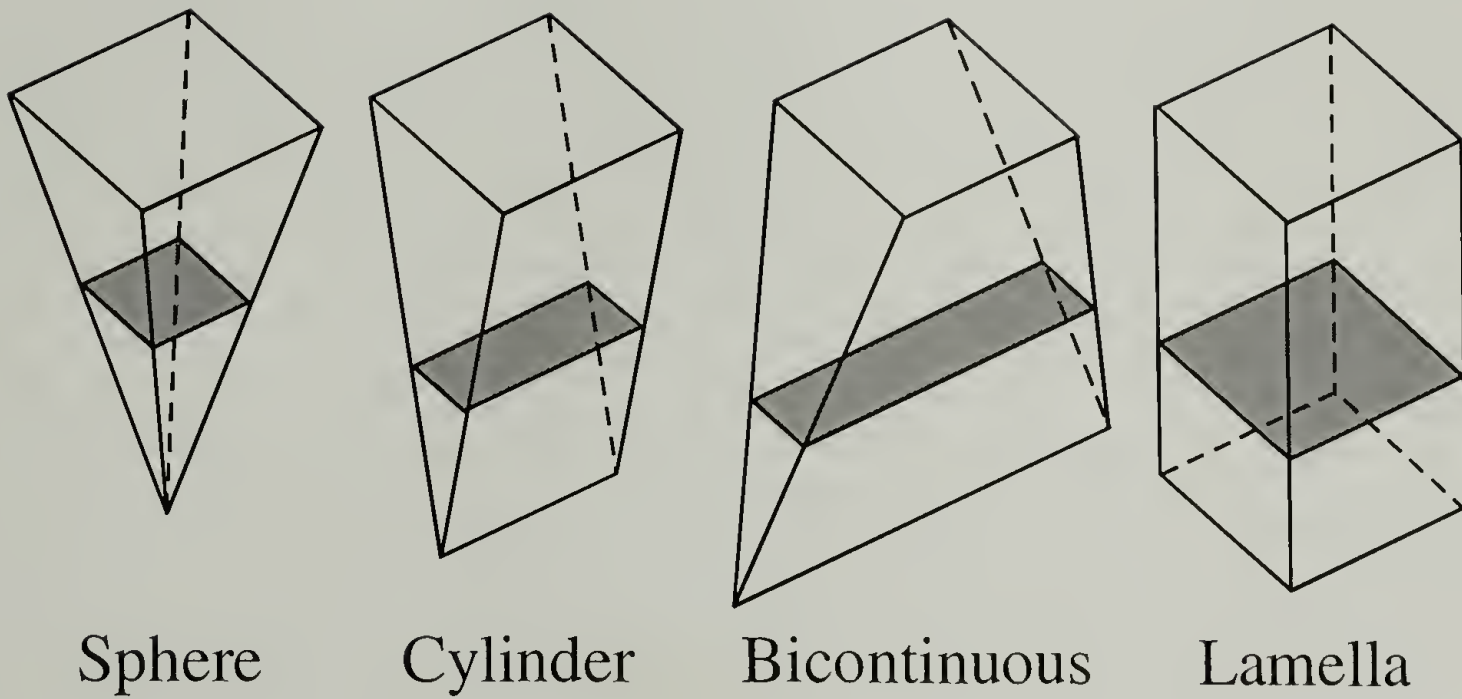
Figure 1.5.   Gaussian wedges for lamellar, cylindrical, spherical, and OBDD bicontinuous morphologies used in the Milner model for calculating morphological behavior of miktoarm star block copolymers. The shaded planes represent the interface between microphase-separated domains of components A and B.
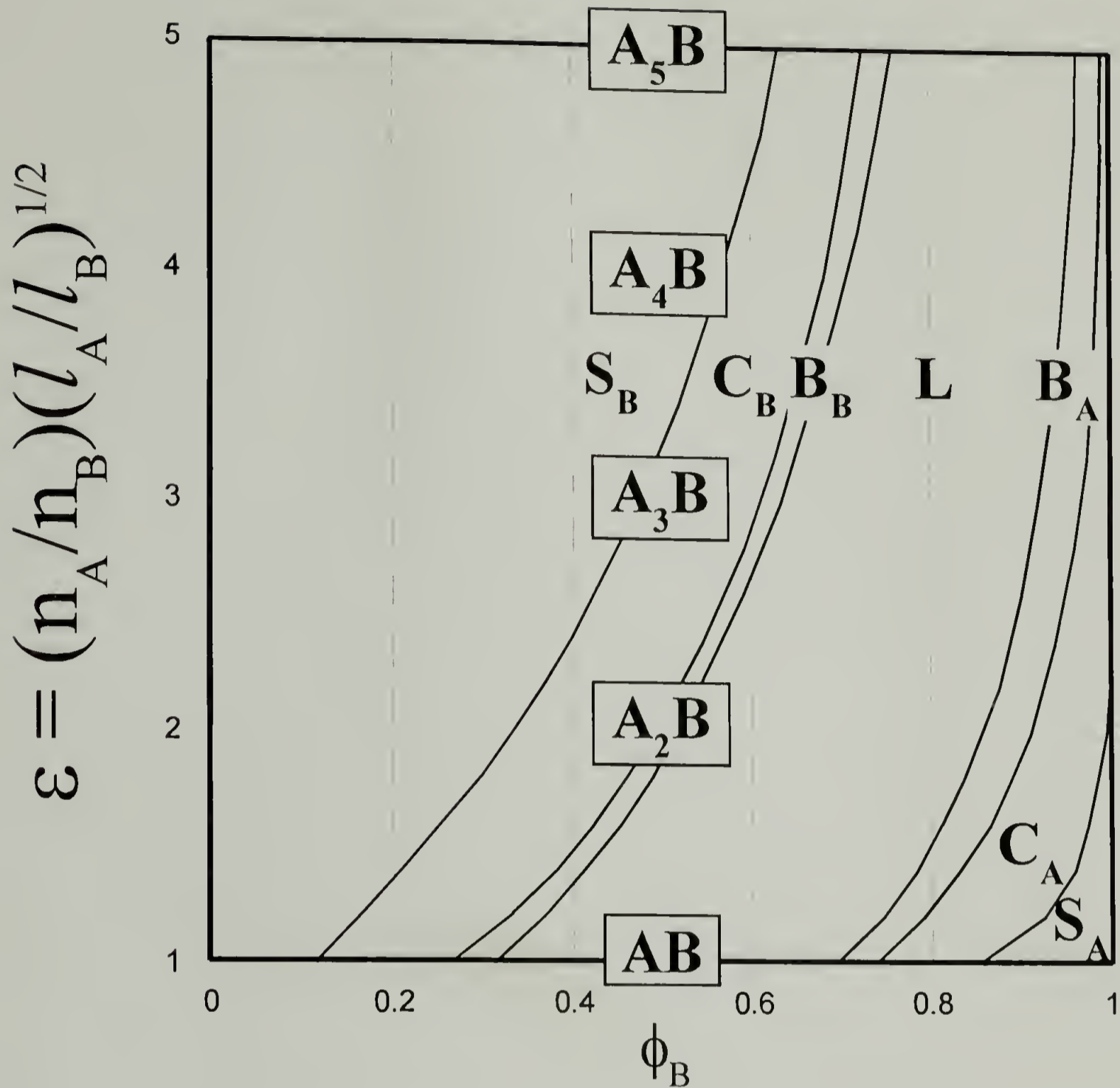
Figure 1.6.   Strong segregation regime morphology diagram generated using the Milner model. Miktoarm star morphology is given as a function of volume fraction, ϕ_B, and molecular asymmetry.   Boxes with A_nB stars indicate the level of molecular asymmetry for conformationally symmetric A_nB miktoarm stars, illustrating the effect of architectural asymmetry on morphological behavior.

CHAPTER 2

MORPHOLOGICAL BEHAVIOR OF I$_2$S SINGLE GRAFT

BLOCK COPOLYMER / HOMOPOLYMER BLENDS

2.1 Abstract

This work is part of an extensive study of model nonlinear block copolymer / homopolymer blends. Effects of graft molecular architecture on the morphology of block copolymer / homopolymer blends have been examined. The single graft Y shaped block copolymers used in the study are I$_2$S block copolymers, which have two low polydispersity (PDI) polyisoprene arms and one low PDI polystyrene arm joint at a single junction point. Previously reported linear diblock copolymer / homopolymer blend systems showed that the order-order transitions (OOTs) occur at about the same volume fractions as in pure linear diblock copolymers. The OOT occurs at the same volume fraction regardless of the direction from which it is approached, i.e. blending homopolymer A with a diblock which forms A cylinders in a B matrix to push it toward lamella or blending B homopolymer with a lamellar diblock to push it back toward cylinders.[17,18,20] This study shows that when blending a homopolymer with an I$_2$S block copolymer that the OOTs split so that they occur at different volume fractions depending up whether they are approached by blending homopolymer into the two arm or the one arm side of the block copolymer interface. A perforated lamellar morphology is obtained in a blend of homopolystyrene (hPS) and a lamella forming single graft block copolymer,

19

and it is found to be stable to thermal annealing. TEM features of perforated lamella are analyzed.

2.2 Introduction

Recently, there have been many investigations concerning the effects of graft block copolymer molecular architecture on morphology using well defined, *model* branched block copolymer materials.[2-5,8,10,87-89] The present study investigates the effect for molecular asymmetry and graft architecture on blend morphology. The morphologies of neat microphase-separated A_2B single graft copolymers have been studied by Pochan, Gido *et. al.*[2,87] The results of the experimental study were plotted on a theoretical morphology diagram for asymmetric *mikto*arm stars, calculated by Milner.[11] For architecturally and conformationally asymmetric miktoarm stars of type A_nB_m, this theory predicts morphology as a function of B component volume fraction, ϕ_B, and a molecular asymmetry parameter, $\varepsilon = (n_A/n_B)(l_A/l_B)^{1/2}$. Here, n_A and n_B are the numbers of arms of block materials A and B, and $l_i = (V_i/R_i^2) = v_i/b_i^2$. V_i and R_i are volume and radius of gyration of one arm of polymer *i*, while v_i is the segmental volume and b_i the statistical segment length of component *i*. The morphologies observed for the A_2B materials showed general agreement with the shift in composition ranges predicted by the theory. However, for some samples, the Milner calculation slightly overestimated the degree of shift in the order-order transitions.[87] Some other studies on S_2I, I_2S and I_3S also showed qualitative agreement but quantitative disagreement.[7-10,89,90] The Milner diagram is calculated for pure block copolymer. In this study, we will try to use it as a guide to

understand the effects of homopolymer blending on the morphological transitions of I_2S block copolymer systems.

Linear diblock copolymer / homopolymer blends and linear multi block copolymer / homopolymer blends systems have been extensively studied.[13-25] Previously reported linear diblock copolymer / homopolymer blend results showed that the OOTs in the blends occur at about the same volume fractions as those of pure linear diblock copolymers.[17,18,20] However, for architecturally asymmetric graft copolymers, blending homopolymer into the one arm side or into the multi-arm side of the interface may produce different morphological results. In the present study, I_2S block copolymers are blended with homopolymers of polystyrene (hPS) or homopolymer polyisoprene (hPI). The schematic of an I_2S single graft block architecture with one PS arms and two PI arms is shown in Figure 2.1.

One of the blends in this study is observed to form a hexagonally perforated lamellar structure. Hexagonally perforated lamellae, which resemble the cantenoid-lamellar structure derived by periodic area-minimizing surfaces calculations,[48] were also observed recently in linear diblock systems[35,37-39,46,50-52] in a narrow volume fraction region between HEX and LAM. Several linear block copolymer / homopolymer blends have been previously shown to form perforated lamellar structures.[22,53] To date, however, ordered perforated lamellar structures have not been observed in block copolymers or blends involving block copolymers with graft architectures.

Controversy exists regarding the details of the perforated lamella structure and the stability of the morphology. Both ABC stacking of the hexagonally perforated layers[38,52] and a combination of an ABC and AB stacking[39] were suggested for the perforated lamellar morphology. Using the methods of Semenov[55] to estimate the free energy of perforated lamella in the strong segregation limit (SSL), Fredrickson[56] showed that the perforated lamella is metastable with respect of cylinders and lamella at $\phi=0.35$. Qi and Wang[57-59] showed that the perforated lamellae appear as a "pseudostable" morphology during the lamellar to cylinder transition.

2.3   Experimental

The synthesis of the I_2S block copolymers and the subsequent molecular characterization was described in a previous publication.[87] The materials were produced by anionic polymerization under high vacuum in all glass reactors. The graft architecture was generated using coupling with trichloromethylsilane. The volume fraction and morphology of the neat I_2S block copolymers and homopolymers used in this study are listed in Table 2.1. The polystyrene of both the I_2S block copolymers and the homopolymer were deuterated. We use low molecular weight (MW) homopolymer in all the blend systems so that the distribution of the homopolymer within the block copolymer domains of like material is relatively uniform.[14,19,91] This study utilizes blends which have overall high PS composition. Blends with I_2S block copolymers having high overall PI composition have been examined separately.[92]

Graft copolymer and homopolymer in the proportions to give the desired blend were co-dissolved in toluene, a non-preferential solvent. Solid films approximately 1 mm thick were slowly cast from these co-solutions at room temperature over the course of 10 to 14 days. Residual toluene was removed by placing the samples under vacuum at ambient temperature for another week. Each sample was thermally annealed in a vacuum oven at 120 °C for two weeks to further promote the approach to equilibrium. The samples were then cooled under vacuum to room temperature over a period of several hours.

Sample morphologies were characterized using a combination of transmission electron microscopy (TEM) and small-angle X-ray scattering (SAXS). To prepare thin sections for microscopy, a Leica Ultracut UCT microtome equipped with a Leica EM FCS cryogenic sample chamber operated at -110°C was used to cut sections approximately 500 Å in thickness. The sections were collected on TEM grids and stained for four hours in OsO_4 vapor. The PI microdomains are preferentially stained by OsO_4, rendering them dark relative to PS microdomains due to mass-thickness contrast in the TEM. A JEOL 100CX TEM, operated at an accelerating voltage of 100 kV, was used to image the stained sections. SAXS data were collected at the Advanced Polymers Beamline (X27C), located at the National Synchrotron Light Source at Brookhaven National Labs (BNL), Upton, NY. Two-dimensional scattering patterns were collected on Fujitsu image plates, and then read by a Fujitsu BAS 2000 image plate reader. Custom software at BNL was used to subtract background noise and perform circular averaging. Data were collected for a wavelength of 1.307 Å and a camera length of 1410 mm.

23

Four different series of blends are examined. Blends are designated as either IYn-m or SYn-m. The first character, I or S, indicates that the homopolymer used in the blend series is either homopolyisoprene (I) or homopolystyrene (S). The first number n indicates the PS volume fraction of the Y shaped graft copolymer (I_2S-89, I_2S-81, or I_2S-62 from reference 4) on which the blend series is based. The last number, m, indicates the PS volume fraction of the overall blend after addition of homopolymer. The molecular characteristics of the block copolymers and homopolymers are listed in Table 2.1. The compositions of all the blends studied in this paper are given in Table 2.2.

2.4. Results

SY62 series

The pure single graft block copolymer I_2S-62 with polystyrene volume fraction $\phi_{PS} = 62\%$ formed a lamella morphology with a long period of 39.0 ± 0.5 nm.[87] The SAXS data for the SY62 blend series is shown in Figure 2.2. The first three blends, SY62-73, SY62-76 and SY62-79, maintain the lamellar morphology with slightly increasing lamellar spacing (Table 2.2). The fourth blend, SY62-82, forms perforated lamella. The layer spacing of perforated layers is 37.5 nm, which is a decrease from the lamellar spacing of SY62-79 due to the morphology change. The $\sqrt{3}\,q^*$ reflection results from the ordering of the perforations.[39,52] This scattering data does not permit the determination of detailed structural information about the stacking of the perforated layers. The perforated lamellar morphology persisted upon annealing at 120°C for 2

24

weeks. The fact that a perforated lamellar structure is found at this unusual composition is a direct result of the I_2S molecular architecture of the block copolymer used in the blend. TEM micrograph of the blend series is shown in Figure 2.3.

As the PS volume fraction further increases, the blends SY62-85 and SY62-89 both form cylindrical morphologies, and the cylinder *(100)* d-spacing increases as the homopolymer volume fraction increases (Table 2.2). TEM observation (data not shown) confirmed the cylindrical morphologies of SY62-85 and SY62-89. The morphologies of the SY62 blends series are mapped onto the theoretical morphology diagram in Figure 2.4.

SY81 series

The pure single graft block copolymer I_2S-81 with polystyrene volume fraction $\phi_{PS} = 81\%$ formed a regular cylinder morphology with reported cylinder *100* spacing of 31.0 ± 0.5 nm.[87] The two blend samples of the SY81 series were made by blending low molecular weight homopolystyrene with I_2S-81. The morphologies of the SY81 blend series are mapped onto the morphology diagram in Figure 2.5. TEM images of SY81-82 and SY81-85 are shown in Figure 2.6. The long-range order of the morphology decreases as hPS concentration increases and essentially vanishes for SY81-85. The SAXS data shown in Figure 2.7 support this conclusion. The *(100)* spacings of SY81-82 and SY81-85, 31.6 nm and 30.6 nm respectively, are nearly the as same as that of pure I_2S-81. The secondary peak of SY81-85 is broad and weak. We calculated form factor scattering that results from disordered arrangements of domains of spheres and cylinders. Domain sizes are obtained by using the primary peak to get an average center-to-center

25

distance between neighboring domains. This spacing along with the known PS and PI volume fraction can be used to calculate sphere and cylinder radii provided that a model for how the domains fill space is assumed. For the purposes of these calculations cylinder radii were obtained assuming a hexagonal packing and sphere radii were determined using both BCC and SC lattice packings.[93,94] All the form factors for cylinders and spheres (both BCC and SC) fit the data poorly. This suggests that the broad peak is actually from weak and diffuse $\sqrt{3}\,q^*$ and $2q^*$ Bragg reflections, and the sample has a poorly ordered cylindrical morphology. Both TEM and SAXS indicate that the long-range order of the cylinder morphology decreases as more PS homopolymer is added.

IY81 series

The morphologies of the IY81 blend series are also mapped onto the morphology diagram in Figure 2.5. In this series, in which hPI is blended into I_2S-81, samples IY81-80, IY81-76, IY81-73, IY81-71 and IY81-66 all form cylindrical morphologies. Figure 2.8a shows a TEM image of one of these cylindrical morphologies (IY81-66), the others are similar. There is little change in long-range order with increasing hPI concentration among these cylindrical samples but all are quite well ordered as compared to the SY81 series. With only one volume percent more PI, blend IY81-65 changed to the lamellar morphology. No intermediate morphology, such as gyroid or perforated lamella, was observed between lamellae and cylinders in this series. Figure 2.9 shows the SAXS data for this series. The cylinder *(100)* spacings, shown in Table 2.2, increased with increasing amounts of homopolyisoprene in the blends.

IY89 series

The pure single graft block copolymer I_2S-89, with ϕ_{PS}=0.89, formed a morphology of disordered, worm-like cylinder domains of PI in a matrix of PS.[2,87] TEM images of the IY89 series, which are produced by blending increasing amounts of hPI with I_2S-89, are shown in Figure 2.10. Figure 2.10b reveals that IY89-86 formed a disordered worm-like cylinder morphology, similar to pure I_2S-89 (Figure 2.10a). Figure 2.10b is a TEM image of blend IY89-82 showing that the dark stained PI domains form ring-like structures and short line segments. Blends IY89-80, IY89-77, and IY89-71 with increasing PI volume fractions also formed sheet-like morphologies but in these cases closed vesicles were not favored (although a few isolated vesicles can be observed in the TEM images). The predominant structures were continuous, convoluted sheets which extend over great distances relative to their sheet thickness. A TEM image of this structure in IY89-80 and IY89-71 are shown in Figure 2.10d and Figure 2.10e. Due to the lack of lattice order in the IY89 blend series, SAXS data was not used for structural investigation. Figure 2.11 shows a higher magnification TEM tilt series of blend IY89-82 that reveals that some PI domains which appear as short line segments, are actually pieces of sheets. Some PI domains which appear as rings are actually sections through vesicles, and other objects seem to be caps sectioned off the top or bottom of vesicles. The schematic of the vesicle and their TEM projection are illustrated in Figure 2.12. The rings and caps have different projections with the change of viewing angles and microtome positions. The thickness of these PI sheets is about 12 nm. The diameters of the vesicles as well as the lengths of the PI sheets are about 150~500nm. The morphology of IY89-82 is composed of bilayer sheets which tend to form closed vesicles or isolated sheets which seem to be limited in there lateral extent to an upper limit of

about 40 times the PI layer thickness. The vesicle and sheet structures of the IY89 series are unusual because the spaces inside the vesicles and between vesicles and/or sheets are frequently much larger (up to almost 1 μm in size) than the radii of gyration of the PS blocks of the I_2S-89 block copolymer (PS molecular weight of 87,300 g/mol). The TEM images suggest that the vesicles and sheets grow by formation of organized block copolymer bilayers in a matrix of un-microphase separated material.

2.5   Discussion

For the lamella samples in the SY62 series, the polystyrene brush height and the polyisoprene brush height can be calculated by $h_{PS}=(\frac{1}{2})d_{lam}*\phi_{PS}$ and $h_{PI}=(\frac{1}{2})d_{lam}*\phi_{PS}$ respectively, where d_{lam} is the long period of the lamella structure. The area per block copolymer chain junction can be calculated by $A=M_{PI}/(d_{lam}*\phi_{PI}*\rho_{PI}*N_{av})$, where M_{PI} is the average total molecular weight of the two PI arms of each block copolymer molecule, ρ_{PI} is the density of polyisoprene and N_{av} is Avagadro's number. After blending in homopolymer, the PS domains swell both parallel and perpendicular to the interface. We can calculate the relative vertical expansion of the PS domain in the blends with respect to the PS brush height of the pure block copolymer (I_2S-62): $\lambda^{\perp}=h/h_o$ where h_o is the PS brush height of the pure block copolymer I_2S-62, and h is the PS brush height of the blend sample. From the area per junction of each blend, the relative expansion ratio in the direction parallel to the interface is calculated by $\lambda^{//}=(A/A_o)^{0.5}$. Therefore, the total swelling of the PS domains can by expressed by the two expansion ratios: $V/V_o=\lambda^{\perp}(\lambda^{//})^2$. If the domain expansion is uniform in all directions, $V/V_o=\lambda^3$, with $\lambda=\lambda^{\perp}=\lambda^{//}$; if the

28

expansion is anisotripic then $\lambda^{\perp}$ and λ'' will not be equal and we define their ratio as the expansion asymmetry coefficient: $K=\lambda^{\perp}/\lambda''$. All the calculated results are listed in Table 2.3 and the asymmetry coefficient for lamella forming SY62 series blends verses homopolymer volume fraction is plotted in Figure 2.13, from which it is apparent that $K\approx1$ and changes little with increasing hPS concentration.

The cylinder core radii R of the samples in the IY81 and SY81 blend series were calculated from the (100) interplanar spacing determined by SAXS and the volume fraction of PI ($R_{cyl} = d_{hex(100)} (\frac{\phi_{PI}}{\pi} Sin\frac{\pi}{3})^{\frac{1}{2}}$). The area per block copolymer chain junction can be calculated by $A=(2M_{PI}/(\rho_{PI}R_{cyl}N_{av})$. For the IY81 series, M_{PI} is the effective total polyisoprene molecular weight per junction point, which includes the PI content of a single block copolymer molecule as well as the total amount of hPI per block copolymer molecule. This is calculated by dividing the total number of hPI molecules in the system by the total number of block copolymer molecules. We use the cylinder core radius R_{cyl} as the average PI brush height; the polystyrene brush height can be calculated by $h_{PS} = (\sqrt{3} d^2_{hex(100)}/\pi)^{\frac{1}{2}} - R_{cyl}$. From these values, λ'', $\lambda^{\perp}$ and K are calculated for the IY81 and the SY81 series and are listed in Table 2.3. The asymmetric swelling coefficient K is plotted verses homopolymer volume fraction in Figure 2.13 for cylinder forming blends in both the SY81 and the IY81 series.

Figure 2.13 shows that expansion coefficients K of the SY62 series and the SY81 series are close to one and change little with increasing ϕ_{PS}. Thus $\lambda^{\perp}\approx\lambda''$, i.e. in both

series, the homopolystyrene swells the PS domains homogeneously. Because the PS and PI domains share the same interface, the component of PS domain swelling parallel to the interface in the SY81 series leads, through conservation of volume, to a decrease of the brush height in the PI domains. Consequently, the overall structural periodicity, the sum of the PS and PI domain thickness, changes very little (Table 2.2). This behavior is considerably different from the IY81 series in which swelling perpendicular to the interface is favored. This can be seen in Figure 2.13 where K increases with increasing hPI content. As hPI is added, the PI layer thickness increases much more strongly than the interfacial area per junction. In this case the overall structural periodicity was found to increase rather strongly with the addition of hPI as indicated in Table 2.2.

Previously published studies on the swelling behavior of block copolymer / homopolymer blends, indicate that the degree to which homopolymer penetrates into the brush of the corresponding block of the copolymer depends on the ratio, α, of the homopolymer molecular weight to the molecular weight of the block of the same type.[14,19,91,95] In both the SY62 and SY81 series $\alpha=0.01$, and in the IY81 series $\alpha=0.09$. Therefore, a comparison of swelling behavior on the two arm PI side of the interface to that on the one arm PS side of the interface is potentially complicated by a difference in α. However, comparison to data of Winey, Thomas and Fetters[19] on blends of linear diblocks with homopolymer, also plotted in Figure 2.13, suggest that the molecular architecture effect on I_2S containing blends is significant enough to be distinguishable even with the α difference.

30

The linear diblock swelling data in Figure 2.13 indicates that with α=0.1, 2600 g/mol hPS swells the PS domain of PS-b-PI (PS 27,000 g/mol, PI 22,000 g/mol) relatively homogeneously. The SY62 and SY81 series, with α=0.01, both show similarly isotropic swelling behavior. This observation is consistent with theoretical calculations of Matsen[95] and Shull and Winey[91], which indicate that at α below 0.125 to 0.10 that homopolymer homogeneously swells the like block of a linear diblock. This suggests that in the IY81 blend series with α=0.09 that the effect of miktoarm star architecture plays a key role in the asymmetric swelling behavior. At the very least, the fact that there are two PI blocks per molecule in the PI block copolymer brush, reduces the value of α for which swelling becomes homogenous to something smaller than the value of 0.1 found for linear diblock containing blends. The IY81 series and the Winey 2600 g/mol hPS / linear diblock blend series have similar α values of 0.09 and 0.1 respectively. However, the IY81 series in which the homopolymer is blended into the two arm side of the block copolymer interface shows dramatic swelling anisotropy, while the linear diblock containing blend series shows isotropic behavior.

The miktoarm star molecular architecture of the block copolymer contributes to the differences in homopolymer swelling behavior on the two sides of the interface between the SY81 and SY62 series, and the IY81 series. The higher crowding of the grafted block copolymer brush on the PI side of the interface, due to the fact that there are two PI blocks per I_2S molecule,[10,96] may make it more difficult for the hPI to penetrate into the PI brush than for the hPS to penetrate the PS brush on the other side of the interface. In the IY81 series, this results in more hPI adding to the center of the PI

domains rather than penetrating to the interface, thus increasing the domain thickness faster than the interfacial area as more homopolymer is added. On the other side of the interface, with one PS arm per block copolymer molecule, the hPS in the SY81 and SY62 series penetrates more easily into the brush resulting in more isotropic swelling behavior.

In diblock copolymer / low molecular weight homopolymer blends, the OOTs generally occur at the about the same overall volume fractions as those of pure diblock copolymer.[17,18,20] Additionally, an OOT occurs at the same volume fraction regardless of the direction from which it is approached, i.e. blending homopolymer A with a diblock that forms A cylinders in a B matrix to push it toward lamella, or blending B homopolymer with a lamellar diblock to push it back toward A cylinders.[17,18,20] In the present study, blending homopolymer into each sides of the interface in systems based on the asymmetric I_2S molecular architecture results in a splitting of the OOT location such that it occurs at different volume fractions depending on the direction from which it is approached. In the IY81 series, blending hPI with cylinder forming I_2S-81 results in a transition to lamella at $\phi_{PS} = 0.65$ to 0.66. This is a substantial shift from the cylinder to lamellar transition predicted by the Milner morphology diagram (around $\phi_{PS} \approx 0.80$), and is close to the PS volume fraction at the lamellar-cylinder OOT in linear diblocks. Figure 2.4 indicates that the OOTs of the SY62 series, in which a lamellar system is pushed toward cylinders by blending with hPS, occur at a ϕ_{PS} value closer to that predicted by the Milner theory for architecturally asymmetric I_2S molecules. The transition from lamella to perforated lamella occurs at a PS volume fraction between 0.79 and 0.82, and the transition from perforated lamella to cylinders occurs at a PS volume fraction between

0.82 and 0.85. In the IY81 blends series, neither perforated lamella nor Gyroid morphology was observed. The splitting of the OOTs in the SY62 and IY81 series most likely results from the asymmetry in the ability of the homopolymer to penetrate the PI and PS brushes due to the difference in chain crowding on the two sides of the interface in the I_2S material. The homopolymer must be able to effectively penetrate this brush in order to drive the changes in interfacial curvature, which accompany an OOT.[17,18,20]

The SAXS data for the perforated lamellar sample (SY62-82) indicates that the layer repeat distance of the perforated lamella and the distance between adjacent perforations are both about 40 nm. Measured from the TEM image, the PI layers are about 10 nm thick and the PS layers are about 30 nm thick. The distance between adjacent PS perforations is also about 40 nm. From the SAXS and TEM data, we cannot distinguish between ABC and AB stacking of the perforated layers. SAXS scattering pattern of perforated lamella has been studied by several groups.[35,37-39,46,50-52] Some analysis of these projections has been given previously by Bates and coworkers.[38]However, detailed analysis of the interesting TEM projections of perforated lamella has not been reported.

Figure 2.14 illustrates the model for hexagonally perforated lamella. The upper model was proposed by Bates group. It illustrates the alternating black and white layers with the majority component (the black component in the model) perforate though the minority component (the white component) hexagonally. In this model, the perforations were drawn as solid cylinder shape. In reality, the sharp 90° angles between the vertical cylinder perforations and the flat layers has high energy and cannot exist in nature. The

33

perforations actually adopt catanoid shape, as shown in the lower model. Different TEM projections are possible depending upon the direction of projection within the layer of perforations and on the way in which the thin section intersects the three-dimensional structure. In general these projections reveal the layering of the structure as well as a side view of the perforations. When microtome parallel to the XY plane and viewing along Z axis in electron microscope, as shown in Figure 2.15, a projection of white spots in dark background is observed. The white spots are the PS perforations, and the dark background is the stained PI layer. The projection appears like a hexagonal honeycomb mesh of dark PI perforated by holes of light PS. This image is striking for its illustration of the relatively thin mesh-like structure in the PI layer that results from the low PI volume fraction of 0.18 in this blend. Since the perforations are not straight cylinder shape, the contrast between the white perforation and the dark PI layer is not sharp. The projection also cannot reflect the alternating PI PS layer structure, as the observation direction is perpendicular to XY plane.

Figure 2.16 illustrates the TEM images obtained when the microtoming cuts perpendicular to the layered structure and thus the TEM projection occurs parallel to the layers. The electron beam is perpendicular to the film surface and will go though the film. Since the observation direction is parallels the XY plane, the TEM projections reflect the alternating PS PI layers, which is what we observed. The PS perforations in the PI plane become white spot in the projections. However, the appearance of these perforations can appear differently depending on the microtome direction within the XY plane. Shown in Figure 2.16, case a, the microtomed film contains one row of PS perforations or two row of PS perforation stacking exactly over each other. They have

34

the same electron transmission intensity profile, as shown in Figure 2.16, where the maximums are at the center of the PS perforations, which correspond to the white area in the schematic and TEM micrograph of Figure 2.16 a1, and the distance between the adjacent maximums is the distance between PS perforations. These features are supported by the TEM micrograph a. Measured from TEM, the average distance between adjacent white spots is 40nm; the distance measured from SAXS is 37nm. Considering the accuracy of TEM measurement, this two distance agrees with each other very well. Figure 2.16, Case b show another extreme case where PS perforations of one row are positioned exactly in the middle of two PS perforations of the other row. The electron transmission intensity profile of case b shows intensity minimums at the center of the PS perforations. The height of the intensity maximums is low. And the distance between the adjacent maximums is half of the distance of the adjacent PS perforations. Reflected in the TEM projection schematics in Figure 2.16 b, the contrast of the black spots and the gray PI layer is low; the black spots are small and near each other. These features are supported in the TEM micrograph b.

Figure 2.17 discusses shows TEM projections when the cutting direction is tilted. Since the grain direction of perforated lamella is usually random and constantly change inside a bulk sample. Most TEM observation reflects the microtome directions neither perpendicular to XY plane nor parallel to XY plane. Shown in Figure 2.17, as the tilting angle θ decrease from 90° to 0° the TEM projections change from that of Figure 2.16 to that of Figure 2.15. The dark PI layers will appear thicker and thicker as the tilting angle θ decreases. When the tilting angle is appropriate, the TEM will show regular

35

projections. For example, when $\tan\theta=a/b$, the microtomed PI layer will contain one bright PS perforations within each dark PI layer. In the projected image, the position of the PS perforation inside the PI layer can change, as illustrated in Figure 2.17, schematic B. the PS perforation appears to be two half with spots in the both sides of a dark PI layer. Further decrease the tilting angle θ, the black PI layer band will appears thicker and the white PS layer band in the projection will appears thinner in the projected image. And the differences in thickness will increase with the decreasing of tilting angle θ. The projection in TEM will feature more multi-perforation in PI layers. When $d/\cos\theta = 2a/b$, the projection will contain 2 adjacent bright PS perforations in PI layer; when the tilting angle is even smaller ($2a/b<d/\cos\theta$), the PI layer will contain more than 2 PS perforations in the projection. In reality, due to the constant changing of the grain direction, the TEM image of Figure 2.17 shows a combination of those features. As marked on the TEM micrograph, position A, B, C, and D reflects the projection of schematic A, B, C, and D respectively. In 3 dimension, the microtome direction can actually tilt in YZ other direction as well and the combination of these two tilting will lead to more complex projections. As the result, the TEM images of perforated lamella contain the regular ones mention above and more irregular projection, all of them reflect the structure features of alternating layers and the perforation of the majority component perforated though the minority hexagonally.

In previously reported vesicle forming block copolymer / homopolymer blend systems, employing a relatively high molecular weight homopolymer, the homopolymer is the major component and the block copolymer forms a bilayer in the homopolymer

36

matrix.[97] That structure is analogous to the classical vesicle structures in surfactant systems. Although the morphology of the IY89-82 blend (Figure 2.11) has a vesicle-like appearance, its structure is inverted from the standard vesicle structure. The block copolymer amphiphile forms the matrix, both inside and outside of the vesicles, while the minor component homopolymer resides in the double layer formed by the short PI blocks.

With the addition of increasing amounts of hPI in the IY89 series samples IY89-80 to IY89-71, the PI sheets forming the closed vesicles in IY89-82 become connected in a network of randomly ordered sheets that appear to form sample spanning structures, at least on the scale of our TEM observation. We speculate that the transition from a structure of predominantly closed vesicles and isolated sheets in IY89-82 to a structure dominated by continuous sheets at higher hPI content may be a percolation phenomenon. During microphase separation of the sheet-like PI structure there will be an energetic driving force to avoid free sheet edges. This can be accomplished by either forming closed vesicles or by producing a semi-infinite network of sheets. During the microphase separation process at lower overall PI content (IY89-82) embryonic pieces of microphase separating sheet structure do not find enough neighboring sheet material to form a network and thus tend to close on themselves to produce vesicles. At slightly higher overall PI content, the percolation threshold is apparently reached and the microphase separating sheets "find" enough like structure in the system to link up into a continuous network. Above the percolation threshold, there is no obvious morphology change from IY89-80 to IY89-71.

2.6   Conclusions

In blends of asymmetric I_2S block copolymer and homopolymers of either PS or PI, the order-order transitions were found to occur at different volume fractions depending on which type of homopolymer was used in the blends. Measurements of domain spacings showed that the PI homopolymer does not penetrate as well into the two-arm per molecule PI brush of the I_2S as does PS homopolymer into the one-arm per molecule PS brush on the PS side of the interface. This asymmetry of homopolymer brush penetration brought about by the asymmetric architecture of the graft copolymer leads to the splitting of the OOTs. Some of the blends produced interesting and unusual morphologies. For instance sample SY62-82 formed well ordered perforated lamella in which the perforated layers comprised only 18 volume percent of the structure. This perforated lamellar morphology was found to be stable to thermal annealing, which indicated that perforated lamella could be stable at certain composition. Unusual vesicle and continuous folded sheet morphologies were found in other blends. A transition been closed vesicles and continuous sheet structures was observed as a function of the overall concentration of the PI, which forms the vesicle or sheet walls. This may result from percolation effects. When the PI concentration is lower, there is not enough material to form a continuous network of sheets, and isolated vesicles form instead. At higher PI concentrations a percolation threshold is reached and the sheet structures can link up into a network.

Table 2.1.   Molecular characterization of the I_2S block copolymer and the PS and PI homopolymers.

a membrane osmometry; b SEC; c Vol% calculated utilizing density of (d-PS)=1.14 g/ml at 25oC and density of PI = 0.91 g/ml at 25oC [98] along with the weight percent compositions from SEC-UV.

Sample Name	[a] M_n(PS arm) (×10⁻³)	[a] M_n(PI arm) (×10⁻³)	[a] M_n (total)	[b] M_w/M_n	[c] Vol% d-PS	[d] $2\pi/q^*$ (± 0.5nm)
I_2S-89	87.3	4.6[e]	97.1×10³	1.04	89	
I_2S-81	79.1	9.6	89.4×10³	1.04	81	31.0
I_2S-62	61.2	14.8	83.0×10³	1.04	62	39.0
hPS			870	1.03		
hPI			872	1.17		

Table 2.2.   Composition and Morphology of the blends in the study.

[a] Calculated utilizing density of (d-PS)=1.14 g/ml at 25°C and density of PI = 0.91 g/ml at 25°C.[98] [b] $q* = 4\pi/\lambda(\sin \theta_1)$ and $2 \theta_1$ is the scattering angle for the lowest angle Bragg peak; corresponds to $d_{(100)}$ for hexagonal packed cylinders, $d_{(001)}$ for lamellae, respectively.

Sample Name	Weight Fraction of Homopolymer	Overall Weight Fraction of PS	[a] Overall Volume Fraction of PS	Morphology	[b] $2\pi/q*$ (± 0.5nm)
IY89-86	0.032	0.88	0.86	Worm	
IY89-82	0.068	0.85	0.82	Vesicle and Sheet	
IY89-80	0.081	0.83	0.80	Disordered layer and Vesicle	
IY89-77	0.12	0.80	0.77	Disordered layer and Vesicle	
IY89-71	0.17	0.75	0.71	Disordered layer and Vesicle	
IY81-80	0.013	0.83	0.80	Cylinder	33.3
IY81-76	0.045	0.80	0.76	Cylinder	33.3
IY81-73	0.083	0.77	0.73	Cylinder	34.5
IY81-71	0.12	0.75	0.71	Cylinder	35.2
IY81-66	0.16	0.71	0.66	Cylinder	37.5
IY81-65	0.17	0.70	0.65	Lamella	40.4
SY81-82	0.062	0.85	0.82	Cylinder	31.6
SY81-85	0.25	0.88	0.85	Disordered Cylinder	30.6
SY62-73	0.30	0.77	0.73	lamella	38.5
SY62-76	0.39	0.80	0.76	lamella	39.4
SY62-79	0.48	0.83	0.79	lamella	40.0
SY62-82	0.54	0.85	0.82	Perforated Lamella	37.5
SY62-85	0.64	0.88	0.85	Cylinder	35.2
SY62-89	0.72	0.91	0.89	Cylinder	36.2

40

Table 2.3.   Table of brush heights and swelling ratios of the blend samples.

	H_{PI} (Å)	H_{PS} (Å)	$\lambda^{\parallel}$	$\lambda^{\perp}_{\text{swollen phase}}$	$\lambda^{\perp}_{\text{unswollen phase}}$	K
I_2S-81	81.9	106.0	1.00	1.00	1.00	1.00
IY81-80	90.3	111.6	0.99	1.10	1.06	1.11
IY81-76	98.9	103.0	1.04	1.21	1.00	1.17
IY81-73	108.7	100.5	1.09	1.33	0.99	1.22
IY81-71	114.9	98.5	1.11	1.40	0.99	1.26
IY81-66	132.6	94.8	1.16	1.62	0.98	1.39
I_2S-81	81.9	106.0	1.00	1	1.00	1.00
SY81-82	81.3	153.4	1.00	1.03	0.99	1.03
SY81-85	71.9	155.4	1.07	1.05	0.88	0.98
I_2S-62	74.1	120.9	1.00	1.00	1.00	1.00
SY62-73	52.0	140.6	1.19	1.16	0.70	0.97
SY62-76	47.2	149.6	1.25	1.24	0.64	0.99
SY62-79	42.1	158.2	1.33	1.31	0.57	0.99

41
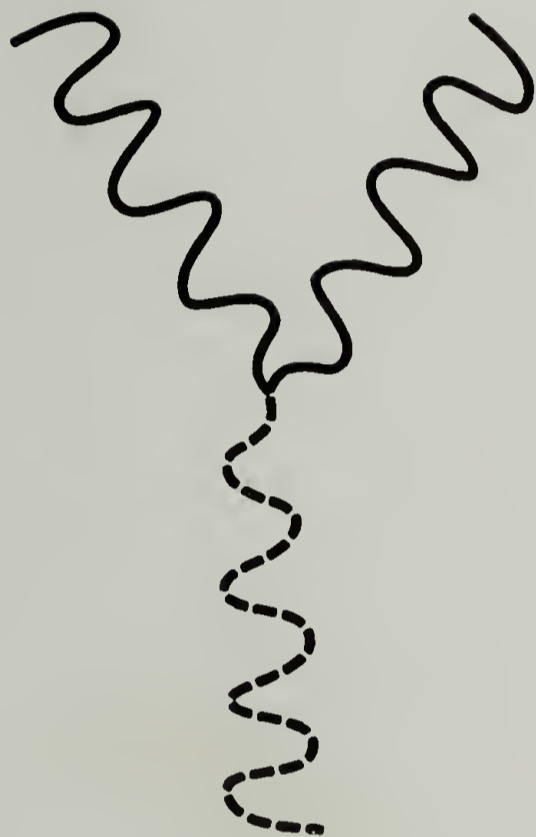
Figure 2.1.   Schematic of an I₂S single graft block architecture with one PS arms (dashed) and two PI arms (solid).
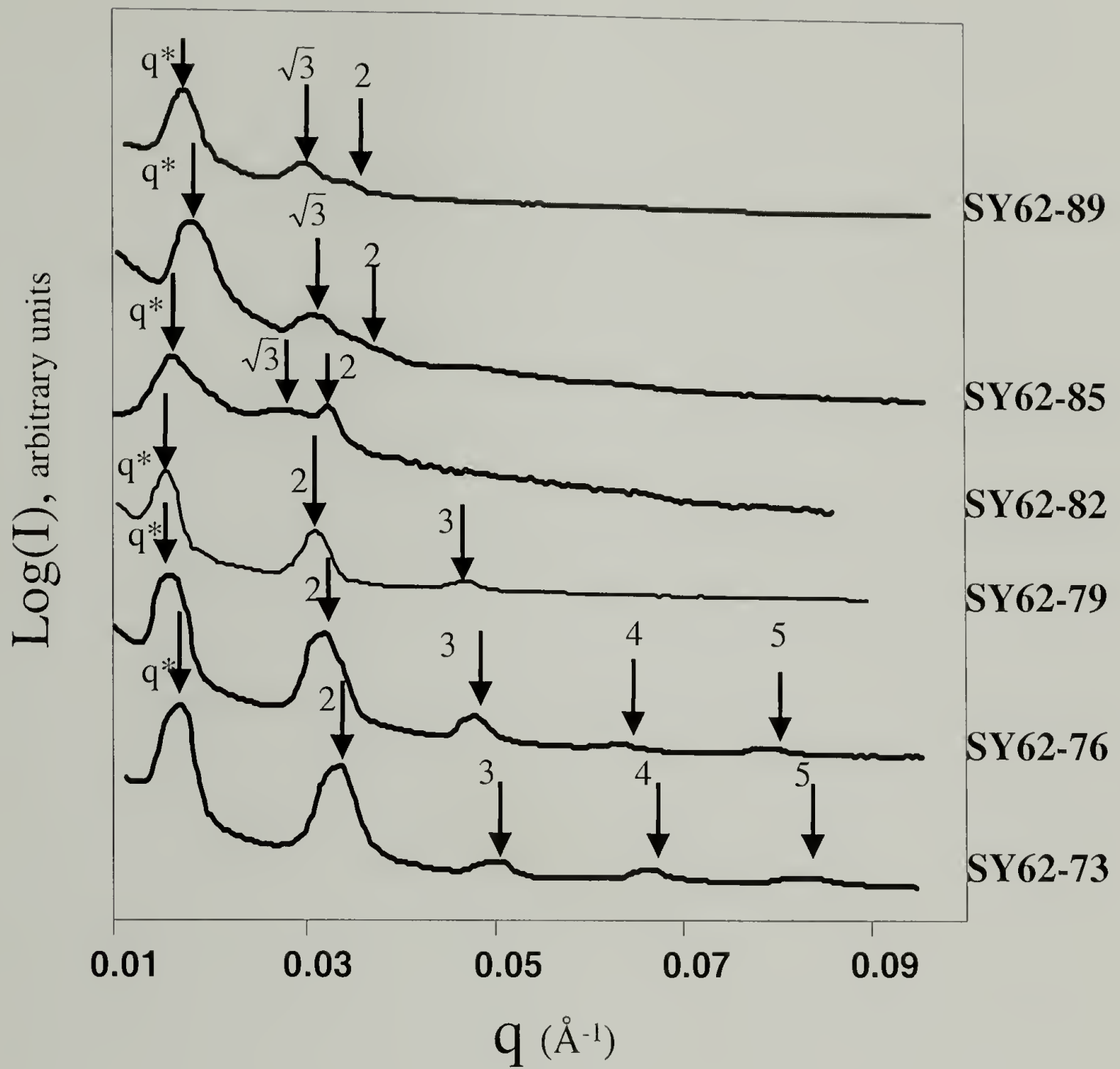
Figure 2.2.   Isotropic SAXS patterns of SY62 series blends azimuthally integrated into one-dimensional plots of log(I) verses q

Figure 2.3.   TEM images of blend SY62-82.

44
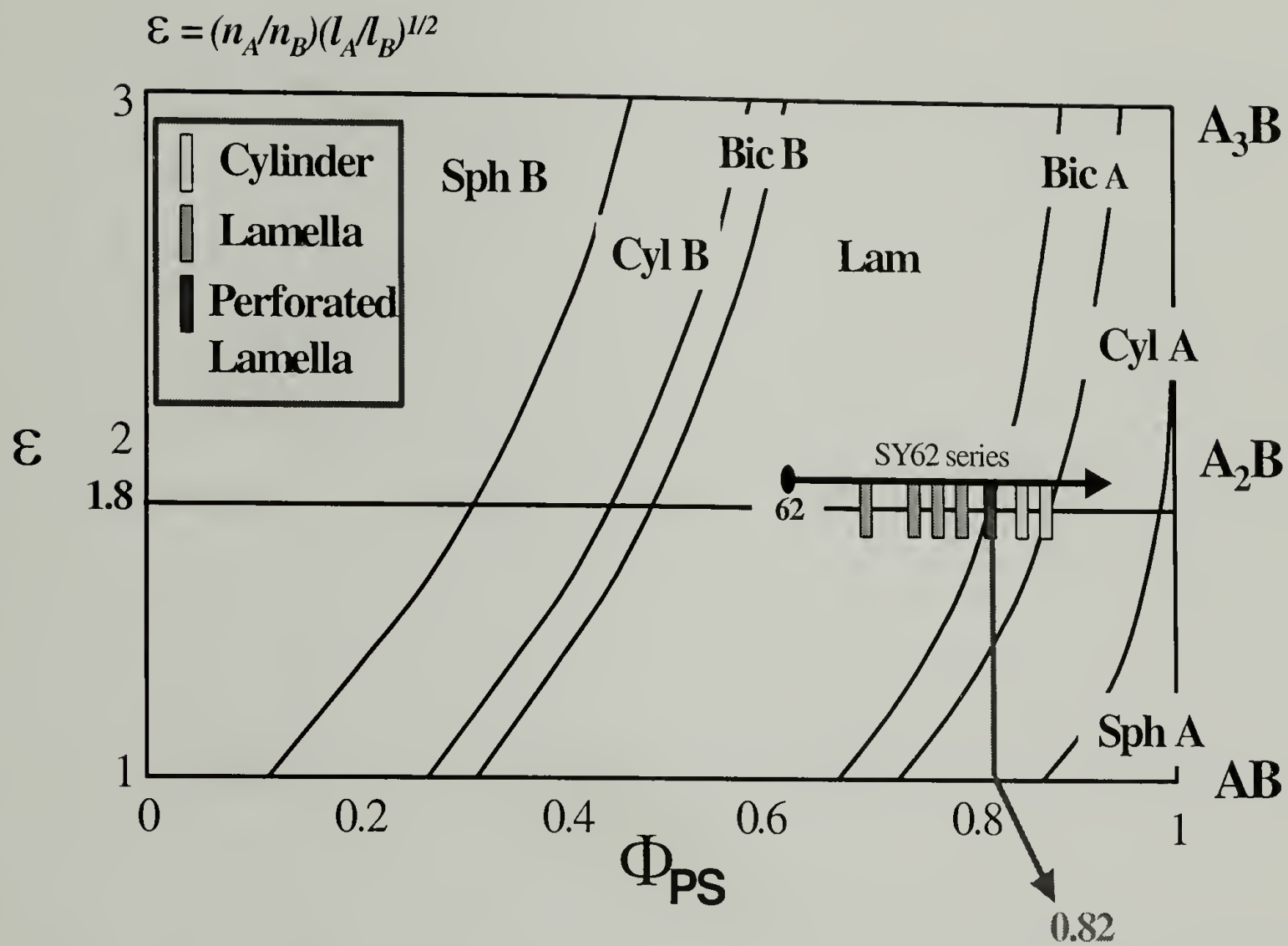
Figure 2.4.   SY62 blend series mapped onto the theoretical morphology diagram. The "62" symbol along the solid at $\varepsilon = 1.8$ indicates the volume fraction of the pure I_2S-62 sample upon which the blends are based. The small rectangular boxes indicate the volume fraction of each blend in the series. The shading of the boxes indicates the morphology.
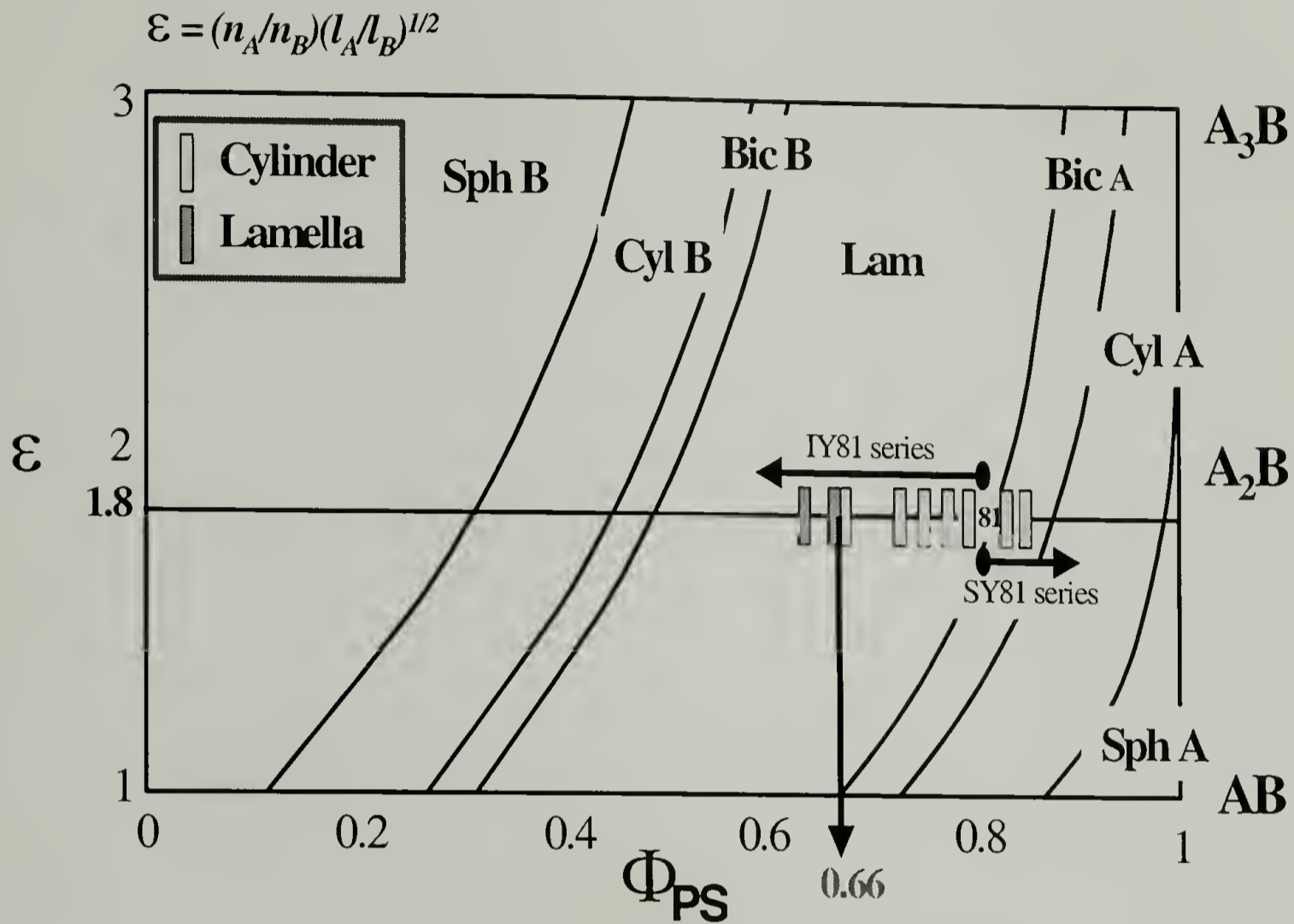
Figure 2.5.   S81 and IY81 blend series mapped onto the theoretical morphology diagram. The "81" symbol along the solid at $\varepsilon = 1.8$ indicates the volume fraction of the pure I_2S-81 sample upon which the blends are based. The small rectangular boxes indicate the volume fractions of each blend. The shading of the boxes indicates the morphology.

46

500 nm

47
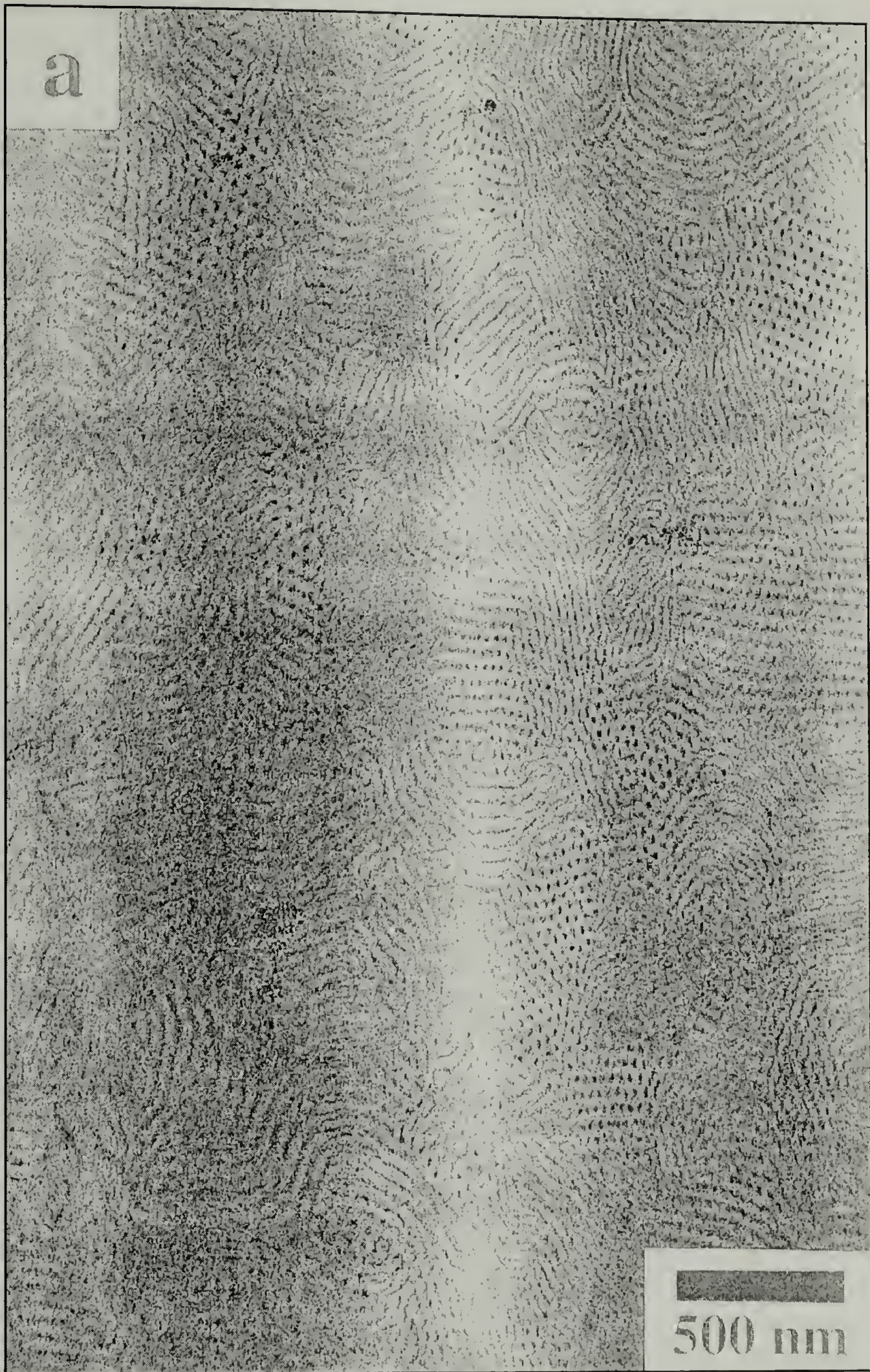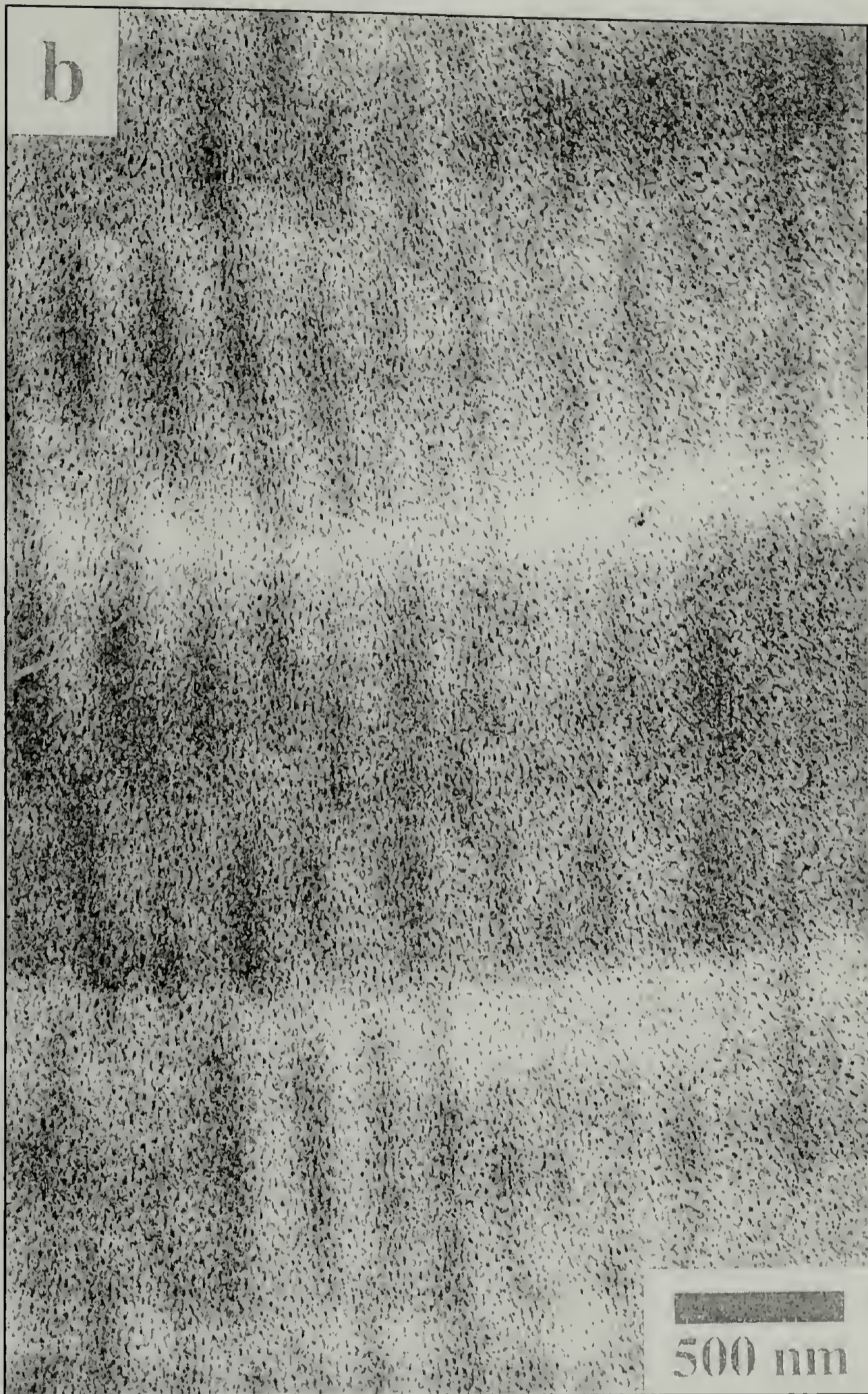
Figure 2.6.   TEM micrographs of blends in the SY81 series. (a) SY81-82 showing projections both parallel and perpendicular to the PI cylinders. (b) SY81-85 showing microphase separated but not well ordered morphology.
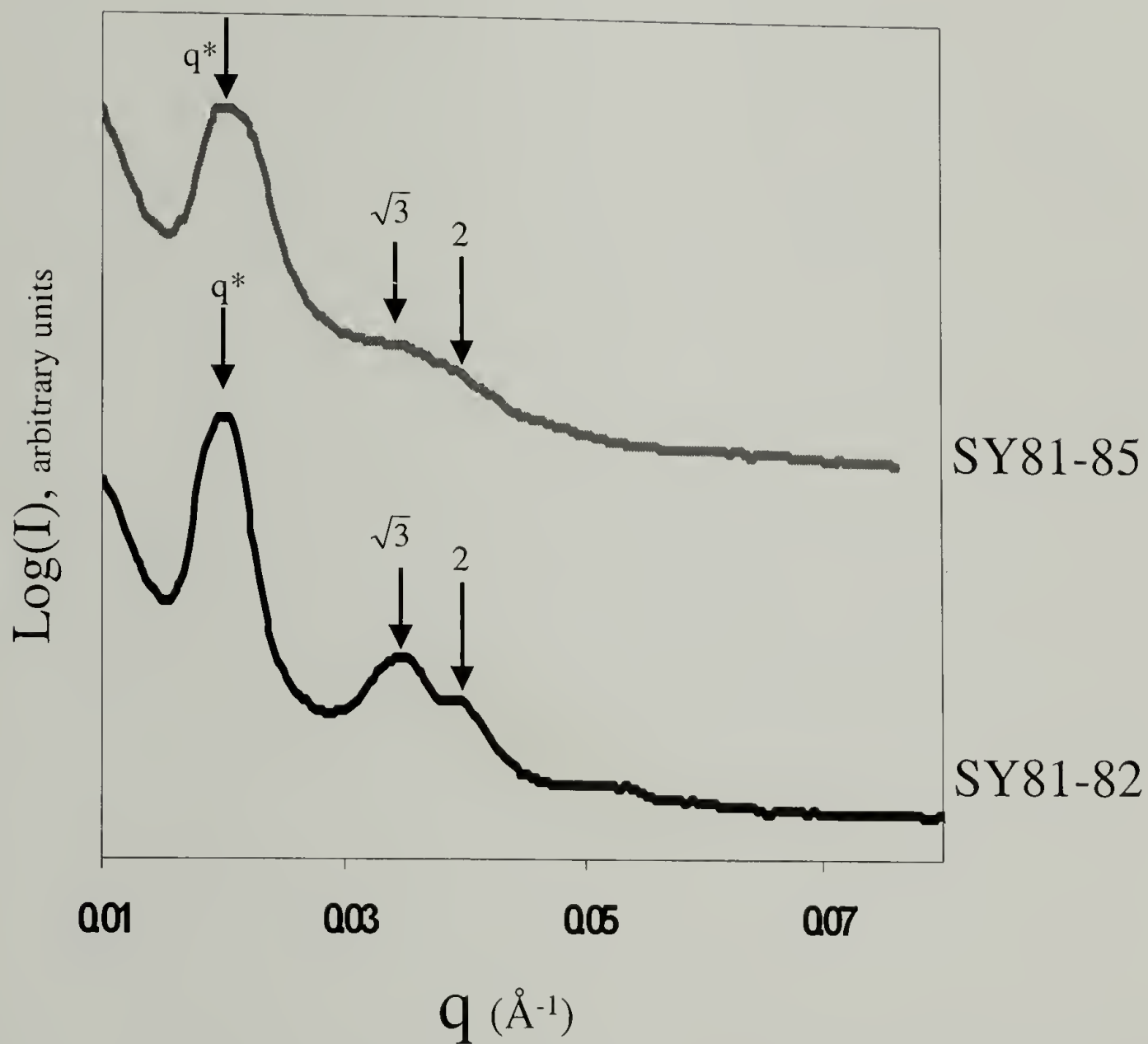
Figure 2.7.   Isotropic SAXS patterns of SY81 series samples azimuthally integrated to give plots of log(I) verses q.
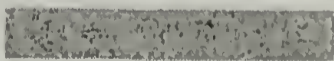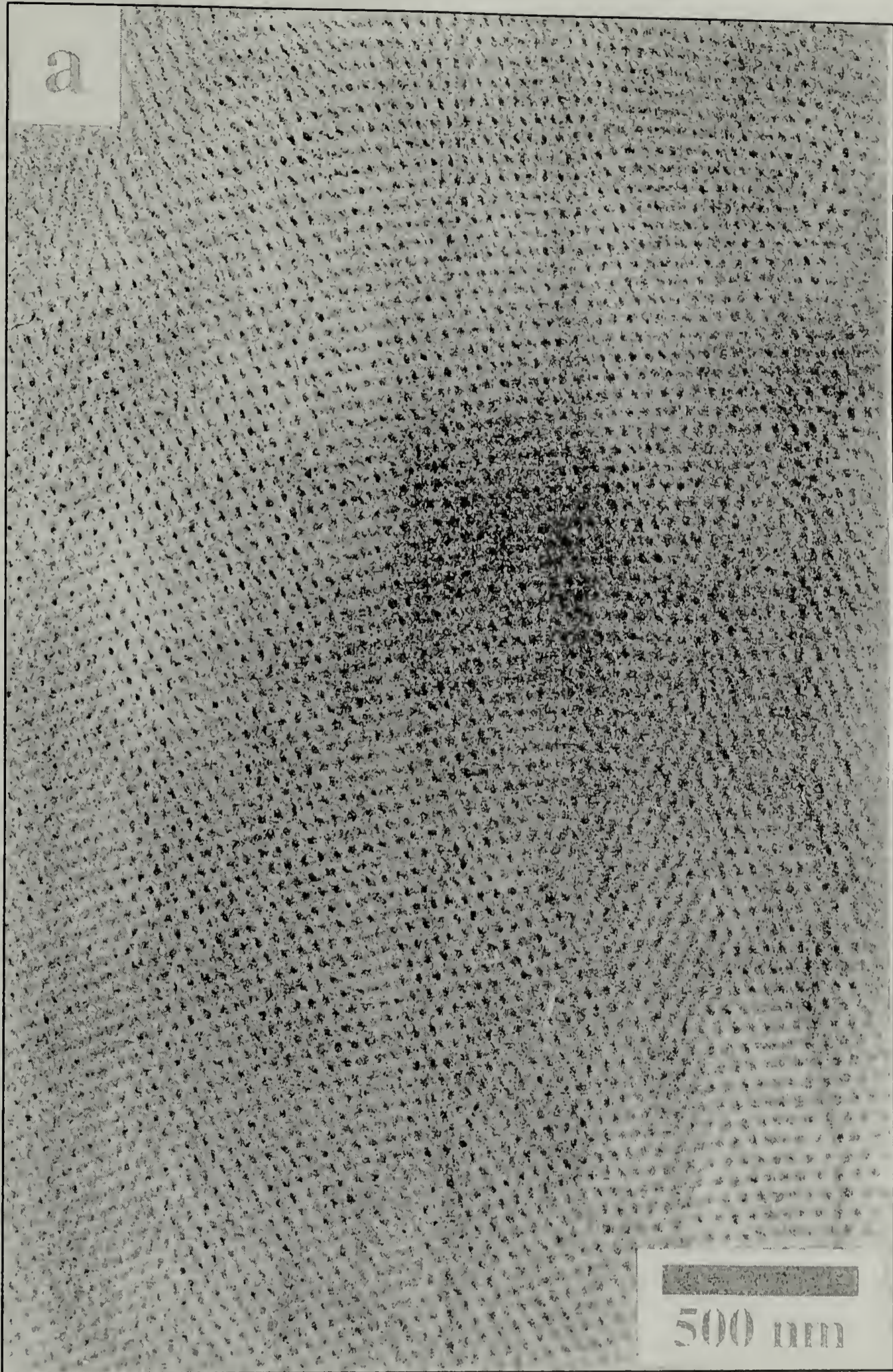
500 nm
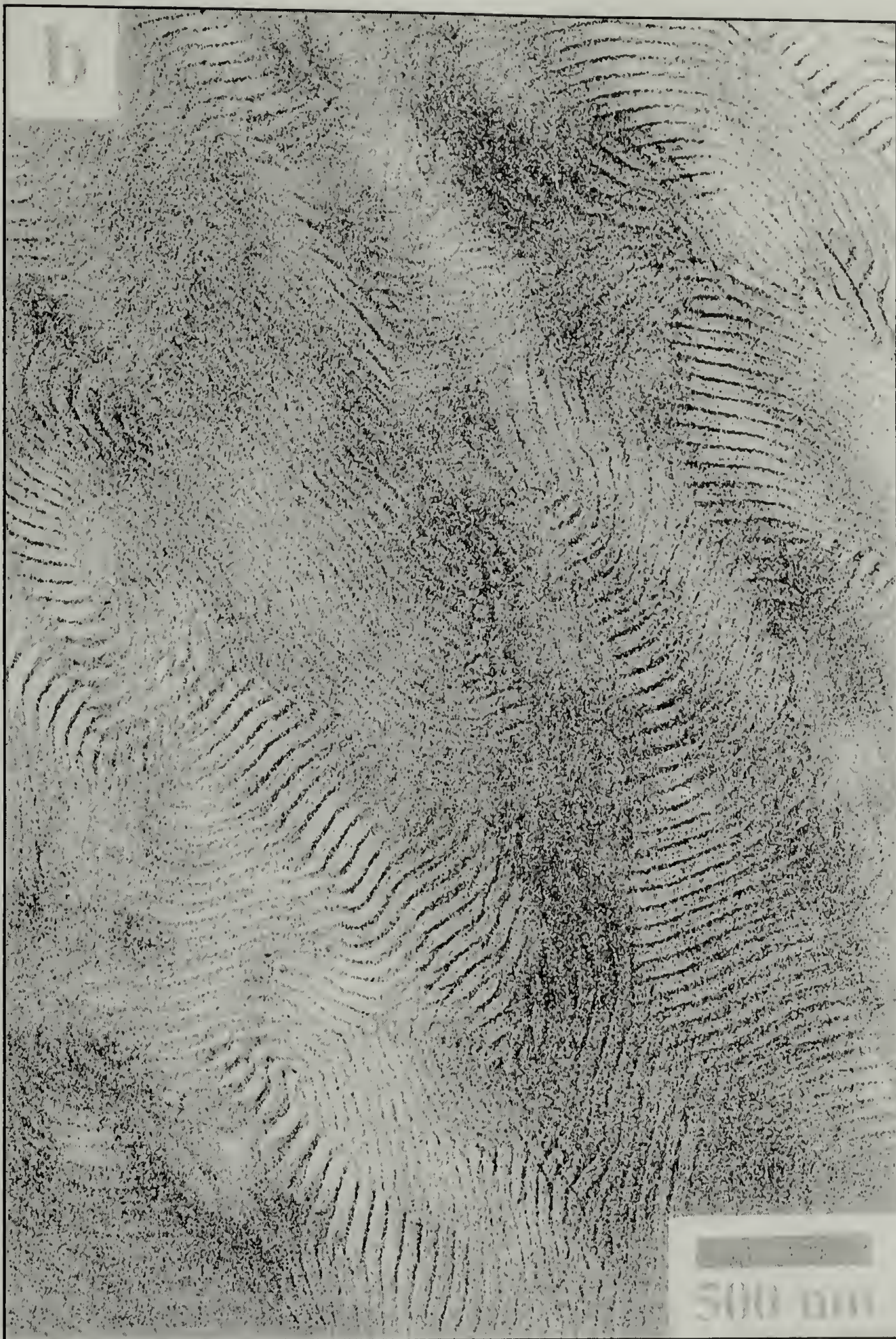
Figure 2.8.   TEM micrographs from the IY81 series.   (a) IY81-66 showing a projection perpendicular to PI cylinders. (b) IY81-65 showing a lamellar structure.

51
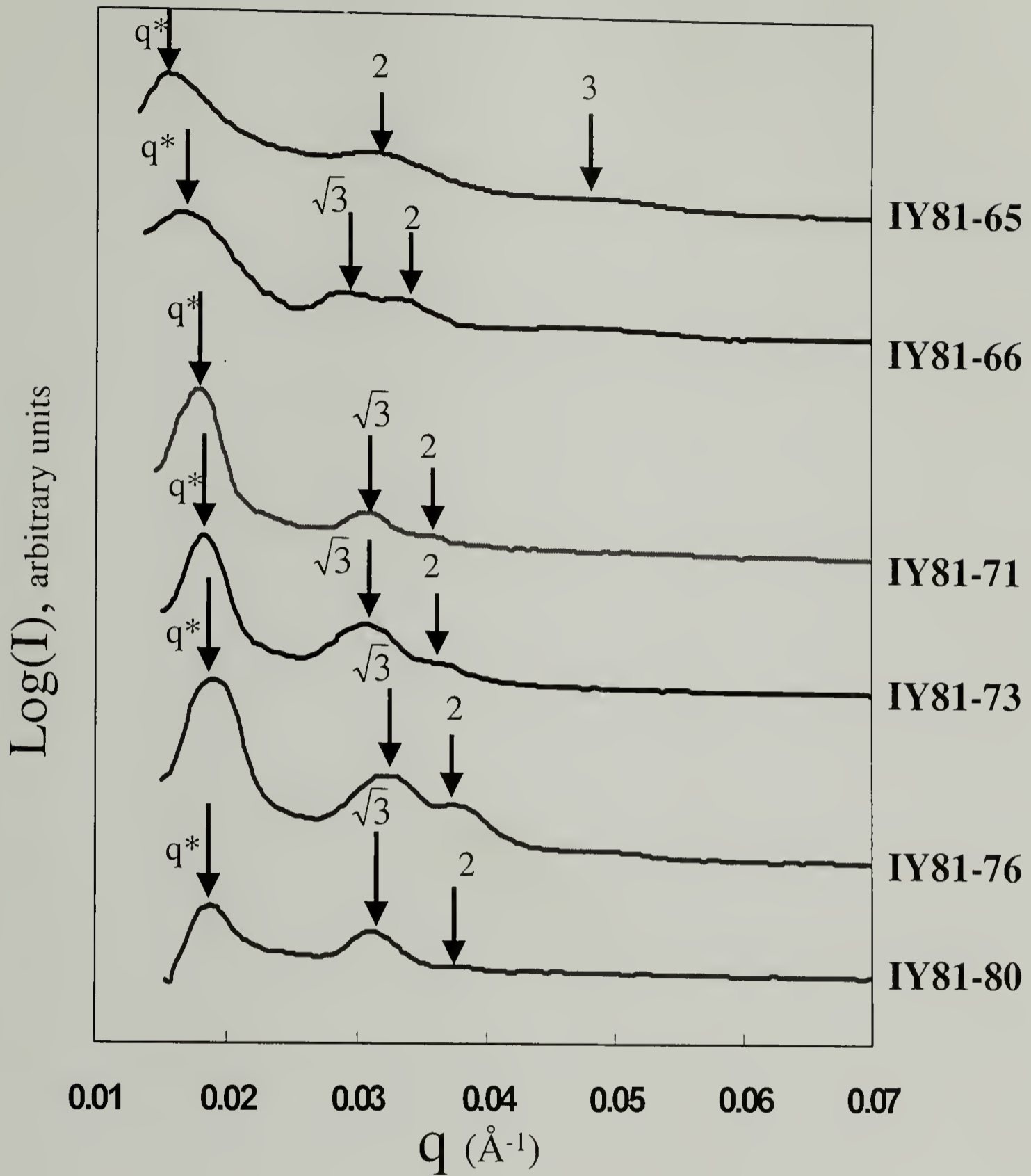
Figure 2.9. Isotropic SAXS patterns of IY81 series samples azimuthally integrated to give plots of log(I) verses q.

500 nm

500 nm

53
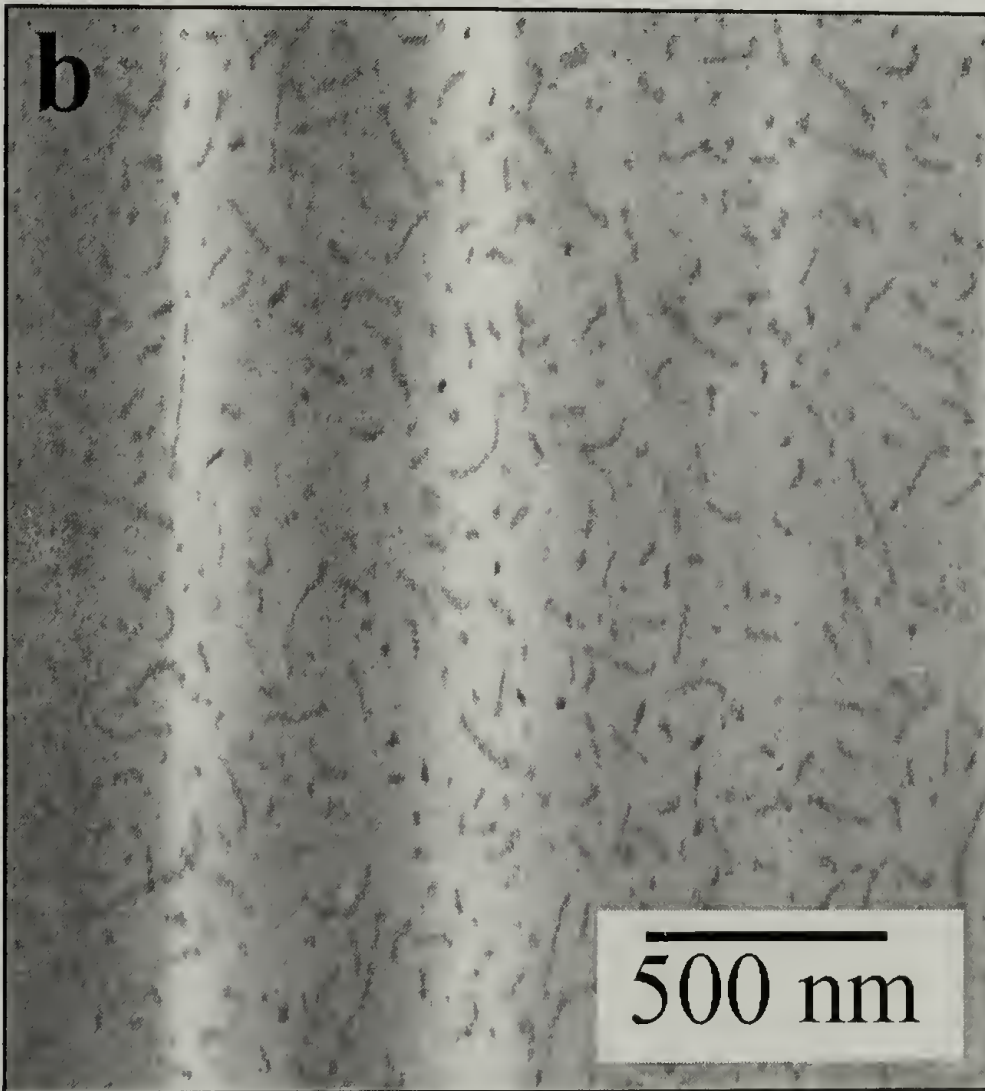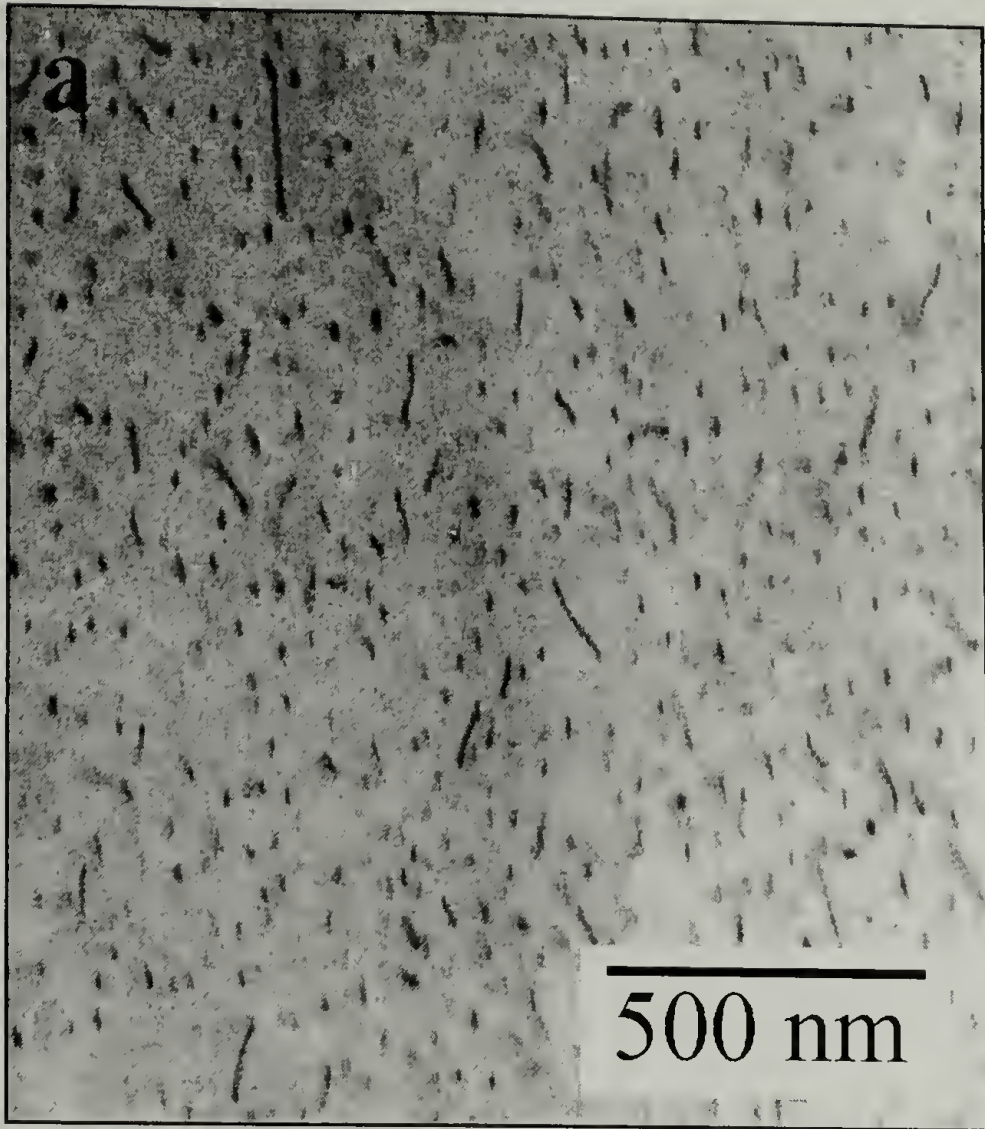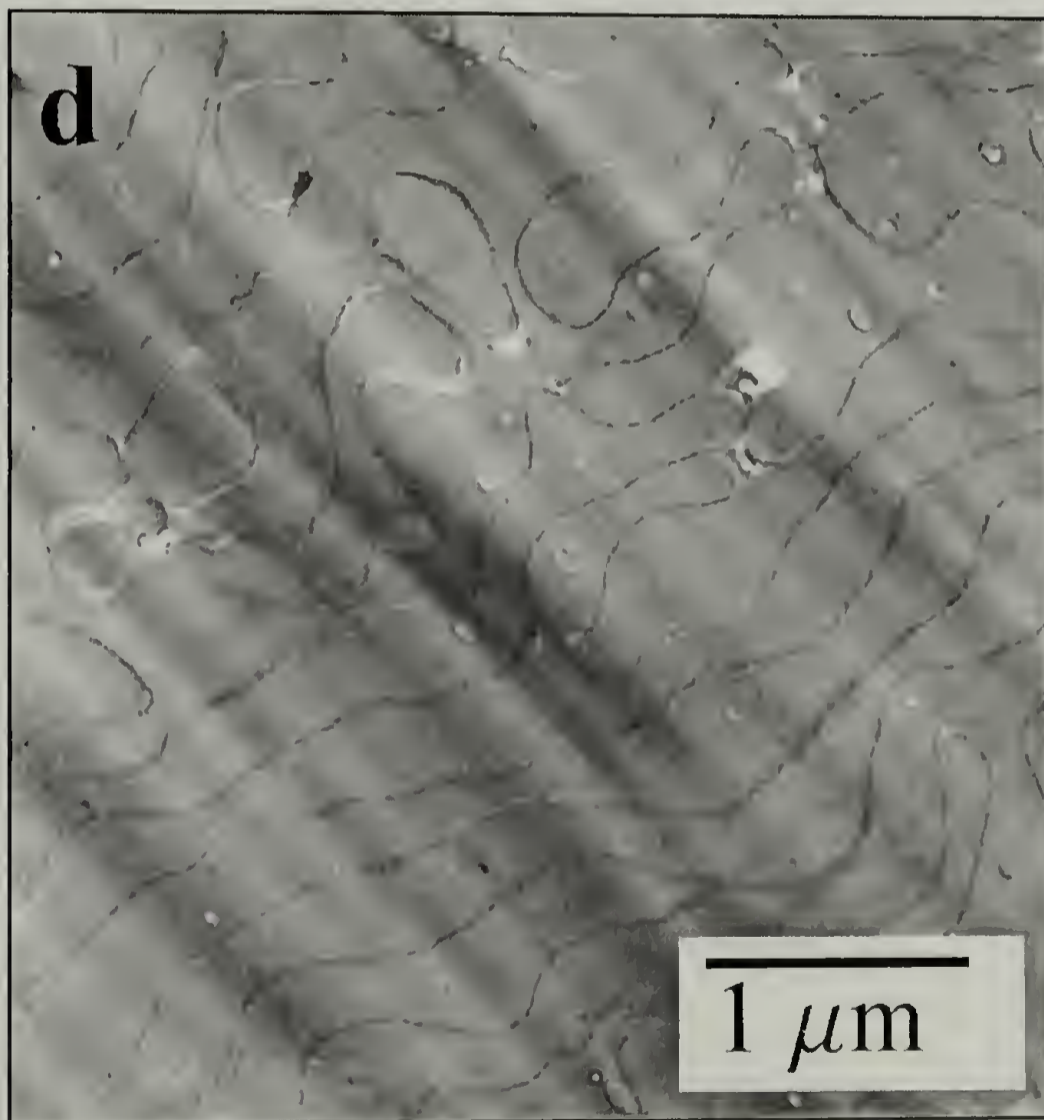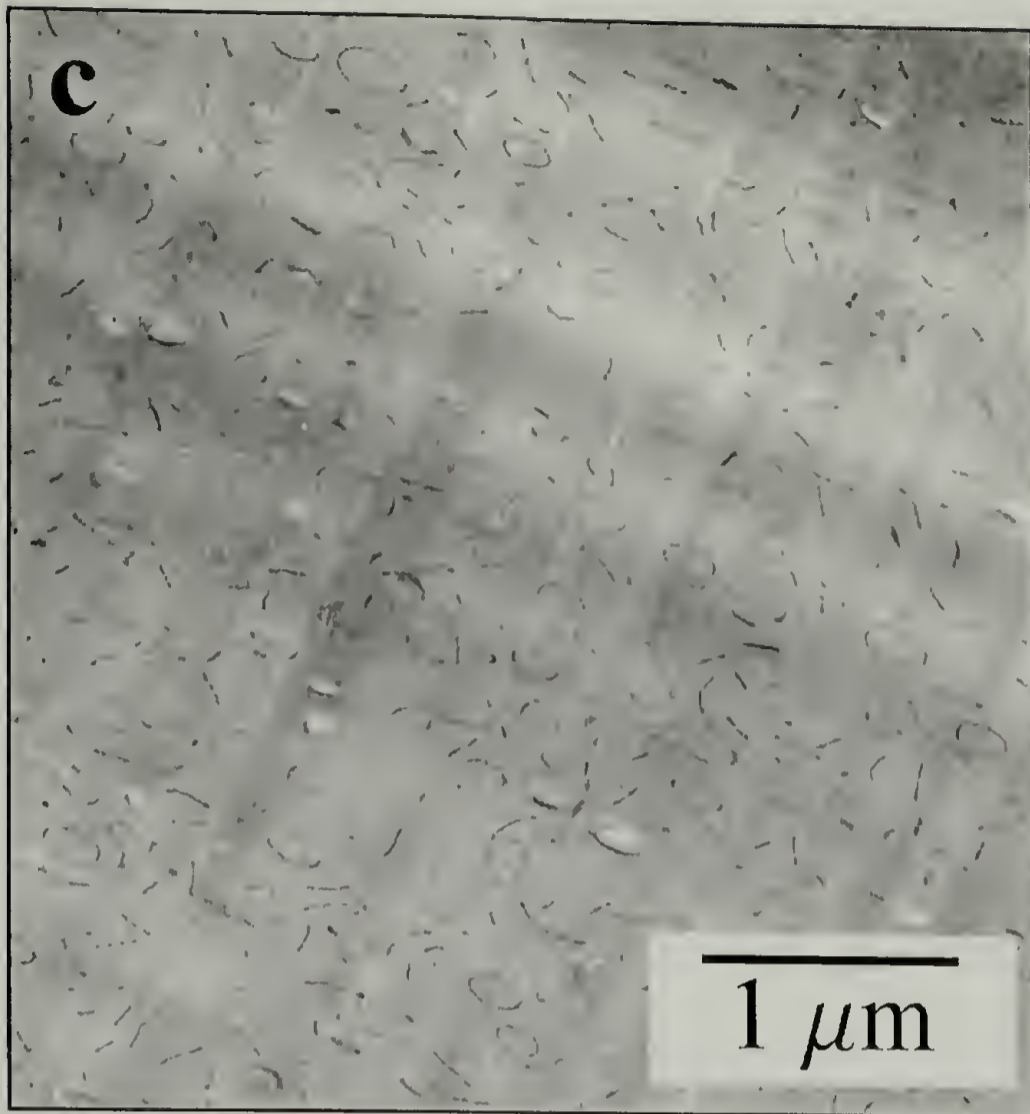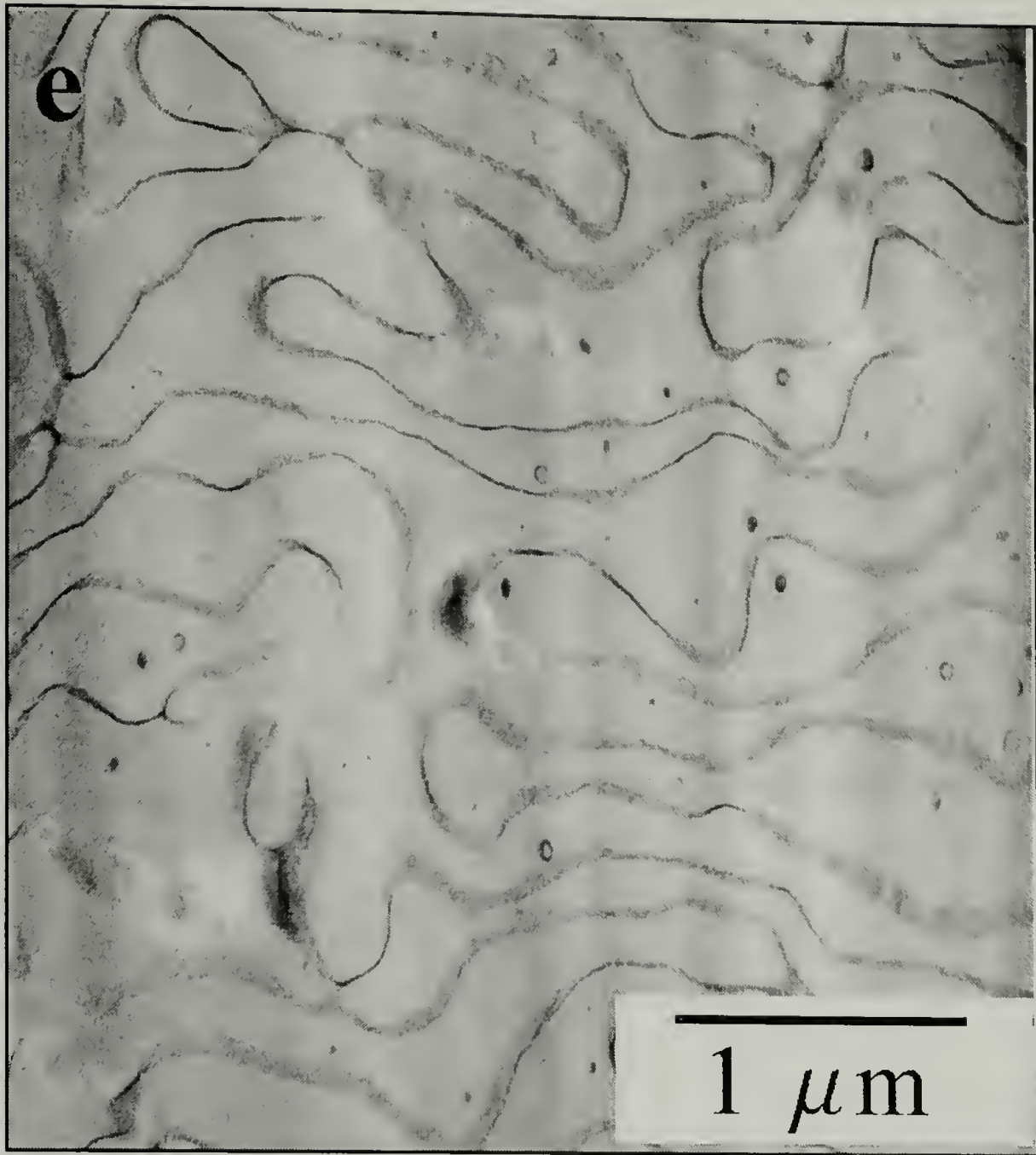
Figure 2.10. TEM image of IY89 series. a) I_2S-89, b) IY89-86, C) IY89-82, d) IY89-80, e) IY89-71
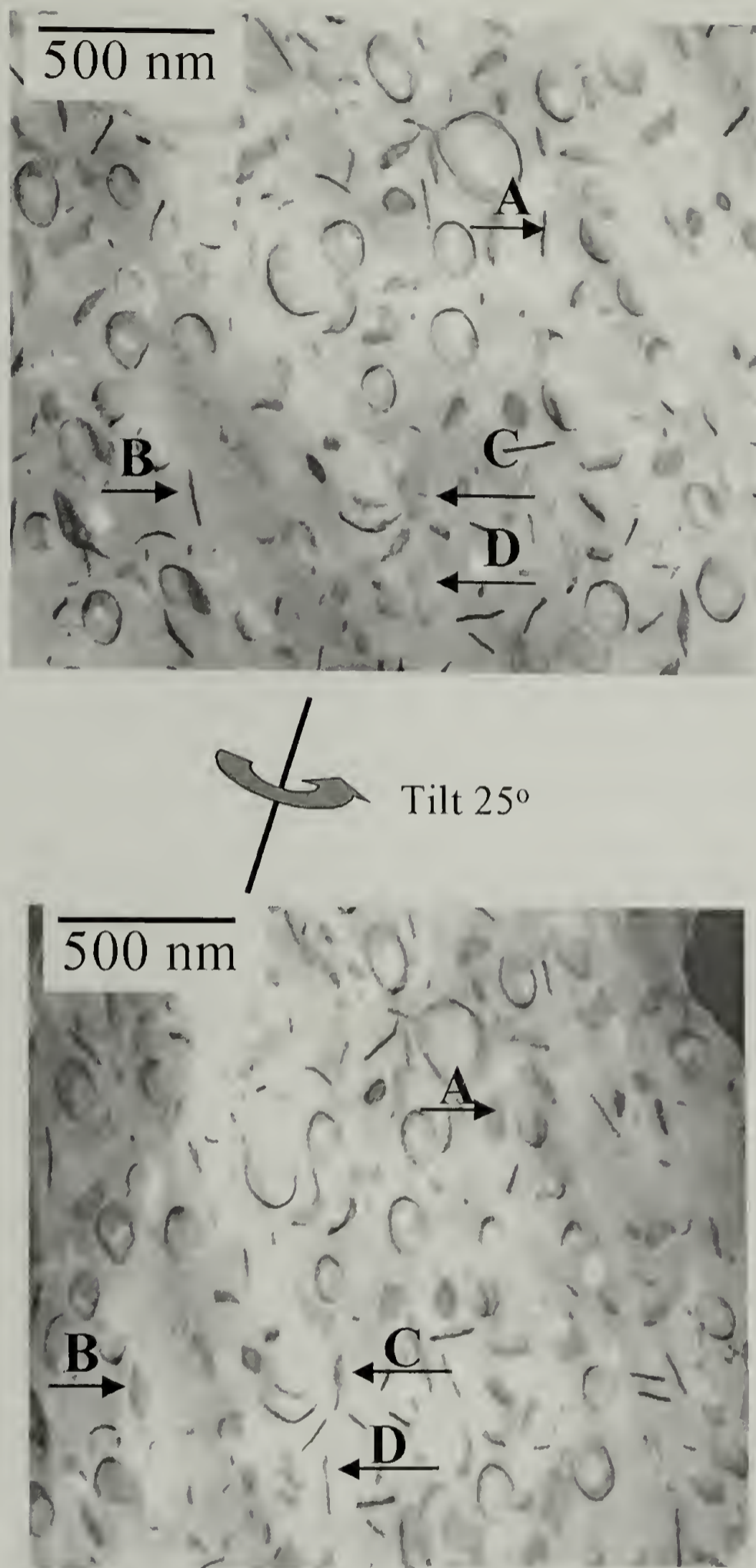
Figure 2.11. TEM tilt series of IY89-82. (a) 0° tilt. (b) 25° about axis indicated. After tilting, the black PI line segments A and B in (a) become PI sheets in (b). The PI sheets C and D in (a) become line segments in (b).
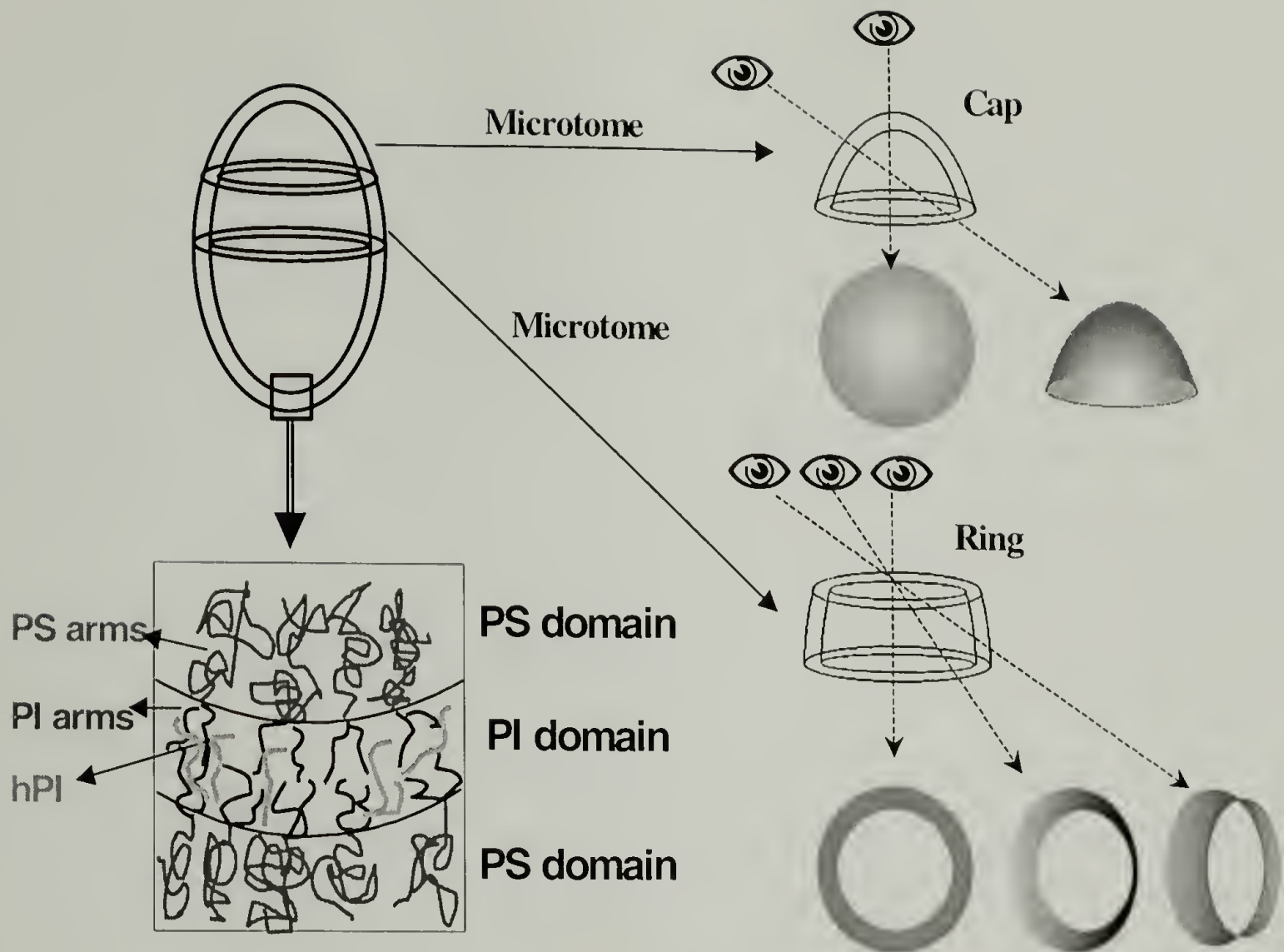
Figure 2.12. Vesicle model. After microtoming, the tops and bottoms of vesicles will appear like caps in TEM projection; the middle parts of vesicles will appear like rings. The rings and caps have different projections with the change of viewing angles and microtome positions.
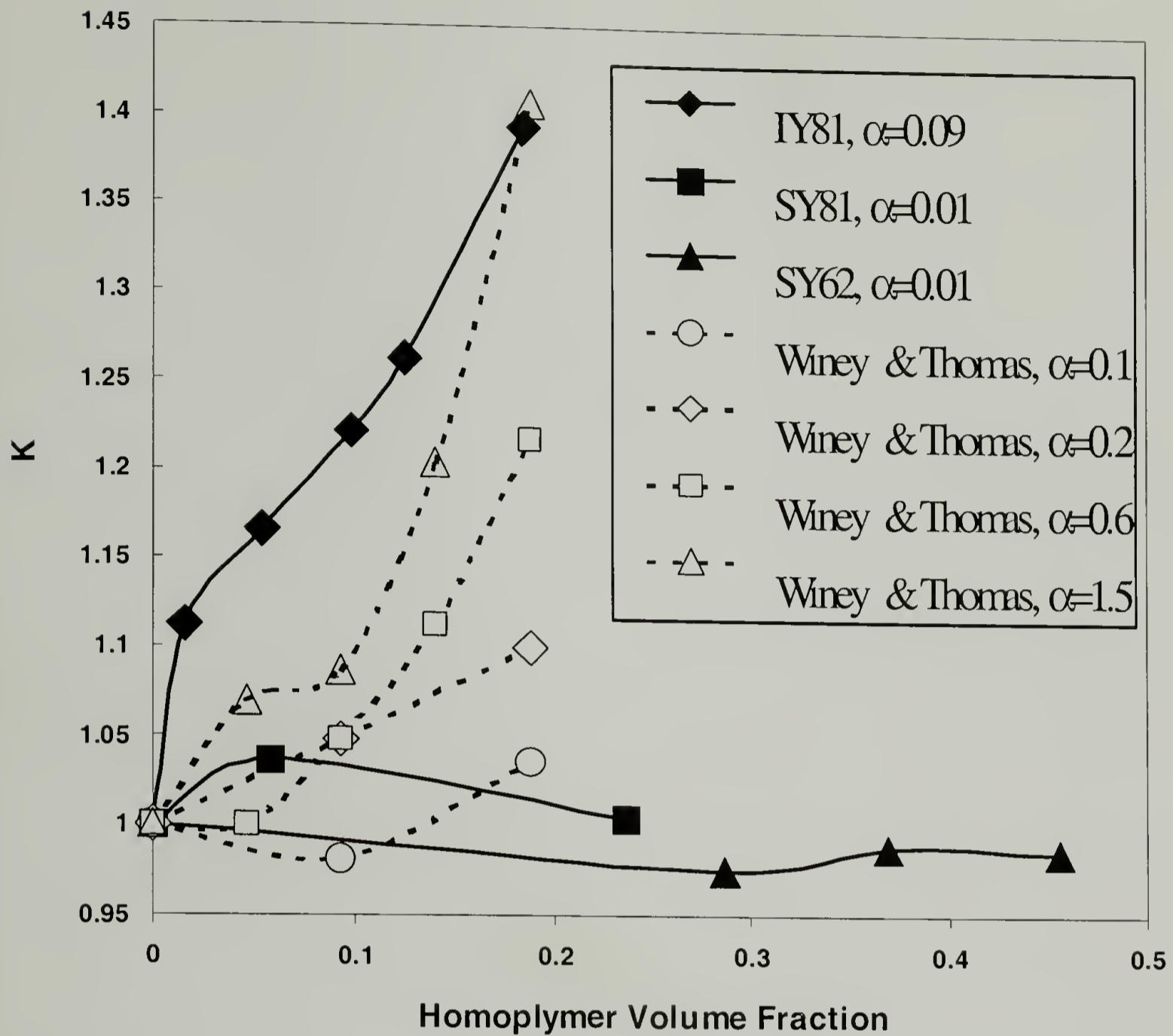
Figure 2.13. Plot of asymmetry swelling ratio, K, verses homopolymer volume fraction for the miktoarm block copolymer / homopolymer blends of this study (filled symbols) and the linear diblock / homopolymer blends studies by Winey, Thomas, and Fetters[19] (open symbols).
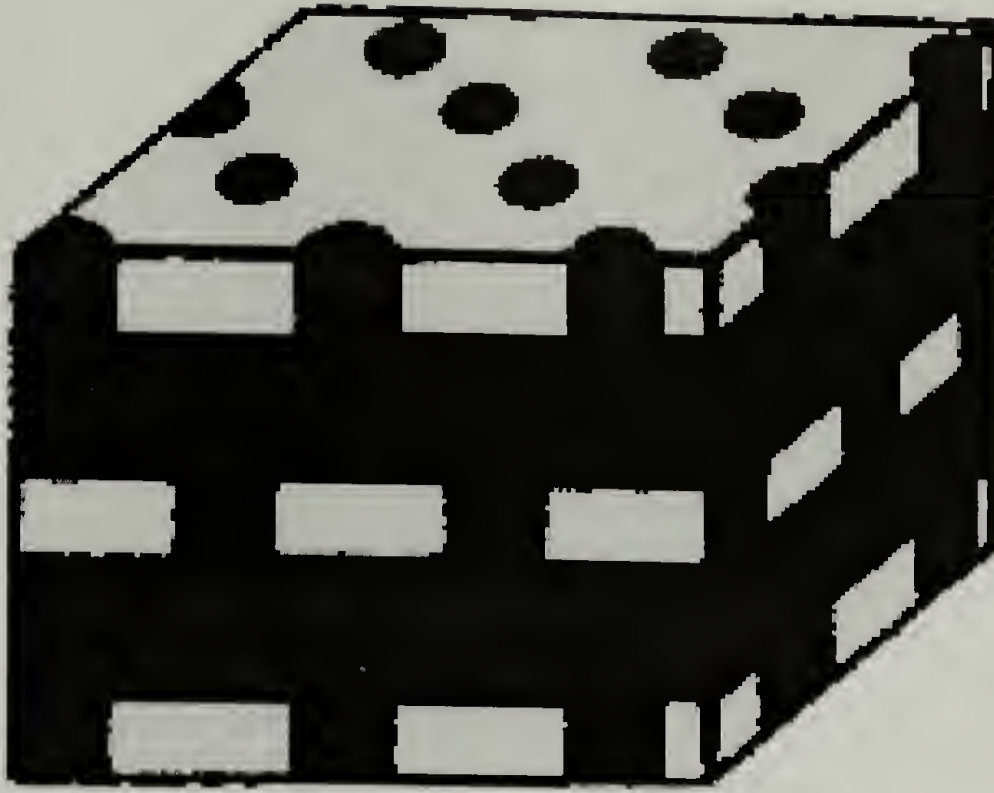
A model suggested by Forster et al .
(Macromolecule, 1994. 27 6922)
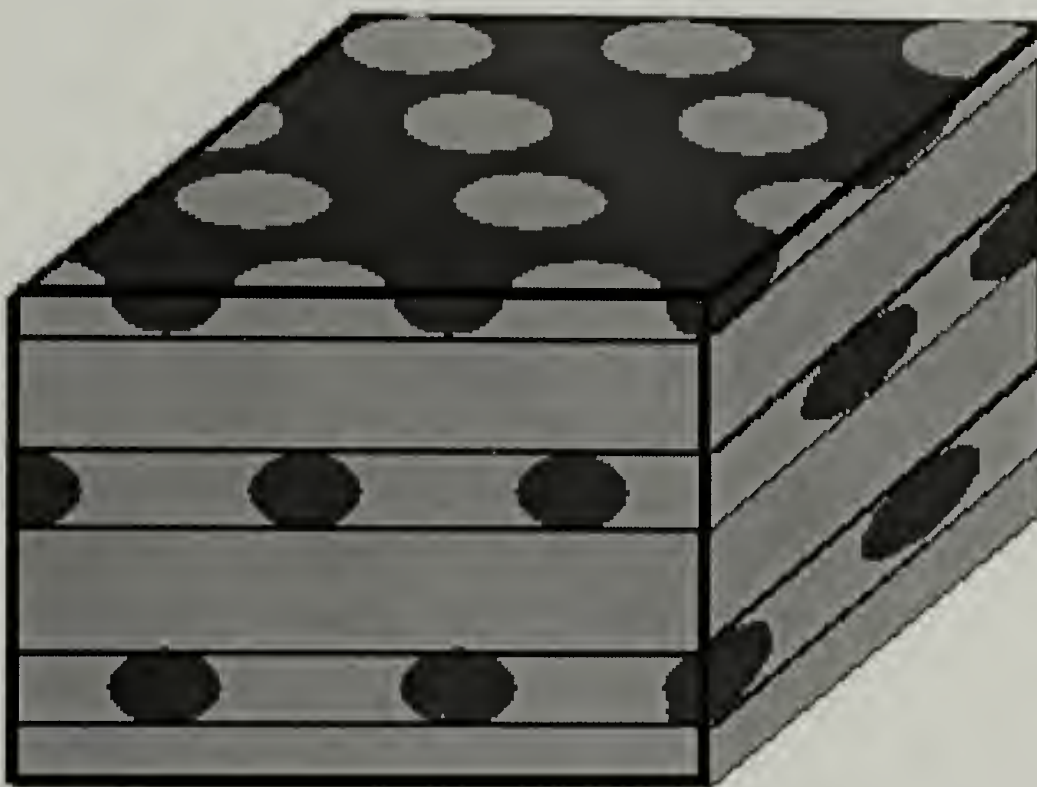
Figure 2.14.   Hexagonally perforated lamella model.
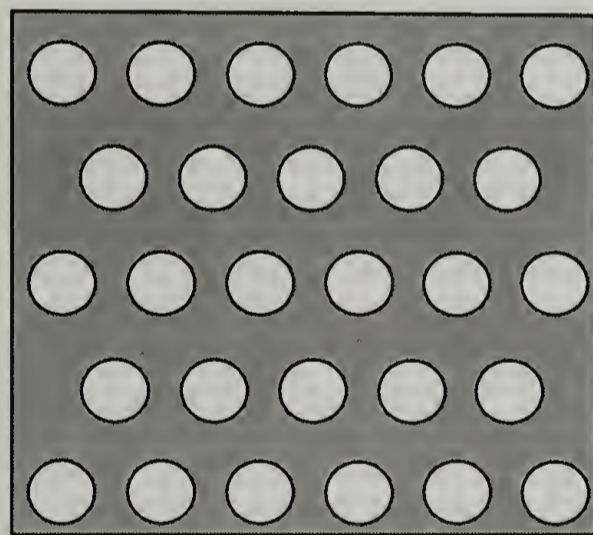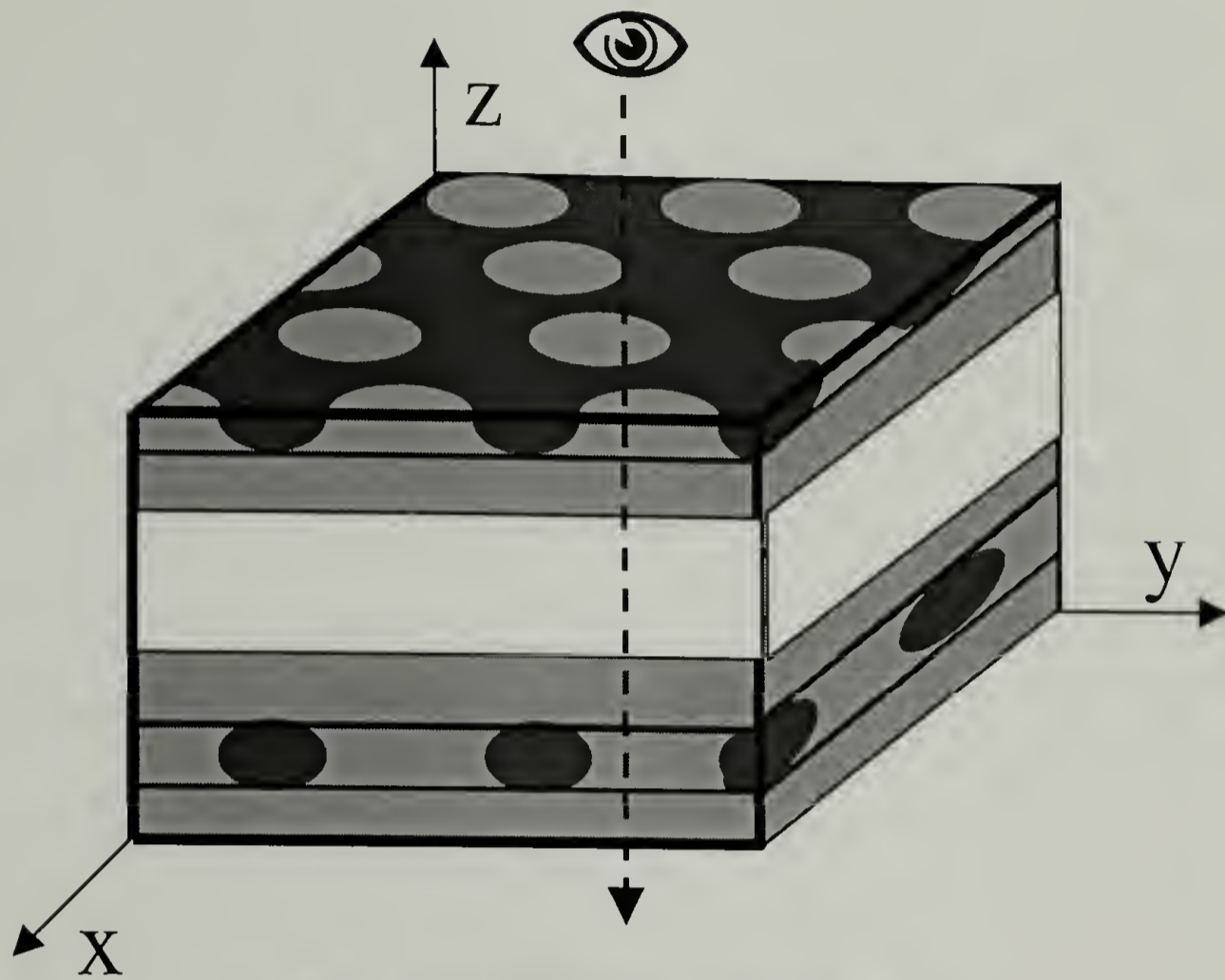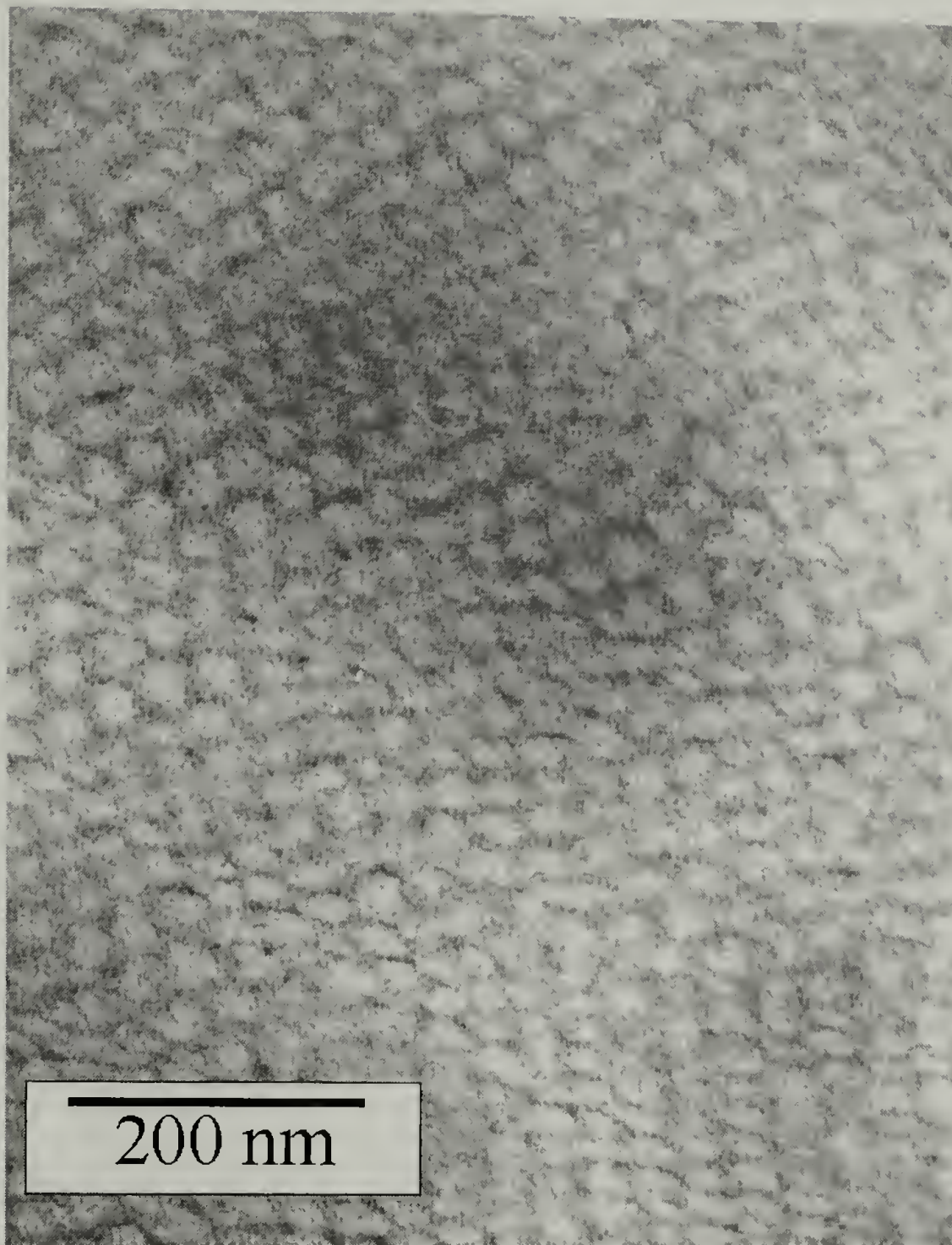
Figure 2.15. The schematic and the TEM micrograph when microtome is parallel to XY plane.
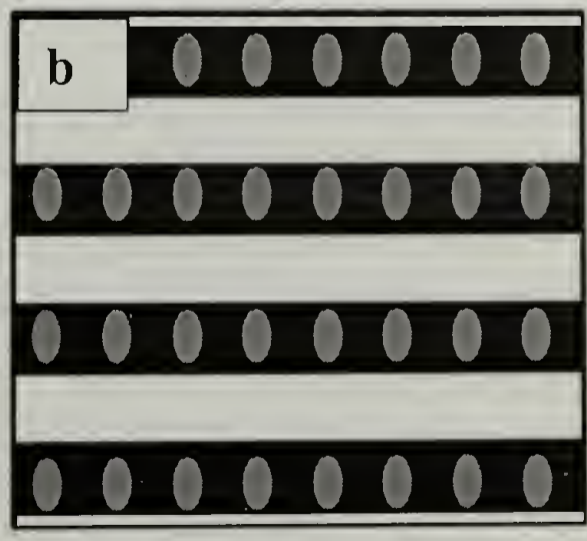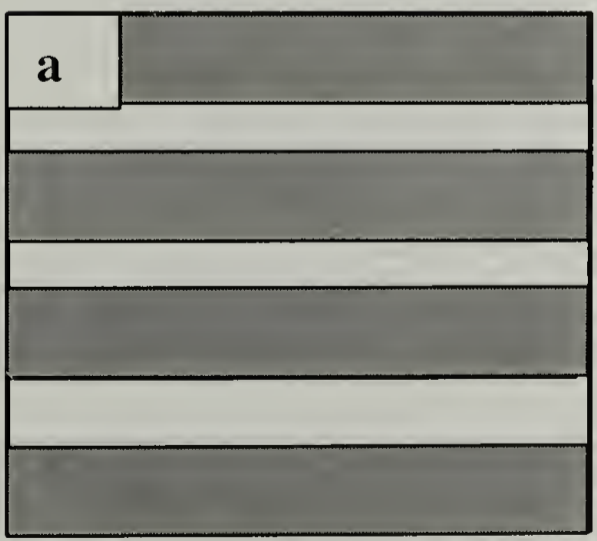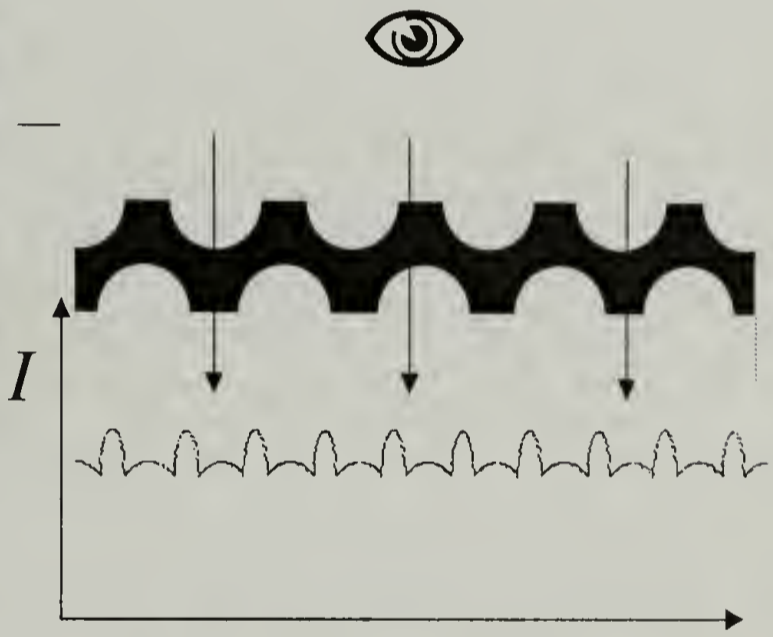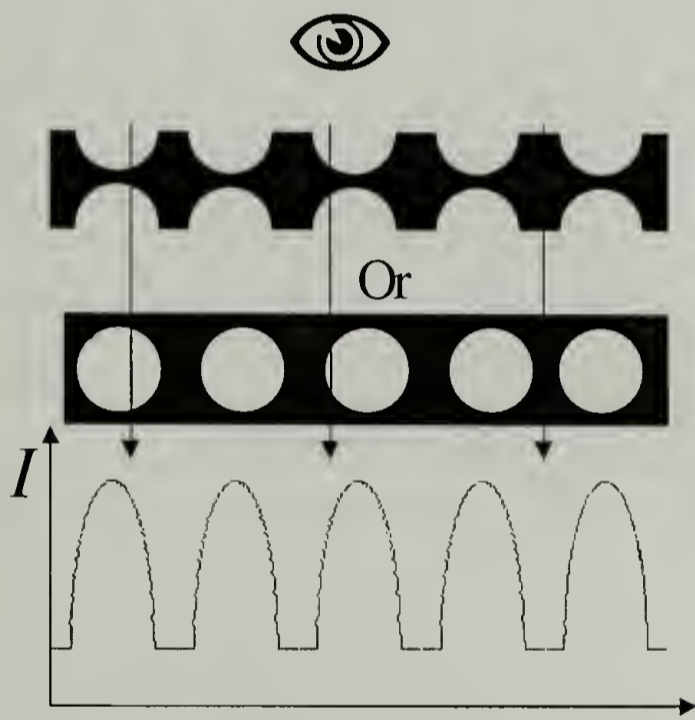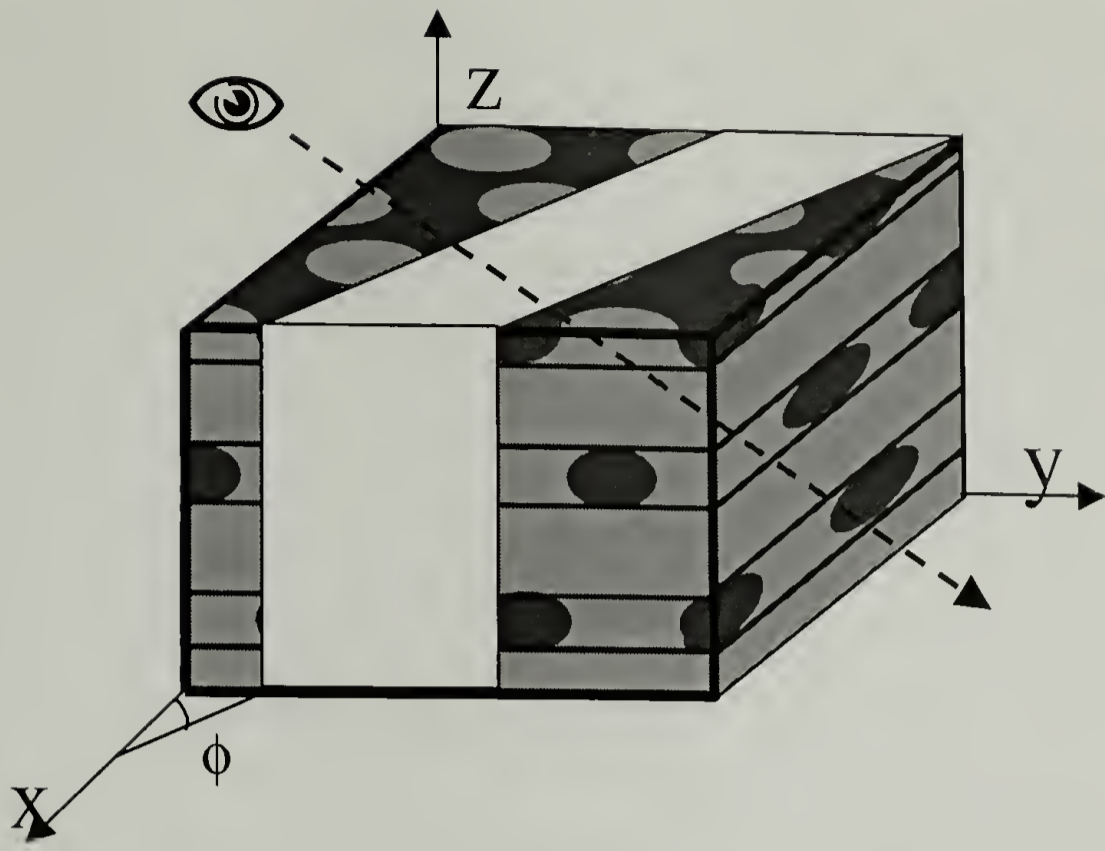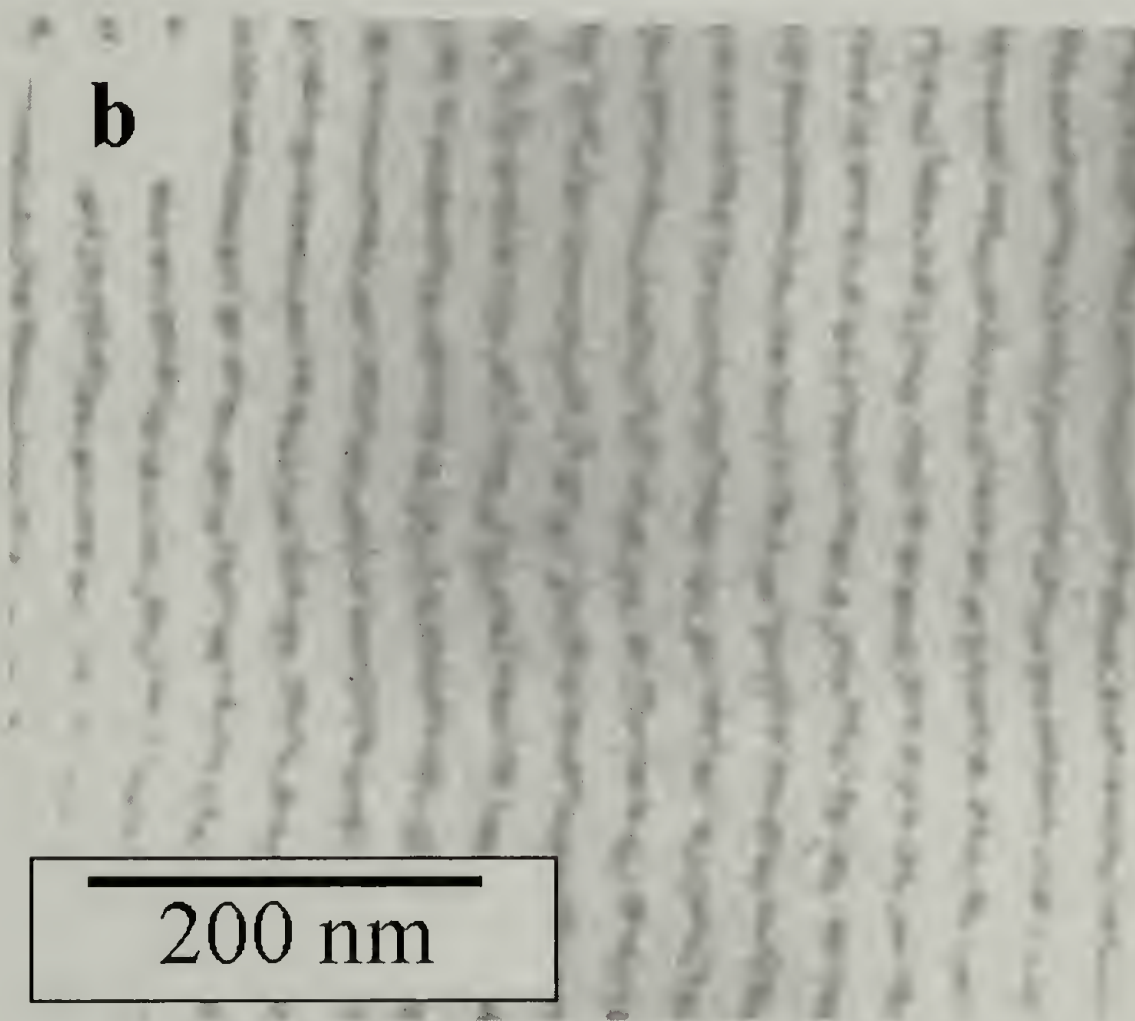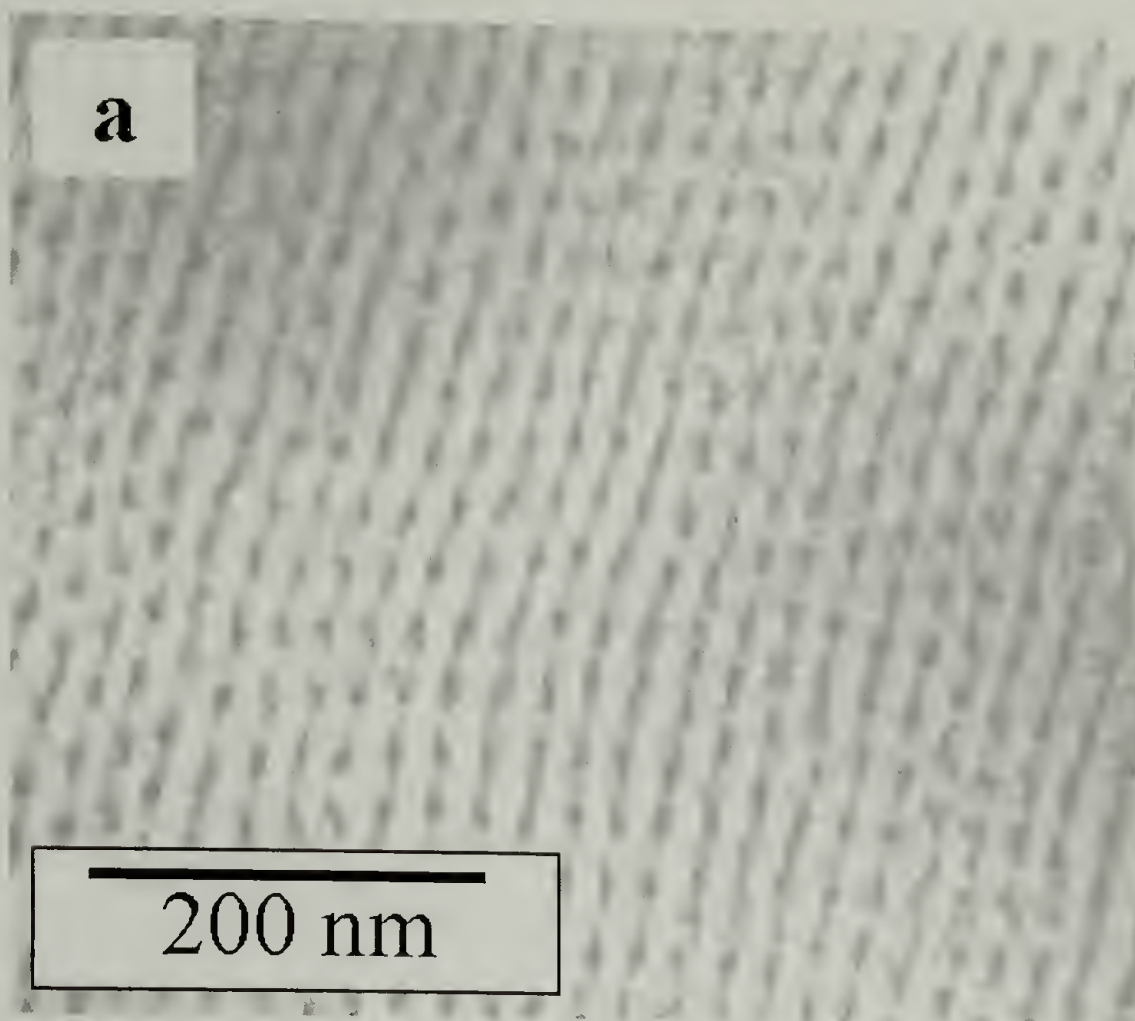
Figure 2.16. The schematic and the TEM micrograph when microtome is perpendicular to XY plane.

A: d/cosθ = b   B: d/cosθ = b

C: d/cosθ = 2b   D: 3b < d/cosθ < 2b

64
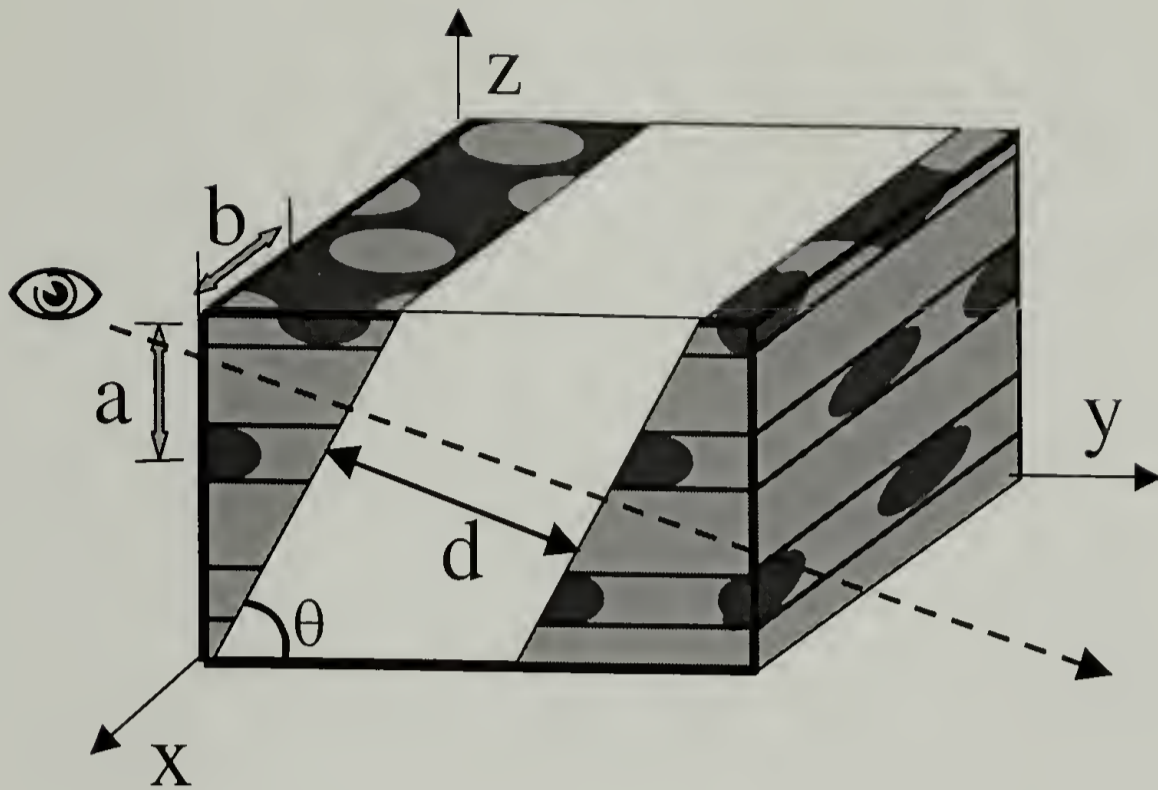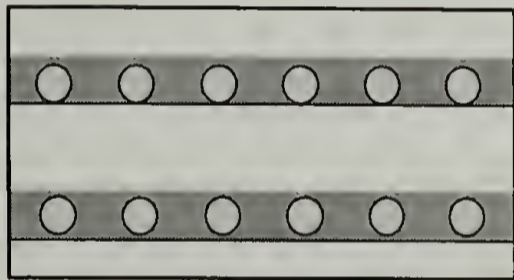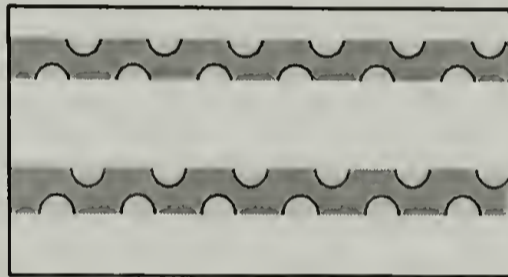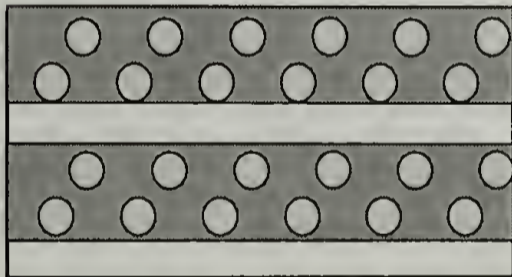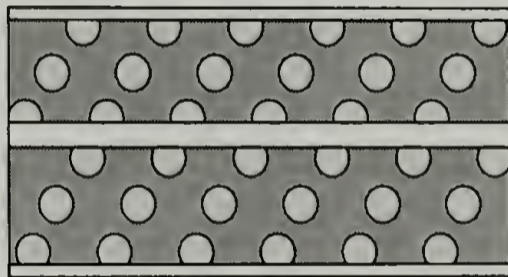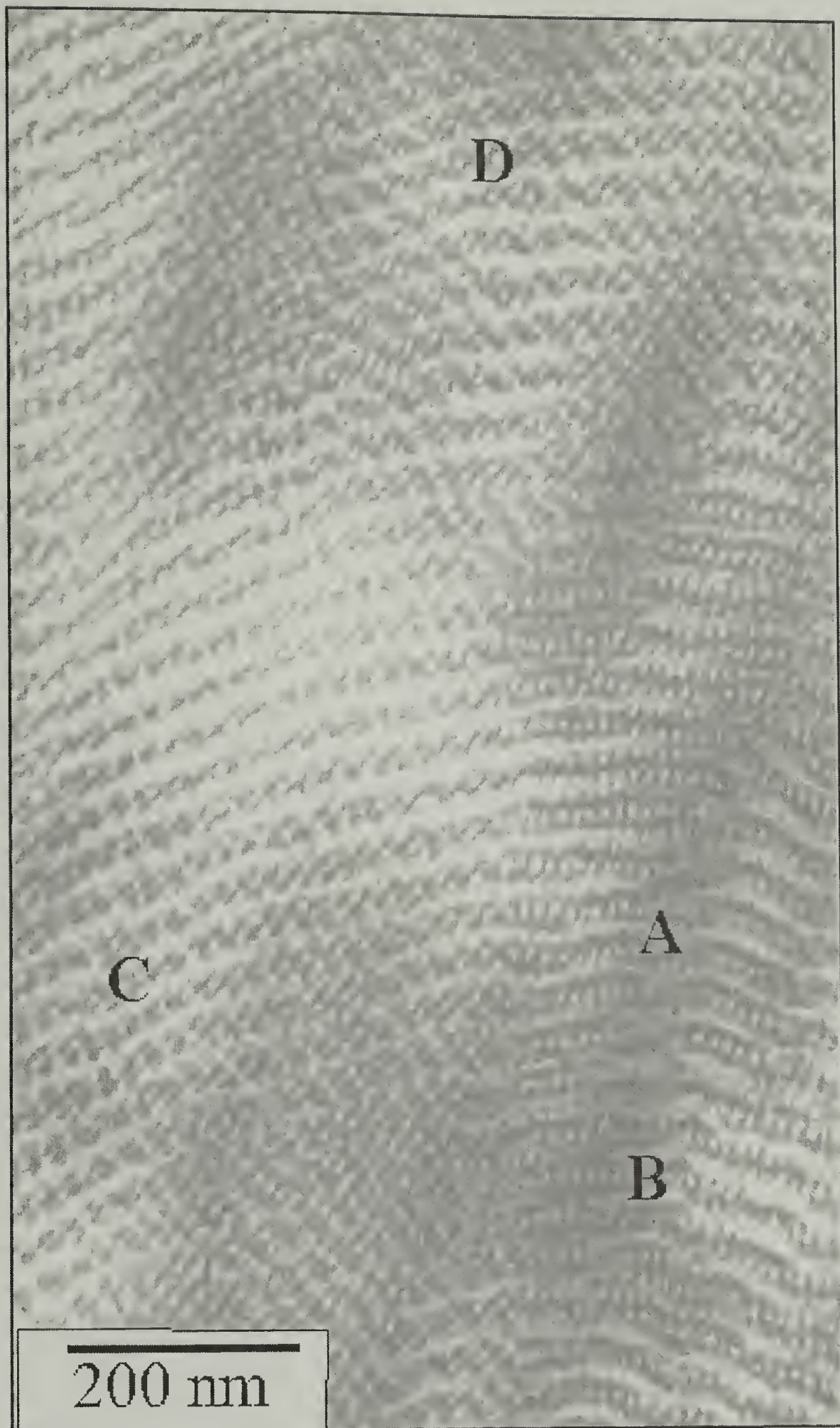
Figure 2.17. The schematic and the TEM micrograph when microtome direction has an angle with XY plane.

CHAPTER 3

MORPHOLOGY BEHAVIOR OF X SHAPED SINGLE GRAPHED BLOCK COPOLYMER / HOMOPOLYMER BLENDS

3.1   Abstract

The morphological behavior of blends of architecturally symmetric, yet non-linear, I_2S_2 miktoarm star block copolymers and homopolymers was investigated using transmission electron microscopy and small angle X-ray scattering. The I_2S_2 block copolymers have two low polydispersity polyisoprene (PI) arms and two low polydispersity polystyrene (PS) arms joined at a common junction point. Previously reported studies of linear diblock copolymer / homopolymer blends showed that the morphology transitions occur at about the same volume fractions as in pure linear diblock copolymers. However, the I_2S_2 block copolymer / homopolymer blends in this study displayed strong shifts in the volume fractions of morphology transitions away from the compositions in which these transitions occur in the pure block copolymer. One of the blend samples formed extremely large and well ordered *single crystals* of the gyroid morphology. SAXS from these single crystals produces as many as 132 diffraction peaks in a single diffraction pattern. Analysis of this data provides the best evidence to date of the $Ia\overline{3}d$ symmetry and Gyroid structure.

66

3.2   Introduction

The effects of non-linear block copolymer molecular architecture on morphology has been studied by various groups using well defined, *model* materials.[2-5,8-10,12,44,87-90,99-101] The present study investigates the effects of non-linear symmetric molecular architecture on the morphology of block copolymer / homopolymer blends using I_2S_2 *mikto*arm star block copolymers. As illustrated in Figure 3.1, I_2S_2 *mikto*arm stars have two polyisoprene (PI) arms and two polystyrene (PS) arms linked at a common junction point. The morphologies of neat microphase-separated I_2S_2 block copolymers have been studied by Beyer, Gido *et. al.*[9] The results of this previous study are plotted in Figure 3.2, on a theoretical morphology diagram for *mikto*arm stars, calculated by Milner.[11] For *mikto*arm stars of type A_nB_m, this theory predicts morphology as a function of B component volume fraction, ϕ_B, and a molecular asymmetry parameter, $\varepsilon = (n_A/n_B)(l_A/l_B)^{1/2}$. Here, n_A and n_B are the numbers of arms of block materials A and B, and $l_i = (V_i/R_i^2) = v_i/b_i^2$. V_i and R_i are volume and radius of gyration of one arm of polymer i, while v_i is the segmental volume and b_i the statistical segment length of component i. The morphologies observed for the A_2B_2 materials showed general agreement with the composition ranges predicted by the theory. However, for some architecturally asymmetric samples, the theory overestimated the degree of shift in the order-order transitions. Studies on S_2I, I_2S, I_3S, and I_5S showed qualitative agreement but quantitative disagreement.[7-9,87,89,90,102] Since the I_2S_2 samples have a symmetric molecular architecture, the conformational asymmetry between PI (the A component) and PS (the B component) is the only contributor to the molecular asymmetry, resulting in an asymmetry value of $\varepsilon \approx 0.85$. Since the ε value is smaller

67

than 1, we have extended the morphology diagram to include ε values from 1/2 to 1. The morphology diagram is calculated for pure *mikto*arm star block copolymers. In this study, we will use it as a guide to thinking about the effects of homopolymer blending on the morphological transitions of I_2S_2 block copolymer systems.

Blends of linear diblock copolymers with homopolymer as well as blends of linear multi block copolymers with homopolymer have been extensively studied.[13-25] Previously reported results for linear diblock copolymer / homopolymer blends showed that the order-order transitions (OOTs) occur at about the same volume fractions as in pure linear diblock copolymers. The OOT occurs at the same volume fraction regardless of the direction from which it is approached, i.e. blending homopolymer A with a diblock which forms A cylinders in a B matrix to push it toward lamella or blending B homopolymer with a lamellar diblock to push it back toward cylinders.[17,18,20] However, for architecturally asymmetric graft copolymers, blending homopolymer into the one arm side or into the multi-arm side of the interface may produce different morphological results. In a recent study by Yang, Gido *et.al.*[54] A shift in OOT volume fraction is observed when blending homopolymer with the two-arm side of an architecturally asymmetric I_2S block copolymer. The current study involves block copolymer materials that, although architecturally symmetric, also have nonlinear molecular structures.

In the present investigation, low molecular weight homopolymers of polystyrene (hPS) or homopolymer polyisoprene (hPI) are blended with I_2S_2 block copolymers to push the morphology transitions. Table 3.1 lists the molecular

characteristics (molecular weights, volume fractions, polydispersities) and morphologies of the neat I_2S_2 block copolymers used in this study as well as the molecular weights and polydispersites of the homopolymers. We use low molecular weight (MW) homopolymer in all the blend systems so that the distribution of the homopolymer within the block copolymer domains of like material is relatively uniform.[14,19,91,95]

A microphase separated, bicontinuous, block copolymer structure with a cubic symmetry was identified as ordered bicontinuous double diamond (OBDD) with Pn3m symmetry by Thomas and coworkers,[44] and the Hashimoto group,[45] in the mid-1980's. In 1994, Thomas and co-workers[46] and Bates and co-workers[38] amended the structure of the cubic bicontinuous morphology, proposing that it was actually a gyroid structure with $Ia\bar{3}d$ symmetry. SAXS evidence for the gyroid structure was provided by powder patterns with up to 13 reflections,[38] and single crystal scattering patterns with up to 10 reflections.[37-39,47] In this study, we obtained a gyroid sample with such an amazing long range order that up to 132 unique reflections were observed in a single SAXS pattern, and 152 reflections were observed overall. These scattering patterns provide the best evidence for gyroid morphology observed so far.

3.3   Experimental

3.3.1   Synthesis

A series of five A_2B_2 miktoarm stars was synthesized using methods similar to those reported by Iatrou and Hadjichristidis.[101] In the present work, however,

69

stoichiometric quantities of tetrachlorosilane were used, eliminating the need to remove excess silane. All manipulations were performed under high vacuum in all-glass, n-butyllithium-washed, benzene-rinsed reactors with breakseals for introduction of reactants and constriction seal-offs for sampling of intermediate products. Polystyryllithium and polyisoprenyllithium were separately prepared in benzene using sec-butyllithium initiator. In the linking reactor, tetrachlorosilane in benzene was chilled in an ice bath for ten minutes. Polystyryllithium was then added to the chlorosilane from a side flask at room temperature; more than one equivalent was added quickly with stirring and then the content was stirred at 0°C for twenty minutes. During this time the reduced vapor pressure in the reactor prevented transfer of the volatile silane to the side flask. The reactor was then warmed to room temperature and small incremental additions of polystyryllithium were made from the same side flask until essentially pure coupled product, as determined by size-exclusion chromatography (SEC) on sampled aliquots, was obtained. Steric effects and the slow addition of polystyryllithium prevented the formation of detectable amounts of three or four arm PS stars. Addition of more than twofold polyisoprenyllithium and subsequent fractionation yielded the A_2B_2 copolymer samples.

3.3.2 Molecular Characterization

The molecular characteristics of the arms and fractionated miktoarm stars are reported in Table 3.1. SEC was performed in tetrahydrofuran (THF) at 30°C using a Waters Model 510 pump, Waters Model 410 differential refractometer, and ultrastyragel columns with a continuous porosity range from 10^6 to 10^3 Å. For calculation of M_n values, calibration with absolute standards was performed.

70

Membrane osmometry (MO) using a Jupiter Model 231 recording membrane osmometer was conducted in toluene distilled from CaH_2. Low-angle light scattering (LALLS) was performed in THF distilled from sodium, using a Chromatix KMX-6 instrument operating at 633 nm. Matrix-assisted laser desorption/ionization time-of-flight mass spectroscopy (MALDI/TOF/MS) was performed in trans-retinoic acid with silver trifluoroacetate using a Perseptive Biosystems Voyager Elite DE instrument. Proton nuclear magnetic resonance (^{1}H-NMR) was carried out in $CDCl_3$ using a Bruker 300 MHz instrument. Ultraviolet spectroscopy (UV) was conducted in THF using a Waters Alliance 2690 separations module and Waters 996 photodiode array detector.

3.3.3 Morphological Characterization

The blends were produced by co-dissolving I_2S_2 block copolymer and homopolymer, in the appropriate proportions, in toluene, a non-preferential solvent. Solid film approximately 1mm thick was slowly cast at room temperature from these toluene solutions over a period of 4 weeks. Solvent evaporation was slowed by covering the samples with a crystallizing dish in order to promote the formation of well-ordered structures. After solidification of the samples, residual toluene was removed by placing the samples under vacuum at ambient temperature for another week. The samples were then annealed for one week under high vacuum at 150°C in order to further promote ordering. Finally, these blend samples were cooled under vacuum to room temperature over a period of several hours.

Sample morphologies were characterized using a combination of transmission electron microscopy (TEM) and small-angle X-ray scattering (SAXS). To prepare thin

71

sections for microscopy, a Leica Ultracut UCT microtome equipped with a Leica EM FCS cryogenic sample chamber operated at -110°C was used to cut sections approximately 500 Å in thickness. The sections were collected on TEM grids and stained for four hours in OsO_4 vapor. The PI microdomains are preferentially stained by OsO_4, rendering them dark relative to PS microdomains due to mass-thickness contrast in the TEM. A JEOL 100CX TEM, operated at an accelerating voltage of 100 kV, was used to image the stained sections. SAXS data were collected at the Advanced Polymers Beamline (X27C), located at the National Synchrotron Light Source at Brookhaven National Labs (BNL), Upton, NY. Two-dimensional scattering patterns were collected on Fujitsu image plates, then read by a Fujitsu BAS 2000 image plate reader. Custom software at BNL was used to subtract background noise and perform circular averaging. Data were collected for a wavelength of 1.307 Å and a camera length of 1410 mm.

Four different series of blends were prepared and their morphologies were examined. Blends are designated as either IXn-m or SXn-m. The first character, I or S, indicates that the homopolymer used in the blend series is homopolyisoprene (I) or homopolystyrene (S). The second character, X, indicates that the block copolymer used is an X shaped I_2S_2 *mikto*arm star block copolymer. The first number n indicates the PS volume fraction of the I_2S_2 graft copolymer on which the blend series is based. The last number, m, indicates the PS volume fraction of the overall blend after addition of homopolymer. The compositions of all the blends studied in this paper are given in Table2.

3.4   Results

SX14 series:

The pure I_2S_2-14, with polystyrene volume fraction Φ_{PS} =14%, forms hexagonally packed PS cylinders with reported *100* spacing of 27.7 ± 0.5 nm.[9] The SAXS data for the SX14 blend series are shown in Figure 3.3. The series of q_n/q^* ratios are the scattering vectors of all the Bragg peaks observed divided by the scattering vector of the primary reflection.   The q_n/q^* ratios of 1, $\sqrt{3}$, $\sqrt{4}$ and $\sqrt{7}$ indicate that SX14-20, SX14-25, SX14-29, SX14-34, and SX14-38 form cylindrical morphologies. The cylinder (100) spacing initially decreases from I_2S_2-14 to SX14-20; and then increases with increasing homopolymer concentration from SX14-20 to SX14-38. This behavior is similar to previous published results on linear block copolymer / homopolymer blends.[19]   The scattering vectors of the peaks occurring at integral multiples of q^* indicates that SX14-44 forms a lamellar morphology. TEM observation (data not shown) confirmed the morphologies observed in SAXS. Therefore, as the homopolymer concentration increases, the morphology of the blends changes from cylinder to lamella at an overall PS volume fraction between 0.38 and 0.44. No gyroid morphology was observed in this blend series. The morphologies of the SX14 series are mapped onto the morphology diagram in Figure 3.4.

SX28 series

The pure four-arm star I_2S_2-28, with polystyrene volume fraction Φ_{PS}=28%, forms hexagonally packed PS cylinders with a reported cylinder spacing of 31.9 ± 0.5

73

nm.[9] The SAXS data for the SX28 blend series are shown in Figure 3.5. The SAXS data indicate that the first blends sample, SX28-36, which has $q_n/q*$ ratio of 1, $\sqrt{3}$, $\sqrt{4}$, $\sqrt{7}$, $\sqrt{9}$, and $\sqrt{12}$, forms a cylindrical morphology. The next three blends, SX28-39, SX28-43, and SX28-46 form gyroid morphologies. For SX28-39 and SX28-43, $q_n/q* =$

$$1, \frac{\sqrt{8}}{\sqrt{6}}, \frac{\sqrt{14}}{\sqrt{6}}, \frac{\sqrt{20}}{\sqrt{6}}, \frac{\sqrt{24}}{\sqrt{6}}, \frac{\sqrt{26}}{\sqrt{6}}, \frac{\sqrt{32}}{\sqrt{6}}, \frac{\sqrt{38}}{\sqrt{6}}, \frac{\sqrt{42}}{\sqrt{6}}, \frac{\sqrt{50}}{\sqrt{6}}; \text{ for SX28-46, } q_n/q* = 1,$$

$$\frac{\sqrt{8}}{\sqrt{6}}, \frac{\sqrt{14}}{\sqrt{6}}, \frac{\sqrt{20}}{\sqrt{6}}, \frac{\sqrt{24}}{\sqrt{6}}, \frac{\sqrt{38}}{\sqrt{6}}, \frac{\sqrt{46}}{\sqrt{6}} \cdot \frac{\sqrt{52}}{\sqrt{6}},$$ The last blend in the series SX28-49,

which has integral $q_n/q*$ ratios, forms lamella. From I_2S_2-28 to SX28-36 in the cylinder morphology and from SX28-39 to SX28-47 in the gyroid morphology the domain spacing is found to increase with increasing homopolymer concentration. As shown in Figure 3.6, the TEM images confirm the morphologies observed in SAXS. In the SX28 blend series, the cylinder to gyroid morphology transition occurs at the PS overall volume fraction between 36% to 39%, and the gyroid to lamella morphology transition occurs at the PS overall volume fraction between 46% to 49%. The morphologies of the SX28 series are mapped onto the theoretical morphology diagram in Figure 3.7.

IX68 series

The pure four-arm star I_2S_2-68, with a polystyrene volume fraction $\Phi_{PS} = 68\%$, forms hexagonally packed PI cylinders with reported *100* spacing of 32.5 ± 0.5 nm.[9]. The SAXS data of this blend series are shown in Figure 3.8. The $q_n/q*$ ratios of 1, $\sqrt{3}$, $\sqrt{4}$, $\sqrt{7}$, $\sqrt{9}$, and $\sqrt{12}$ ... indicate that IX68-65 and IX68-61 form cylindrical

74

morphologies with PI in the cores of the cylinders. The q_n/q^* ratios of 1, $\frac{\sqrt{8}}{\sqrt{6}}$, $\frac{\sqrt{14}}{\sqrt{6}}$,

$\frac{\sqrt{20}}{\sqrt{6}}$, $\frac{\sqrt{24}}{\sqrt{6}}$, $\frac{\sqrt{32}}{\sqrt{6}}$, $\frac{\sqrt{40}}{\sqrt{6}}$ and $\frac{\sqrt{52}}{\sqrt{6}}$ indicate that IX68-58 forms a gyroid morphology;

and the integral q_n/q^* ratios indicate that IX68-53, IX68-49, IX68-41, and IX68-41

form lamellar morphologies. The morphologies observed in SAXS were confirmed by

TEM, images are shown in Figure 3.9. Interestingly, the last blend in this series, IX68-

37, forms a cylindrical morphology with PS in the cylinder cores, i.e. the inverse of the

pure I_2S_2-68. The observed morphologies in the IX68 series are mapped onto the

theoretical calculated morphology diagram in Figure 3.10. In these blends, the

transition from PI cylinders to lamella occurs at an overall PS volume fraction between

0.61 and 0.58. The transition from gyroid to lamella occurs at an overall PS volume

fraction between 0.58 and 0.53; and the transition from lamella to PS cylinders occurs

at an overall PS volume fraction between 0.41 and 0.37. Within the same morphology,

i.e. from pure I_2S_2-68 to IX68-61 and from IX68-53 to IX68-41, the domain spacing

increases with increasing homopolymer concentration

IX35 series

The pure four-arm star block copolymer I_2S_2-35, with polystyrene volume

fraction Φ_{PS} = 35%, forms a lamellar morphology with a reported lamella spacing of

36.3 ± 0.5 nm.[9] The SAXS data from the IX35 blend series are shown in Figure 3.11.

Blend sample IX35-33, which has integral q_n/q^* ratios, form lamellar morphology. The

75

q_n/q^* ratios of 1, $\dfrac{\sqrt{8}}{\sqrt{6}}$, $\dfrac{\sqrt{20}}{\sqrt{6}}$, $\dfrac{\sqrt{22}}{\sqrt{6}}$, $\dfrac{\sqrt{32}}{\sqrt{6}}$, $\dfrac{\sqrt{38}}{\sqrt{6}}$, $\dfrac{\sqrt{46}}{\sqrt{6}}$ $\dfrac{\sqrt{48}}{\sqrt{6}}$, $\dfrac{\sqrt{50}}{\sqrt{6}}$, $\dfrac{\sqrt{62}}{\sqrt{6}}$, $\dfrac{\sqrt{72}}{\sqrt{6}}$,

$\dfrac{\sqrt{86}}{\sqrt{6}}$ ... indicate that IX35-30 forms the gyroid morphology. The q_n/q^* ratios of 1, $\sqrt{3}$, $\sqrt{4}$, and $\sqrt{7}$ ... indicate that IX35-27, IX35-24, IX35-20, and IX35-17 all form cylindrical morphologies. In the IX35 blend series, the lamella to gyroid morphology transition occurs at an overall PS volume fraction between 33% and 30%. The gyroid to cylinder transition occurs at an overall PS volume fraction between 30% and 27%. The cylinder spacing increases with increasing homopolymer concentration from IX35-27 to IX35-17. IX35-31 formed an extremely well ordered *single crystal* like gyroid structure. A two-dimensional SAXS pattern of this *single crystal* is shown in Figure 3.12a. The X-ray beam is perpendicular to the surface of the 2 mm thick IX35-31 sample. Figure 3.12b gives the indexing of this pattern. From this single SAXS pattern, 132 unique reflections are observed. The relative intensities of these reflections are listed in Table 3. Combined with another SAXS pattern from a different zone, 160 total unique diffraction peaks were observed. The observed reflections are listed in Table 4 to compare with the permitted reflections for $Ia\bar{3}d$ symmetry. All the observed reflections are permitted for $Ia\bar{3}d$ symmetry; and most of the permitted reflections for $Ia\bar{3}d$ are observed. The near perfect long-range order of this sample is also supported by TEM observations. A TEM micrograph of IX35-31 is shown in Figure 3.13. Other blends in the IX35 series were also studied by TEM. The TEM observation (image not shown here) supports the morphologies observed though SAXS.

The morphologies of IX35 series are mapped onto the morphology diagram in Figure 3.14.

3.5   Discussion

In linear diblock copolymer / low molecular weight homopolymer blends the morphology transitions occur at roughly the same volume fraction regions as those of pure diblock copolymers.[17,18,20] The morphology transitions in the I_2S_2 block copolymer / homopolymer blends exhibit complex behaviors. The gyroid to lamella transition of linear diblock copolymers occurs at volume fraction of about 0.33 and 0.66. According to the morphology diagram, architecturally symmetric A_2B_2 should be morphologically similar to linear AB diblocks. Considering the conformational asymmetry between PS and PI in the I_2S_2 systems, the gyroid to lamella transitions for pure I_2S_2 block copolymers occurs at PS volume fractions around 0.28 and 0.63. In the IX35 blend series, based on the lamella forming I_2S_2-35, a transition to Gyroid and then to PS cylinders occurs over a volume fraction range (0.33-0.27) which is similar to that predicted for these transitions in pure I_2S_2. This behavior is similar to that of linear diblock copolymer / homopolymer blends. However, in the SX14 and SX28 series, the transitions from cylinder to lamella (SX14) and from gyroid to lamella (SX28) occur at PS volume fractions between 0.38 and 0.44 and between 0.46 and 0.49, respectively. These are strong shifts from the 28% predicted for pure I_2S_2 block copolymers. Thus there is a splitting of the cylinder-gyroid-lamellar transitions depending upon whether one is blending in PS homopolymer (SX14 and SX28 series) or PI homopolymer (IX35 series). Similar splitting was previously observed in blends of homopolymer with

77

asymmetric I_2S miktoarm star block copolymers where it was attributed to the effect of molecular asymmetry on the differing ability of homopolymer to penetrate the grafted brushes of block copolymer arms on the two arm vs. one arm side of the interface.[54] In the current study, splitting of OOTs is observed even though the I_2S_2 miktoarm stars have two arms per molecule on both sides of the interface. Due to the shifts in OOT volume fractions, morphologies can occurs at quite different volume fraction ranges as that of linear diblock systems. For example, the SX28-43, SX28-46, IX68-58 was observed to form gyroid morphologies at 43%, 46%, and 58% polystyrene volume fractions, which are well into the lamella region in linear diblock system; SX14-38 and IX68-61 from cylinder morphology at 38% and 61% PS volume fraction, which are also in the lamella region in linear diblock systems. This provides another parameter to tailor the morphologies block copolymer systems.

Inverted phases bring up by solvents was demonstrated by Sadron and Gallot for a cylindrical diblock copolymer and recently by Lodge and coworkers for a gyroid diblock copolymer.[103] However, morphology inversions that result from homopolymers have not been reported. Inside-out or inverted morphologies require the short block of the copolymer to swell to such an extent that its effective volume is larger than that of the unswollen long block of the copolymer. The swelling of the short block is promoted by the favorable entropy of mixing. In reported linear diblock copolymer / homopolymer blends, starting from cylinder forming diblock and blend homopolymer with the minority component, Winey, Thomas and Fetters[17] showed that as the homopolymer concentration increase, the cylinder morphology transform into lamella and then into macrophase separation. In that study, the homopolymer is PS, the

molecular weight of the hPS is 5.900 g/mol and the PS block molecular weights of the block copolymers are around 13,000 g/mol, which is about 2 times that MW of homopolymer. Blend sample IX68-37, which contains 44% homopolyisoprene and 56% I_2S_2-68, forms cylinder morphology with PS form the core of the cylinders, which is the inverse of pure I_2S_2-68. Even with 44% low MW homopolymer present in the matrix (PI), the PS cylinders still form good long-range order, as indicated by the SAXS data. The molecular weight of the hPI is 1,200 g/mol and the PI arm of I_2S_2-68 12,900 g/mol, which is about 10 times of the MW of homopolymer. These results indicates a greater solubility range for selective solvent molecules and for low molecular weight homopolymer than for higher MW homopolymers, and lower MW homopolymer maintains the long range order of the system.

IX35-30 and IX68-58 form extremely well ordered gyroid morphology. The single crystal SAXS pattern indicates the degree of ordering of this sample. Perfect single crystals are usually observed in atom and molecular level self-assemblies with each consisting of materials perfectly the same. In nano-scale self-assemblies, the repeat unit usually consists of hundreds to tens of thousands of atoms and the component molecules are not necessarily identical. Fluctuations and defects lead to imperfections and prevent the formation of large single crystal. All the cylinder or lamella blend samples are processed at the same conditions, but none of them have nearly the same degree of ordering as the Gyroid samples. This observation implies the defects structure in the interpenetration network of Gyroid have relatively higher energies or kinetically easier to eliminate than that of lamella and cylinder morphologies. These experimental results showed an example that the non-perfect

79

block copolymer systems can form near-perfect structures in a large area at certain compositions and process conditions.

3.6   Conclusions

Unlike linear diblock copolymer / homopolymer blend systems, shifts in OOT volume fraction is observed in the architecturally symmetry yet non-linear A_2B_2 block copolymer / homopolymer blends series. In IX68 blend series, morphology inversion is observed at high homopolymer concentration. "Gyroid Single crystal" was obtained though slow solvent casting and annealing. The SAXS of the sample provides the best evidence for gyroid morphology so far.

Table 3.1.   Molecular characterization of the I_2S_2 block copolymer and the PS and PI homopolymers.

[a] from SEC

[b] from membrane osmometry

[c] Data from reference.[9]

Sample Name	[a] M_n(PS arm) (g/mol)	[a] M_n(PI arm) (g/mol)	[b] M_n (total)	[a] M_w/M_n	[c] Vol% PS	[c] q^* (Å^{-1})	[c] Morphology
I_2S_2-14	9,080	41,000	106,000	1.01	14	0.0227	cylinder
I_2S_2-28	10,400	33,000	104,000	1.01	28	0.0197	cylinder
I_2S_2-35	20,500	30,800	99,000	1.03	35	0.0173	lamella
I_2S_2-68	37,300	12,900	104,000	1.01	68	0.0193	cylinder
hPS			1,050	1.13			
hPI			1,020	1.17			

Table 3.2.   Compositions and Morphologies of the blends in the study.

[a] Calculated utilizing density of PS =1.04 g/ml at 25°C and density of PI = 0.91 g/ml at 25°C.

[b] $q^* = 4\pi/\lambda(\sin\theta_1)$ and $2\theta_1$ is the scattering angle for the lowest angle Bragg peak; corresponds to $d_{(100)}$ for hexagonal packed cylinders, $d_{(001)}$ for lamellae, respectively.

Sample Name	Weight Fraction of Homopolymer	Overall Weight Fraction of PS	a Overall Volume Fraction of PS	Morphology	b $2\pi/q^*$ (±0.5nm)
SX14-20	0.07	0.22	0.20	Cylinder	25.5
SX14-25	0.13	0.27	0.25	Cylinder	27.9
SX14-29	0.18	0.32	0.29	Cylinder	28.3
SX14-34	0.25	0.37	0.34	Cylinder	28.7
SX14-38	0.30	0.41	0.38	Cylinder	30.4
SX14-44	0.37	0.47	0.44	Lamella	31.8
SX28-36	0.12	0.39	0.36	Cylinder	33.2
SX28-39	0.16	0.42	0.39	Gyroid	32.3
SX28-43	0.22	0.46	0.43	Gyroid	33.7
SX28-46	0.27	0.49	0.46	Gyroid	35.2
SX28-49	0.32	0.52	0.49	Lamella	35.0
IX68-65	0.05	0.68	0.65	Cylinder	33.8
IX68-61	0.10	0.64	0.61	Cylinder	33.9
IX68-58	0.14	0.61	0.58	Gyroid	32.4
IX68-53	0.21	0.56	0.53	Lamella	35.2
IX68-49	0.26	0.53	0.49	Lamella	36.0
IX68-45	0.32	0.49	0.45	Lamella	39.1
IX68-41	0.39	0.44	0.41	Lamella	40.3
IX68-37	0.44	0.40	0.37	Cylinder	36.0
IX35-33	0.07	0.36	0.33	Lamella	39.2
IX35-30	0.16	0.32	0.30	Gyroid	37.5
IX35-27	0.24	0.29	0.27	Cylinder	37.8
IX35-24	0.31	0.26	0.24	Cylinder	38.1
IX35-20	0.33	0.23	0.20	Cylinder	38.4
IX35-17	0.41	0.19	0.17	Cylinder	38.6

Table 3.3.   Observed reflections their intensities. (The intensity of the brightest peak was set as 1000)

Index	Intensity	Index	intensity	Index	Intensity	Index	Intensity
(2,2,0)	1000.0			(-4,-8,2)	106.0	(4,8,-2)	11.6
(4,4,0)	896.6			(3,-2,3)	280.9	(-3,2,-3)	18.7
(6,6,0)	505.1			(6,1,3)	31.5	(-6,-1,-3)	1.1
(-2,-2,0)	945.9			(8,2,2)	22.0	(-8,-2,-2)	7.1
(-4,-4,0)	904.9			(3,-3,2)	162.7	(-3,3,-2)	23.2
(-6,-6,0)	457.2			(2,-3,3)	190.7	(-2,3,-3)	18.3
(2,1,1)	112.5	(-2,-1,-1)	27.1	(-1,-6,3)	80.7	(1,6,-3)	6.8
(4.3.1)	30.3	(-4,-3,-1)	2.4	(-2,-8,2)	36.3	(2,8,-2)	14.1
(5,4,1)	113.8	(-5,-4,-1)	4.2	(5,-2,3)	432.6	(-5,2,-3)	46.9
(6,5,1)	35.1	(-6,-5,-1)	3.1	(6,-1,3)	279.1	(-6,1,-3)	36.4
(7,6,1)	56.7	(-7,-6,-1)	5.5	(8,1,3)	28.3	(-8,-1,-3)	4.8
(-1,-2,1)	315.0	(1,2,-1)	33.9	(2,-5,3)	370.0	(-2,5,-3)	45.9
(-3,-4,1)	145.1	(3,4,-1)	8.9	(1,-6,3)	218.5	(-1,6,-3)	25.9
(-4,-5,1)	238.4	(4,5,-1)	9.6	(-1,-8,3)	10.1	(1,8,-3)	2.0
(-5,-6,1)	74.1	(5,6,-1)	4.3	(4,-4,4)	1052.1	(-4,4,-4)	100.7
(-6,-7,1)	68.6	(6,7,-1)	1.7	(5,-3,4)	667.2	(-5,3,-4)	63.8
(2,-1,1)	242.2	(-2,1,-1)	42.1	(6,-2,4)	70.0	(-6,2,-4)	5.5
(5,2,1)	223.7	(-5,-2,-1)	23.9	(8,0,4)	285.2	(-8,0,-4)	24.3
(6,3,1)	121.4	(-6,-3,-1)	19.6	(3,-5,4)	644.5	(-3,5,-4)	55.9
(7,4,1)	8.4	(-7,-4,-1)	1.1	(2,-6,4)	63.7	(-2,6,-4)	7.3
(8,5,1)	32.1	(-8,-5,-1)	8.4	(0,-8,4)	209.9	(0,8,-4)	19.8
(1,-2,1)	227.7	(-1,2,-1)	45.2	(7,-3,4)	49.7	(-7,3,-4)	3.2
(-2,-5,1)	191.1	(2,5,-1)	29.5	(8,-2,4)	90.4	(-8,2,-4)	12.5
(-3,-6,1)	141.7	(3,6,-1)	17.4	(3,-7,4)	100.1	(-3,7,-4)	10.8
(-4,-7,1)	29.7	(4,7,-1)	4.9	(2,-8,4)	90.2	(-2,8,-4)	14.6
(-5,-8,1)	64.9	(5,8,-1)	9.5	(6,-5,5)	544.9	(-6,5,-5)	53.0
(3,-1,2)	17.7	(-3,1,-2)	1.1	(7,-4,5)	257.1	(-7,4,-5)	28.2
(4,0,2)	883.5	(-4,0,-2)	4.9	(5,-6,5)	527.7	(-5,6,-5)	44.4
(5,1,2)	392.0	(-5,-1,-2)	43.3	(4,-7,5)	188.2	(-4,7,-5)	22.2
(7,3,2)	200.3	(-7,-3,-2)	9.8	(8,-6,6)	13.5	(-8,6,-6)	11.2
(8,4,2)	135.8	(-8,-4,-2)	11.4	(7,-7,6)	92.3	(-7,7,-6)	7.6
(1,-3,2)	29.2	(-1,3,-2)	2.5	(6,-8,6)	62.0	(-6,8,-6)	5.7
(0,-4,2)	927.8	(0,4,-2)	86.9	(9,-8,7)	78.4	(-9,8,-7)	4.9
(-1,-5,2)	366.7	(1,5,-2)	38.3	(8,-9,7)	63.8	(-8,9,-7)	3.5
(-3,-7,2)	140.6	(3,7,-2)	10.3				

Table 3.4. The permitted reflections of $Ia\bar{3}d$ and observed reflections for IX35-30.

Listed h, k, l, are permitted reflection for Cubic Aspects. + indicates presence of reflection. – indicates absence of reflection. $s=h^2+k^2+l^2$. Reflections with $s\leq100$ are listed. Table from reference[104].

s	h	k	l	$Ia\bar{3}d$	observed	s	h	k	l	$Ia\bar{3}d$	observed
1	1	0	0	-	-	30	5	2	1	+	+
2	1	1	0	-	-	32	4	4	0	+	+
3	1	1	1	-	-	33	5	2	2	-	-
4	2	0	0	-	-	33	4	4	1	-	-
5	2	1	0	-	-	34	5	3	0	-	-
6	2	1	1	+	+	34	4	3	3	-	-
8	2	2	0	+	+	35	5	3	1	-	-
9	3	0	0	-	-	36	6	0	0	-	-
9	2	2	1	-	-	36	4	4	2	-	-
10	3	1	0	-	-	37	6	1	0	-	-
11	3	1	1	-	-	38	6	1	1	+	+
12	2	2	2	-	-	38	5	3	2	+	+
13	3	2	0	-	-	40	6	2	0	+	+
14	3	2	1	+	+	41	6	2	1	-	-
16	4	0	0	+	-	41	5	4	0	-	-
17	4	1	0	-	-	41	4	4	3	-	-
17	3	2	2	-	-	42	5	4	1	+	+
18	4	1	1	-	-	43	5	3	3	-	-
18	3	3	0	-	-	44	6	2	2	-	-
19	3	3	1	-	-	45	6	3	0	-	-
20	4	2	0	+	+	45	5	4	2	-	-
21	4	2	1	-	-	46	6	3	1	+	+
22	3	3	2	+	+	48	4	4	4	+	+
24	4	2	2	+	+	49	7	0	0	-	-
25	5	0	0	-	-	49	6	3	2	-	-
25	4	3	0	-	-	50	7	1	0	-	-
26	5	1	0	-	-	50	5	5	0	-	-
26	4	3	1	+	+	50	5	4	3	+	+
27	5	1	1	-	-	51	7	1	1	-	-
27	3	3	3	-	-	51	5	5	1	-	-
29	5	2	0	-	-	52	6	4	0	+	+
29	4	3	2	-	-	53	7	2	0	-	-

s	h	k	l	$Ia\bar{3}d$	observed	s	h	k	l	$Ia\bar{3}d$	observed
53	6	4	1	-	-	78	7	5	2	+	-
54	7	2	1	+	-	80	8	4	0	+	+
54	6	3	3	+	+	81	9	0	0	-	-
54	5	5	2	+	-	81	8	4	1	-	-
56	6	4	2	+	+	81	7	4	4	-	-
57	7	2	2	-	-	81	6	6	3	-	-
57	5	4	4	-	-	82	9	1	0	-	-
58	7	3	0	-	-	82	8	3	3	-	-
59	7	3	1	-	-	83	9	1	1	-	-
59	5	5	3	-	-	83	7	5	3	-	-
61	6	5	0	-	-	84	8	4	2	+	+
61	6	4	3	-	-	85	9	2	0	-	-
62	7	3	2	+	+	85	7	6	0	-	-
62	6	5	1	+	+	86	9	2	1	+	-
64	8	0	0	+	-	86	7	6	1	+	-
65	8	1	0	-	-	86	6	5	5	+	+
65	7	4	0	-	-	88	6	6	4	+	+
65	6	5	2	-	-	89	9	2	2	-	-
66	8	1	1	-	-	89	8	5	0	-	-
66	7	4	1	+	-	89	8	4	3	-	-
66	5	5	4	-	-	89	7	6	2	-	-
67	7	3	3	-	-	90	9	3	0	-	-
68	8	2	0	+	+	90	8	5	1	+	+
68	6	4	4	-	-	90	7	5	4	+	+
69	8	2	1	-	-	91	9	3	1	-	-
69	7	4	2	-	-	93	8	5	2	-	-
70	6	5	3	+	+	94	9	3	2	+	+
72	8	2	2	+	+	94	7	6	3	+	-
72	6	6	0	+	+	96	8	4	4	+	-
73	8	3	0	-	-	97	9	4	0	-	-
73	6	6	1	-	-	97	6	6	5	-	-
74	8	3	1	+	-	98	9	4	1	+	+
74	7	5	0	-	-	98	8	5	3	+	+
74	7	4	3	+	+	98	7	7	0	-	-
75	7	5	1	-	-	99	9	3	3	-	-
75	5	5	5	-	-	99	7	7	1	-	-
76	6	6	2	-	-	99	7	5	5	-	-
77	8	3	2	-	-	100	10	0	0	-	-
77	6	5	4	-	-	100	8	6	0	+	+
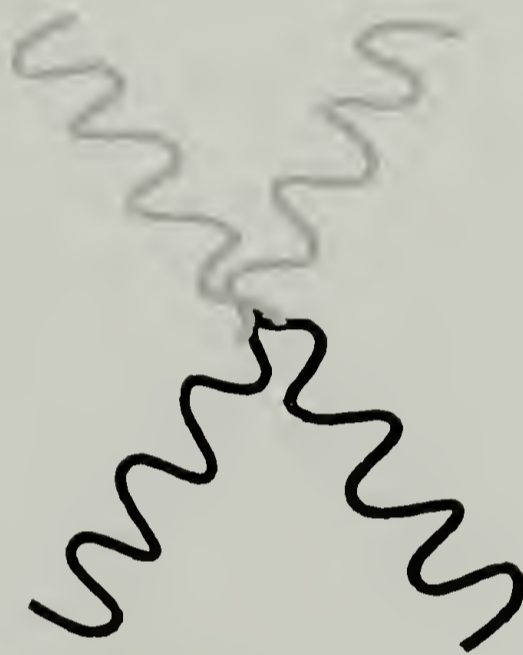
Figure 3.1.   Illustrations of A_2B_2 miktoarm star block copolymer architecture.
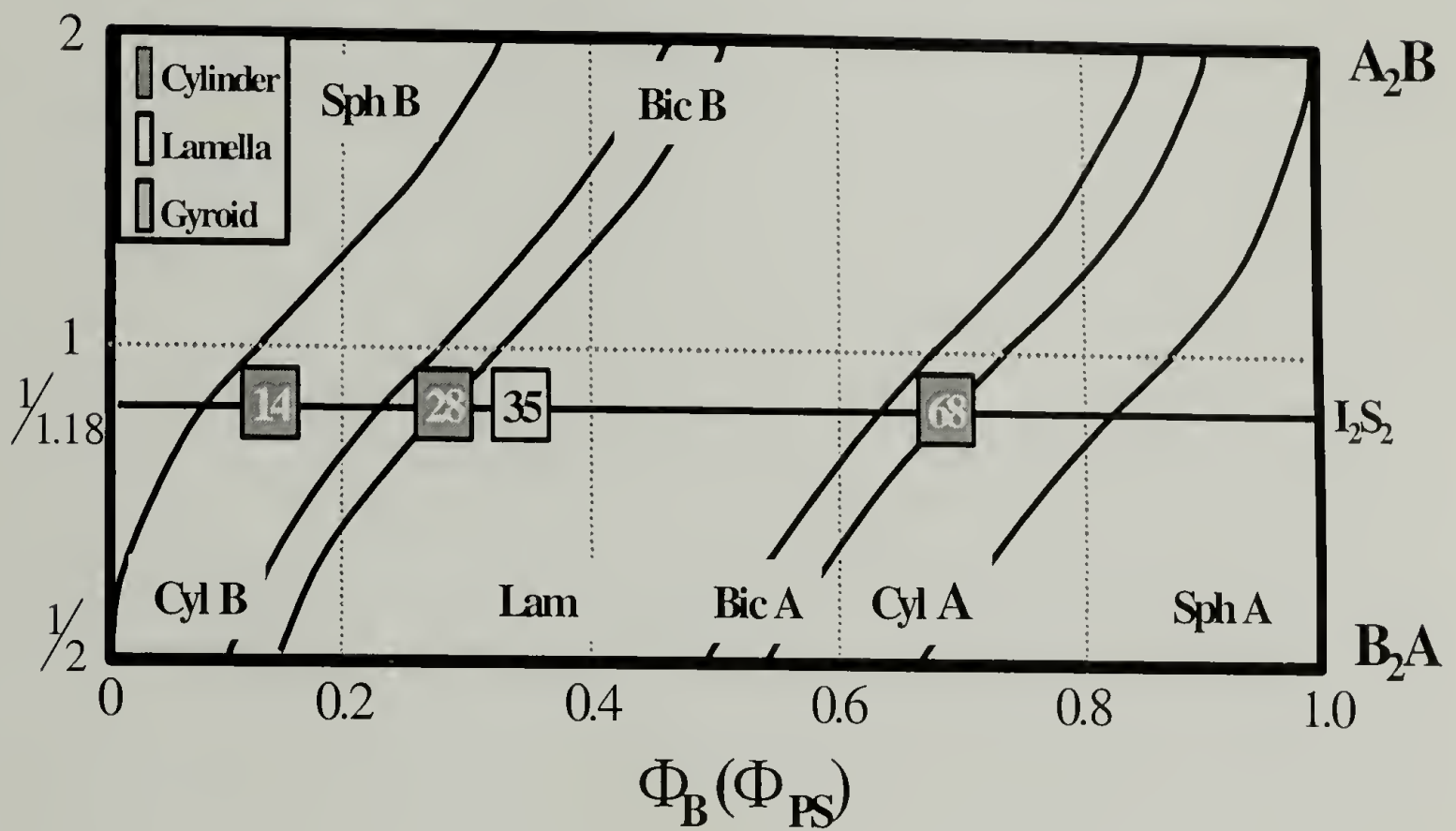
Figure 3.2.   Morphology diagram with A_2B_2 block copolymer sample positions indicated. The numbers in the symbols correspond to the sample numbers given in Table 3.1.

Figure 3.3.   Log(I) vs. q SAXS patterns for the SX14 blend series. The ratios q_n/q^* of the scattering vector of each peak to the scattering vector of the primary peak are indicated.
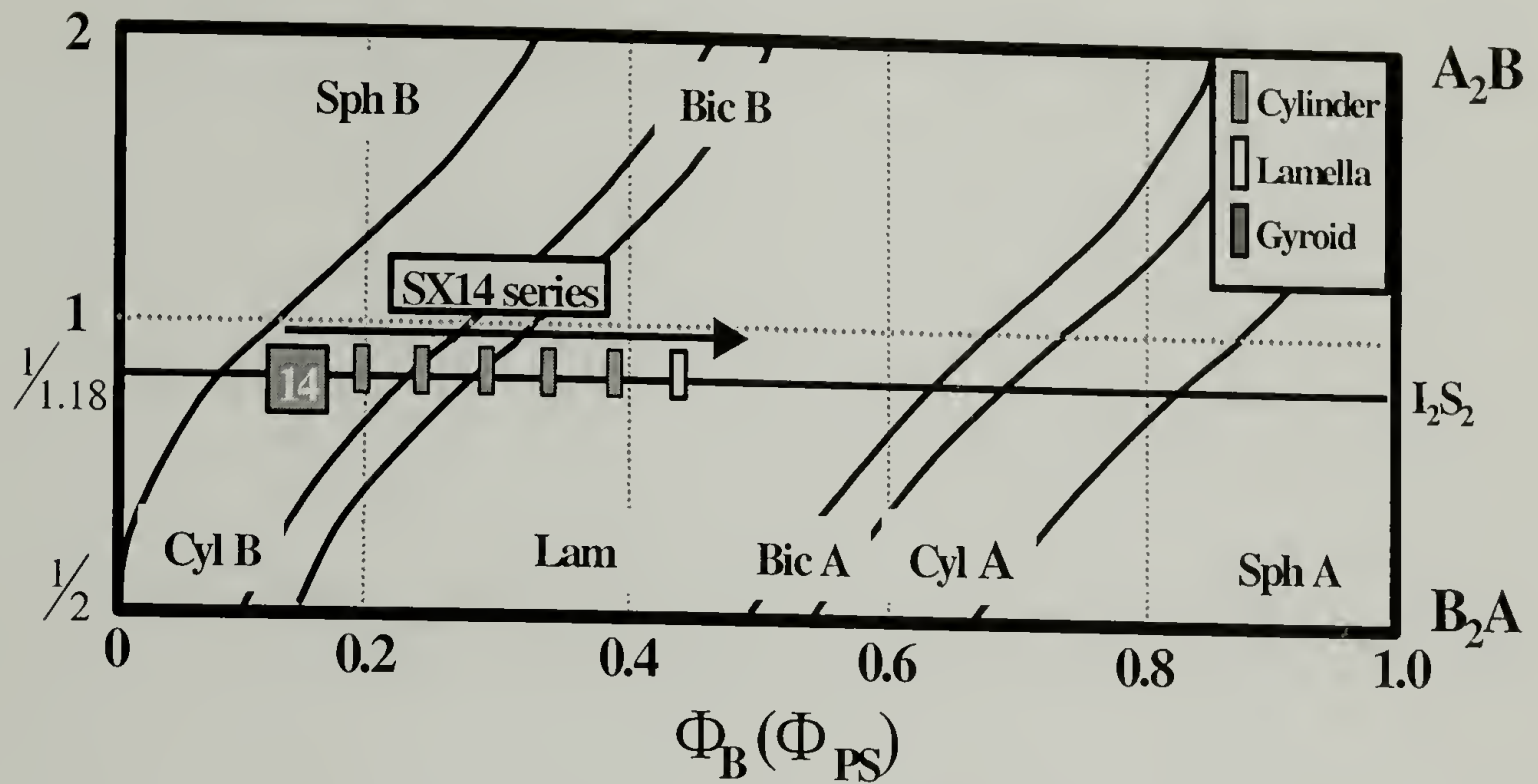
Figure 3.4. Blend series SX14 mapped onto the theoretical morphology diagram. The numbered symbols along the solid line at $\varepsilon = 1/1.18$ indicate the volume fractions of the pure I_2S_2 samples upon which the blends are based. The locations on the diagrams of small rectangular boxes indicate the volume fractions of the blends in the series. The shading of the boxes indicates the morphology.

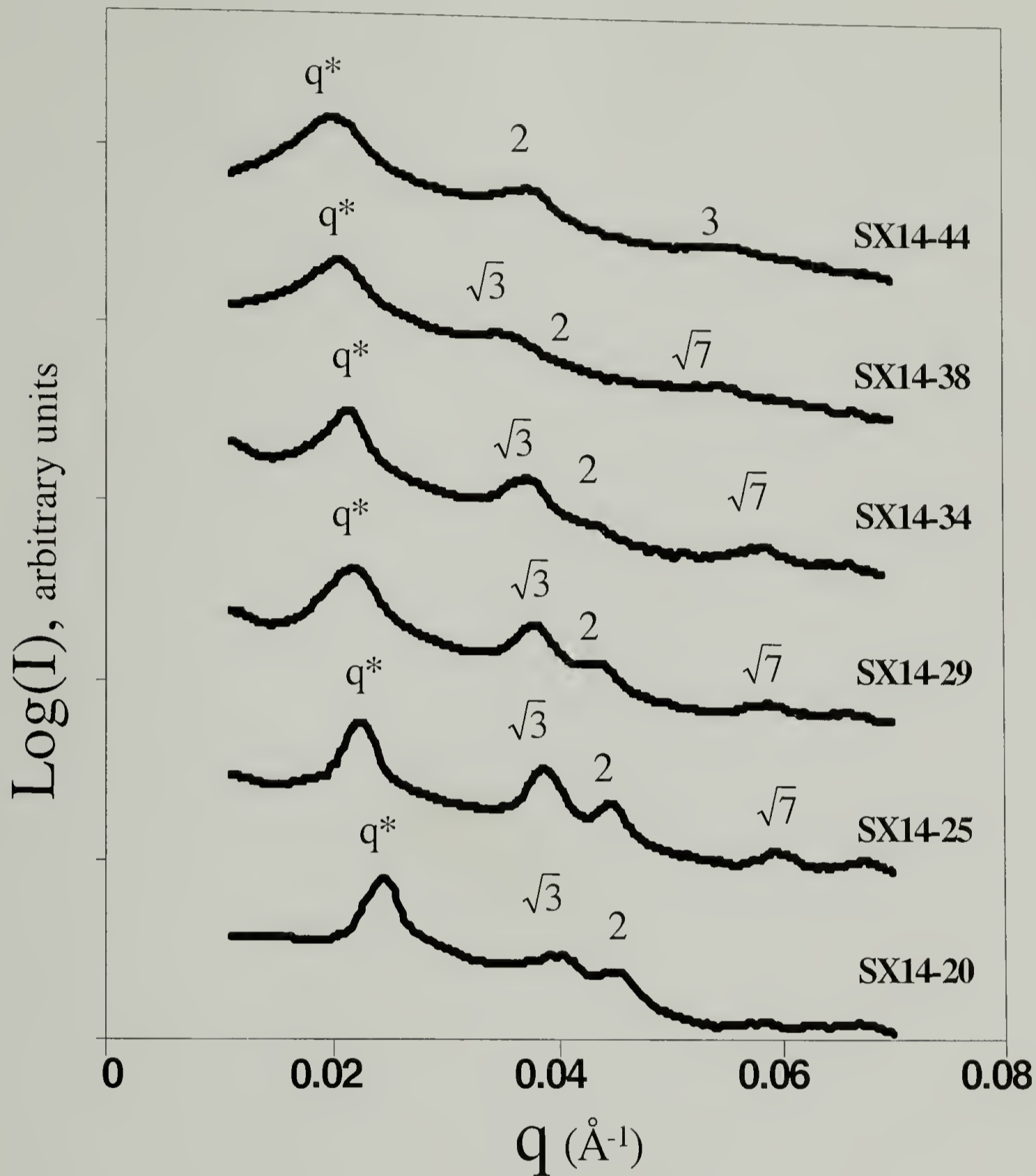Figure 3.5.   Log(I) vs. q SAXS patterns for the SX14 blend series. The ratios q_n/q^* of the scattering vector of each peak to the scattering vector of the primary peak are indicated.

a

500 nm

b

500 nm
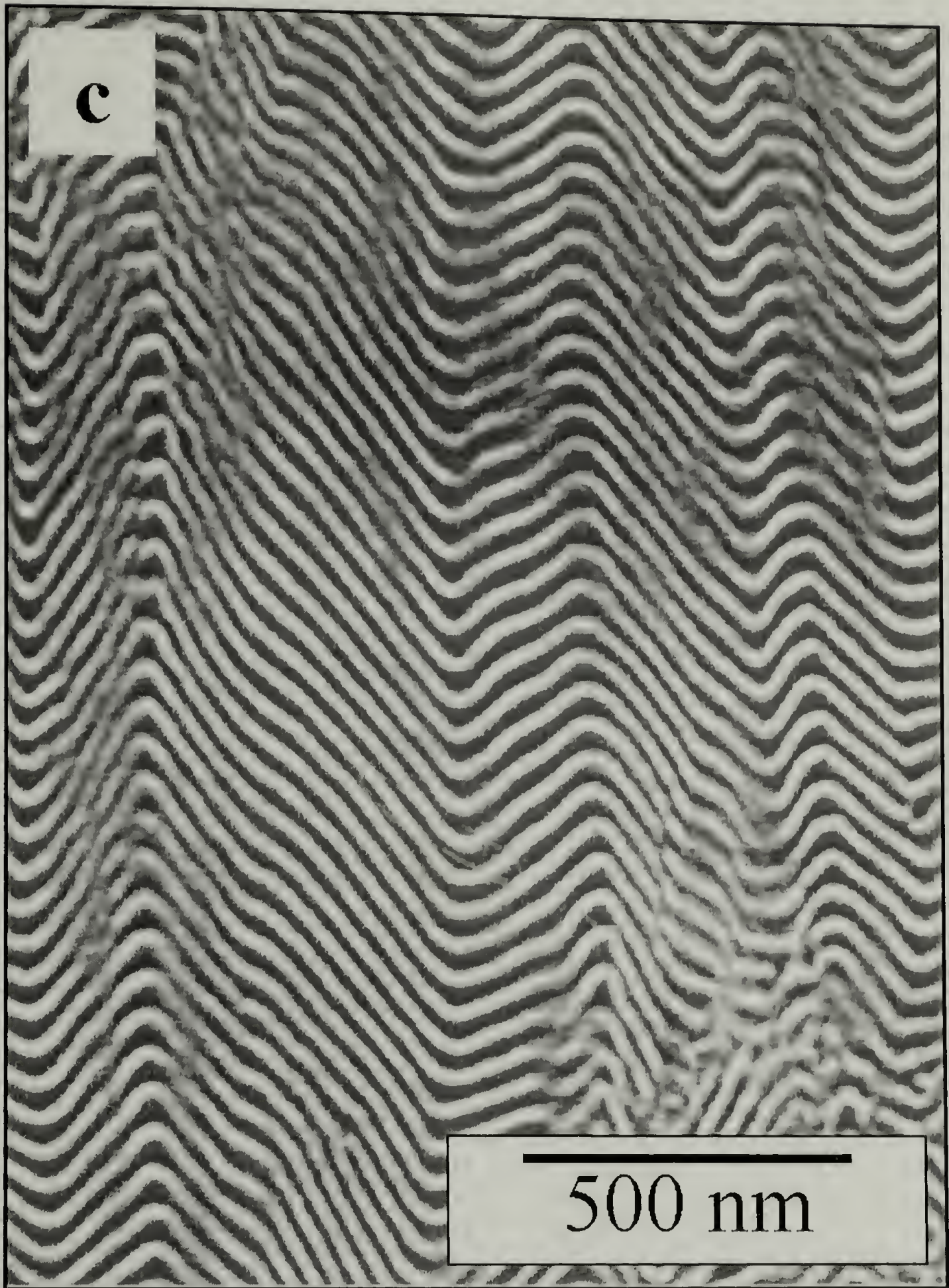
Figure 3.6.   TEM of blend series SX28. a) SX28-36; b) SX28-46; c) SX28-49.
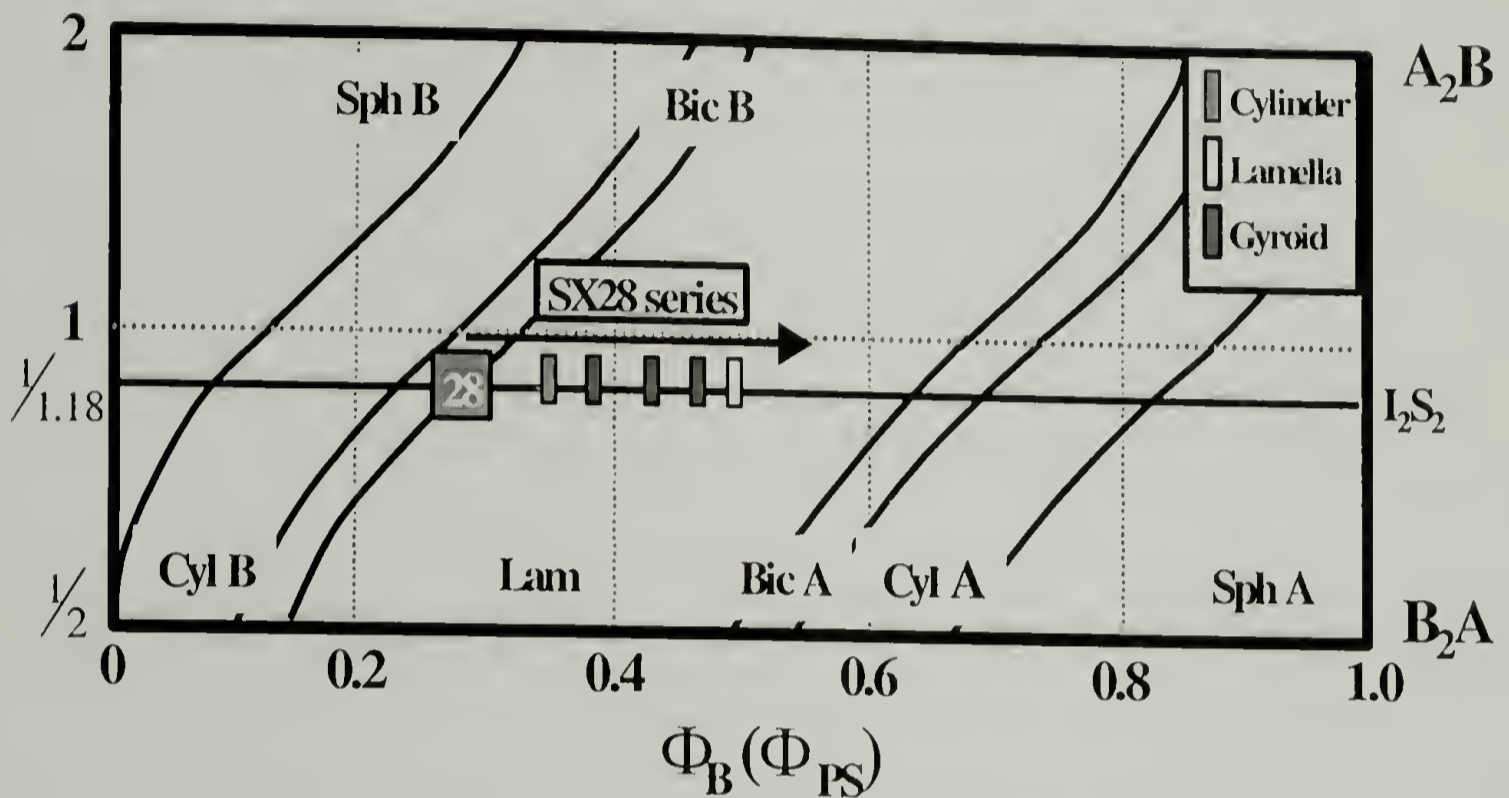
Figure 3.7.   Blend series SX28 mapped onto the theoretical morphology diagram. The numbered symbols along the solid line at $\varepsilon = 1/1.18$ indicate the volume fractions of the pure I_2S_2 samples upon which the blends are based.   The locations on the diagrams of small rectangular boxes indicate the volume fractions of the blends in the series.   The shading of the boxes indicates the morphology.
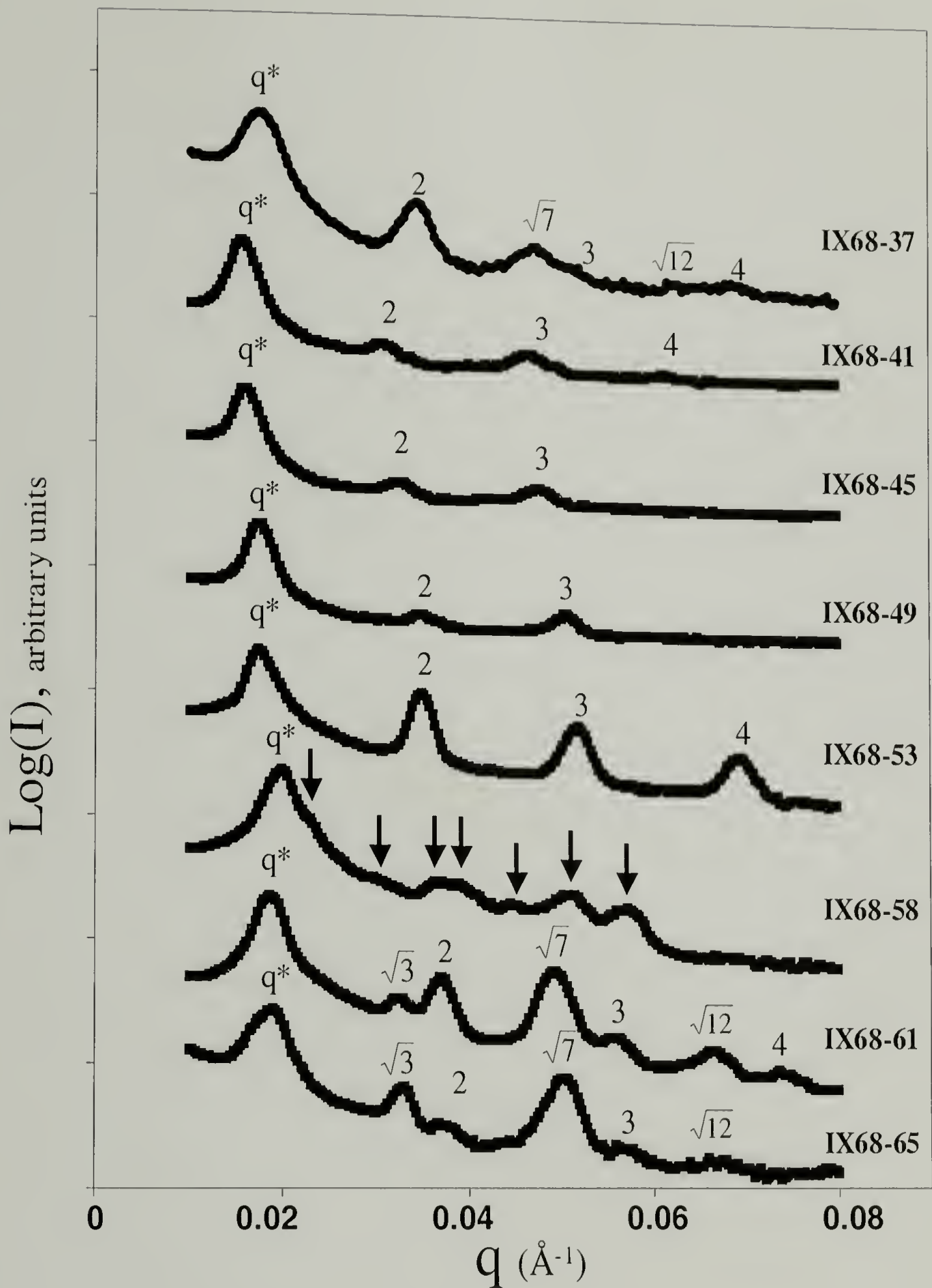
Figure 3.8. Log(I) vs. q SAXS patterns for the IX68 blend series. The ratios q_n/q^* of the scattering vector of each peak to the scattering vector of the primary peak are indicated.

95

500 nm

500 nm

97

c
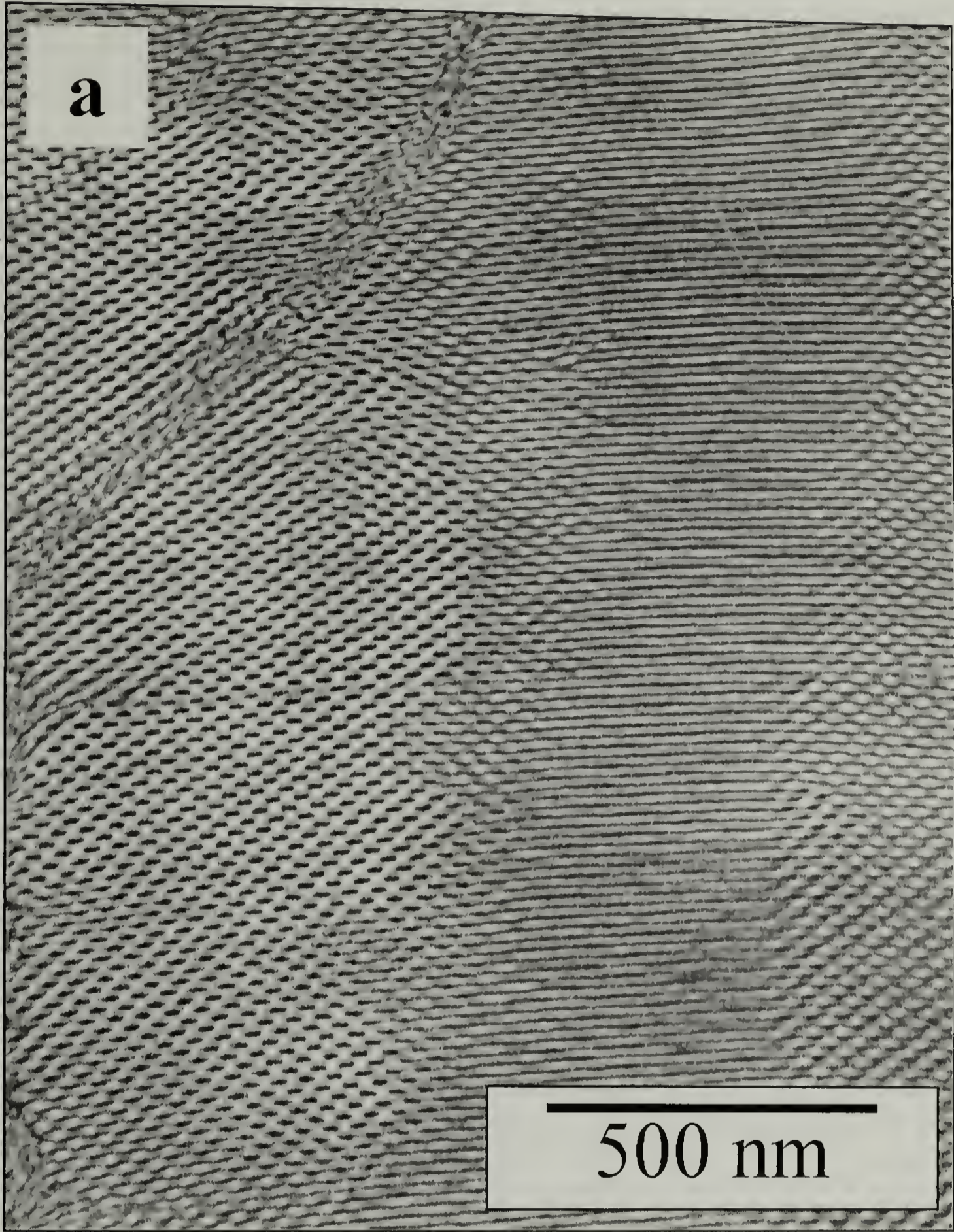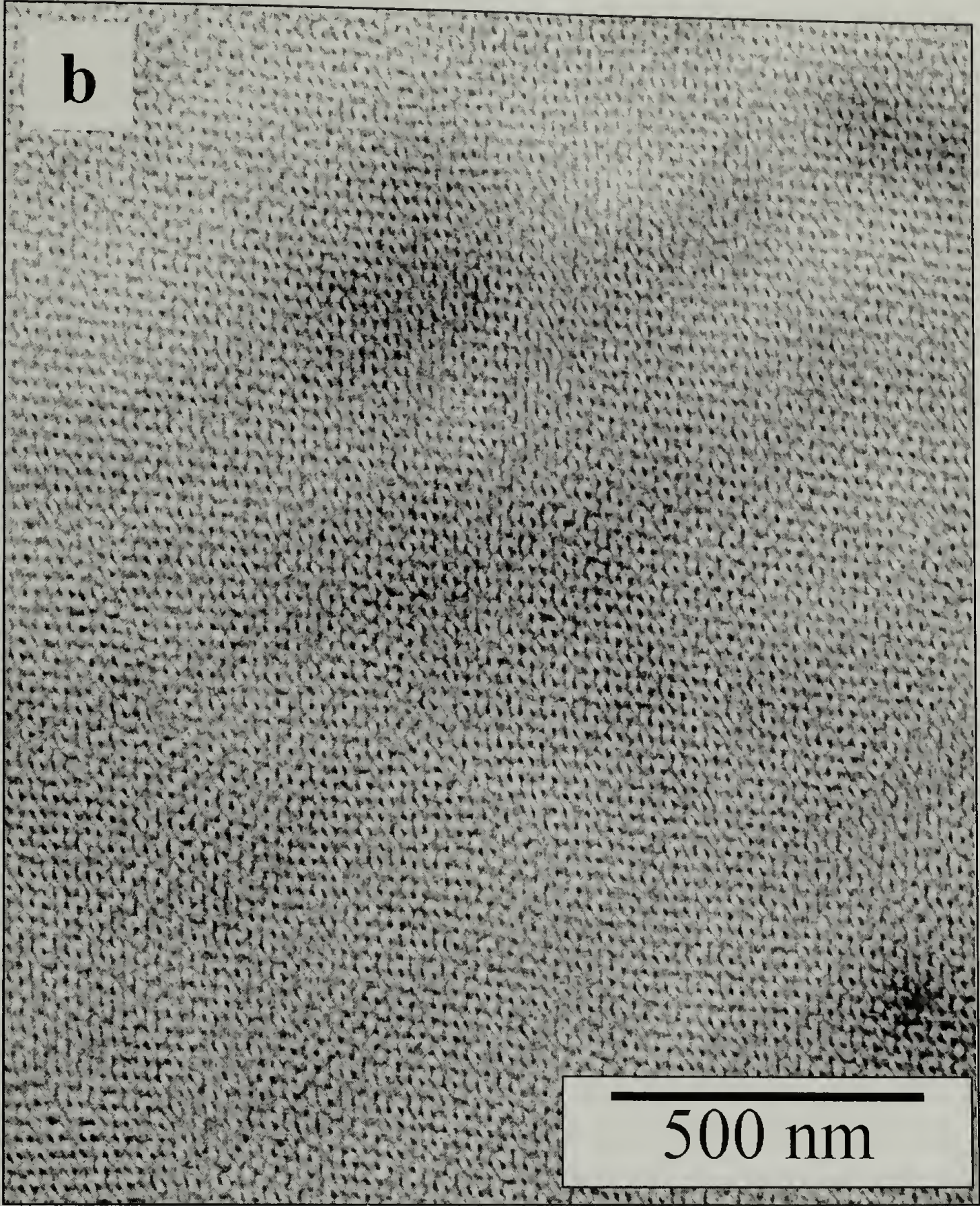
500 nm
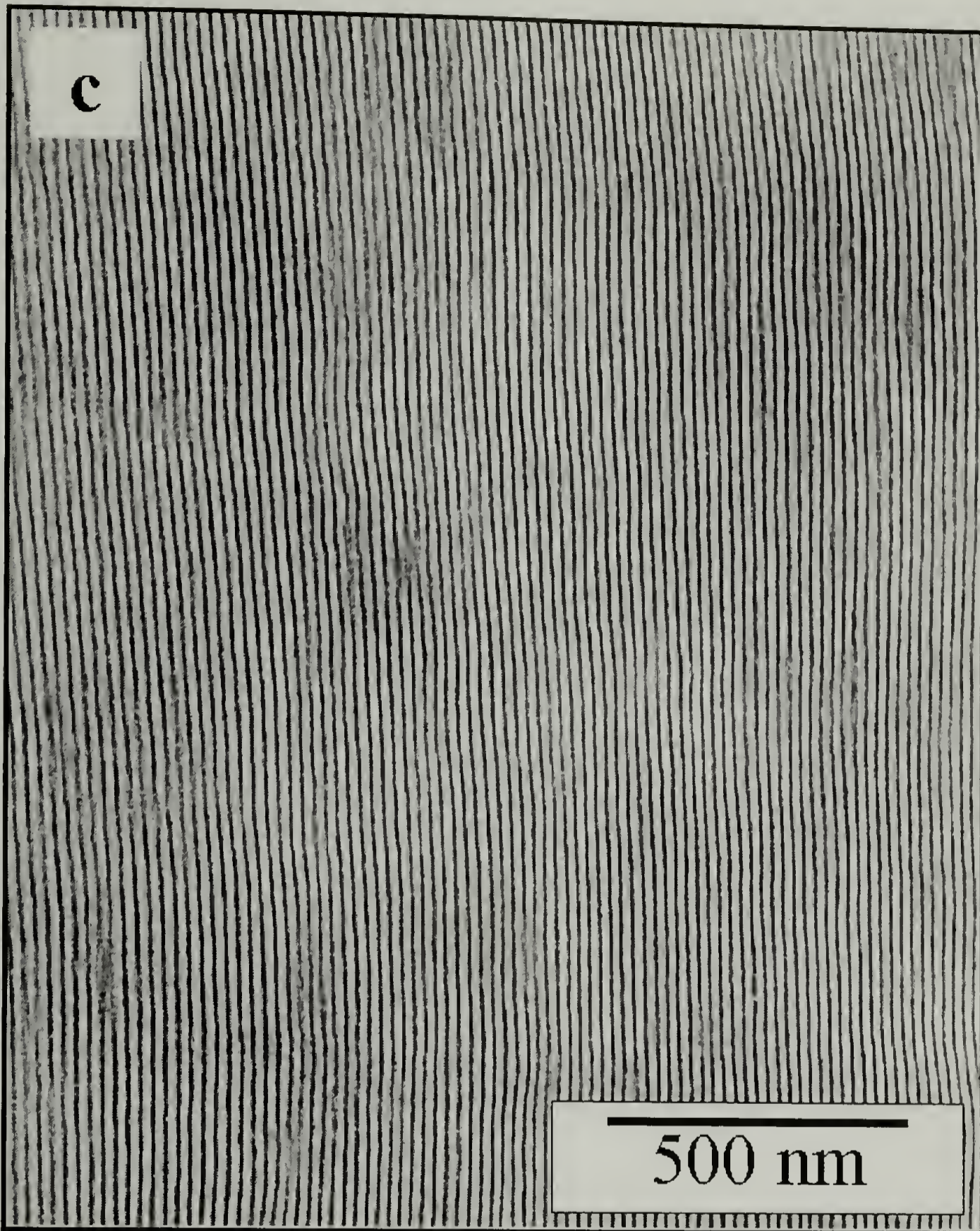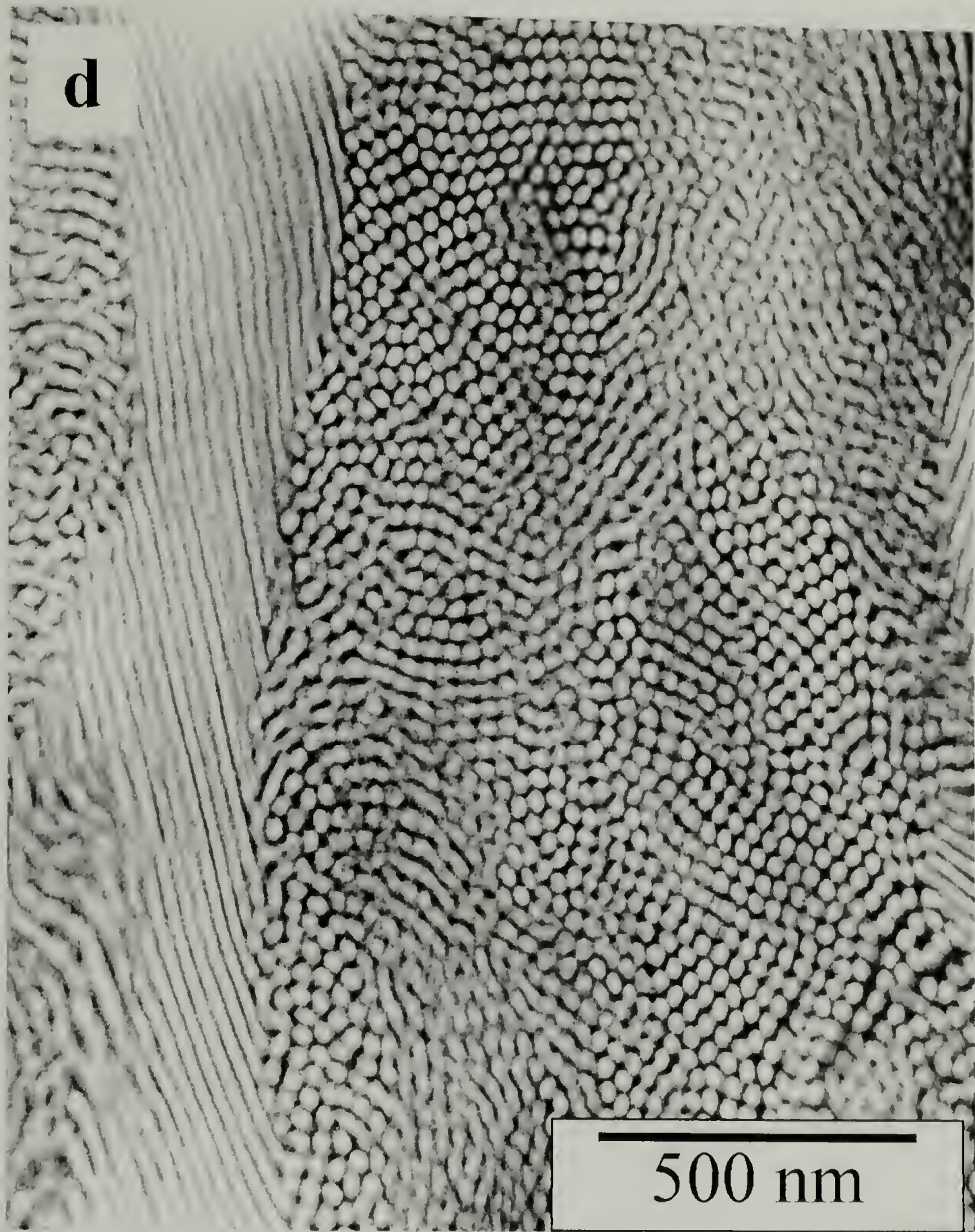
Figure 3.9.   TEM of IX68 blend series.   a) IX68-65; b) IX68-58; c) IX68-45; d) IX68-37.
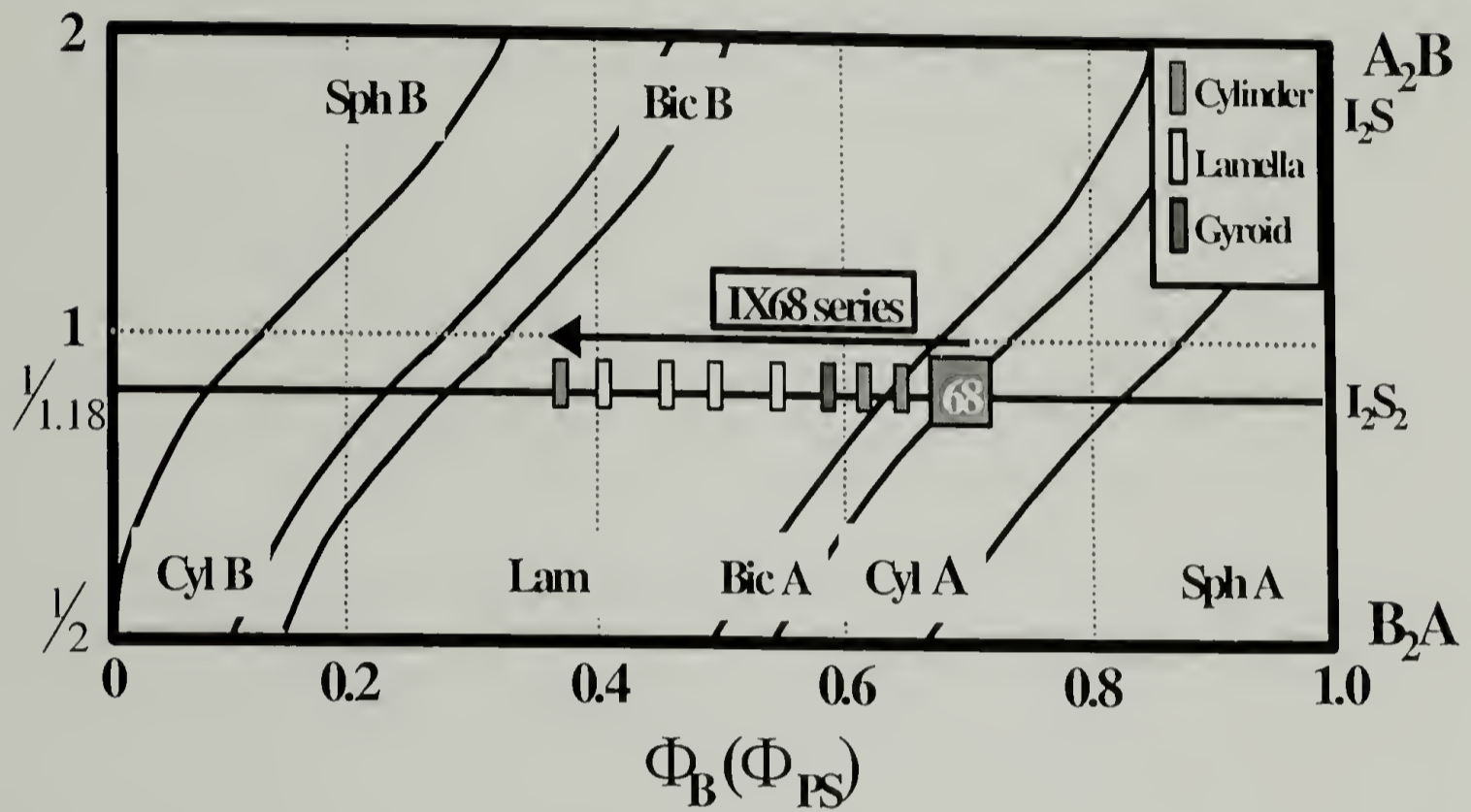
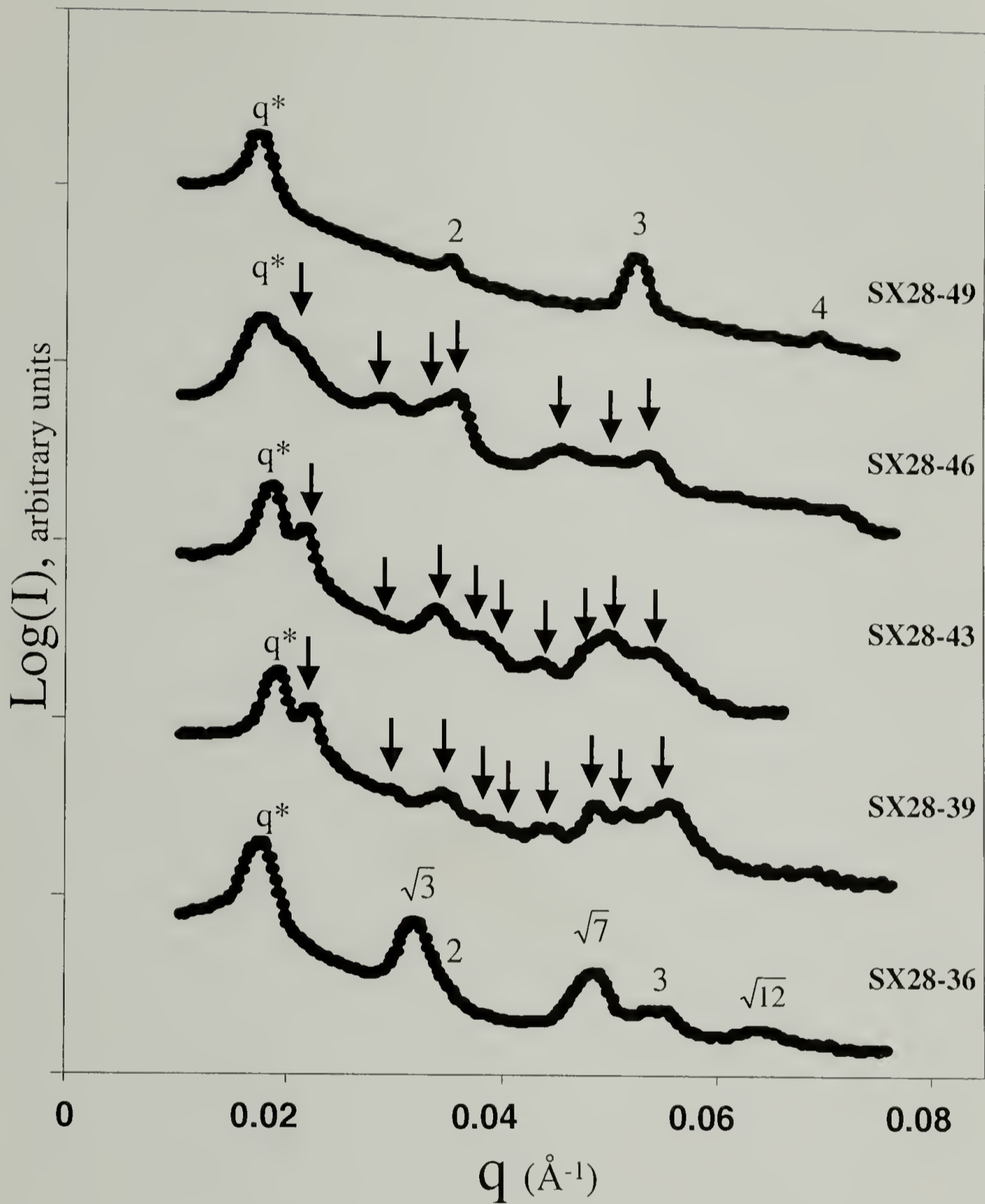Figure 3.10.   Blend series IX68 mapped onto the theoretical morphology diagram.
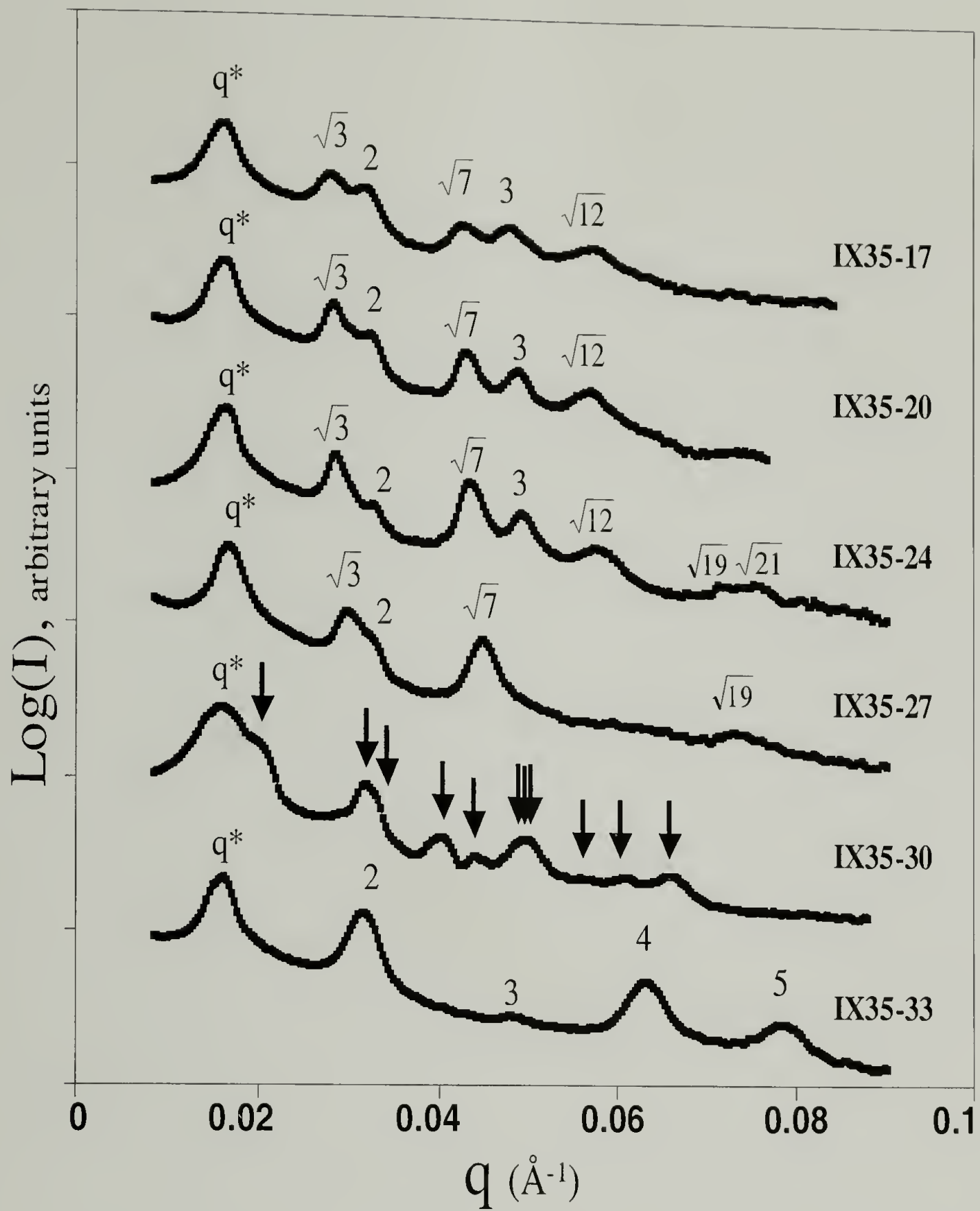
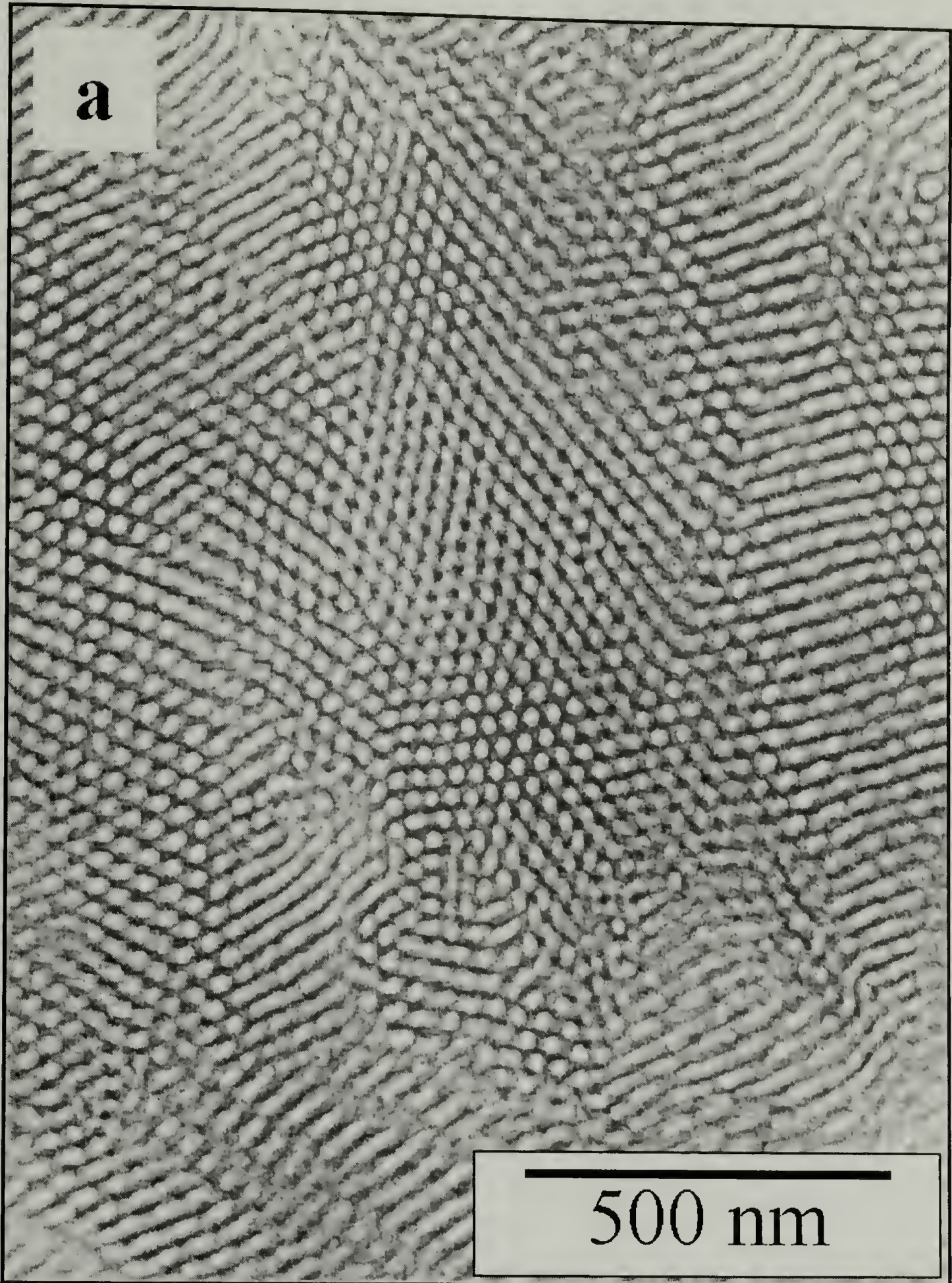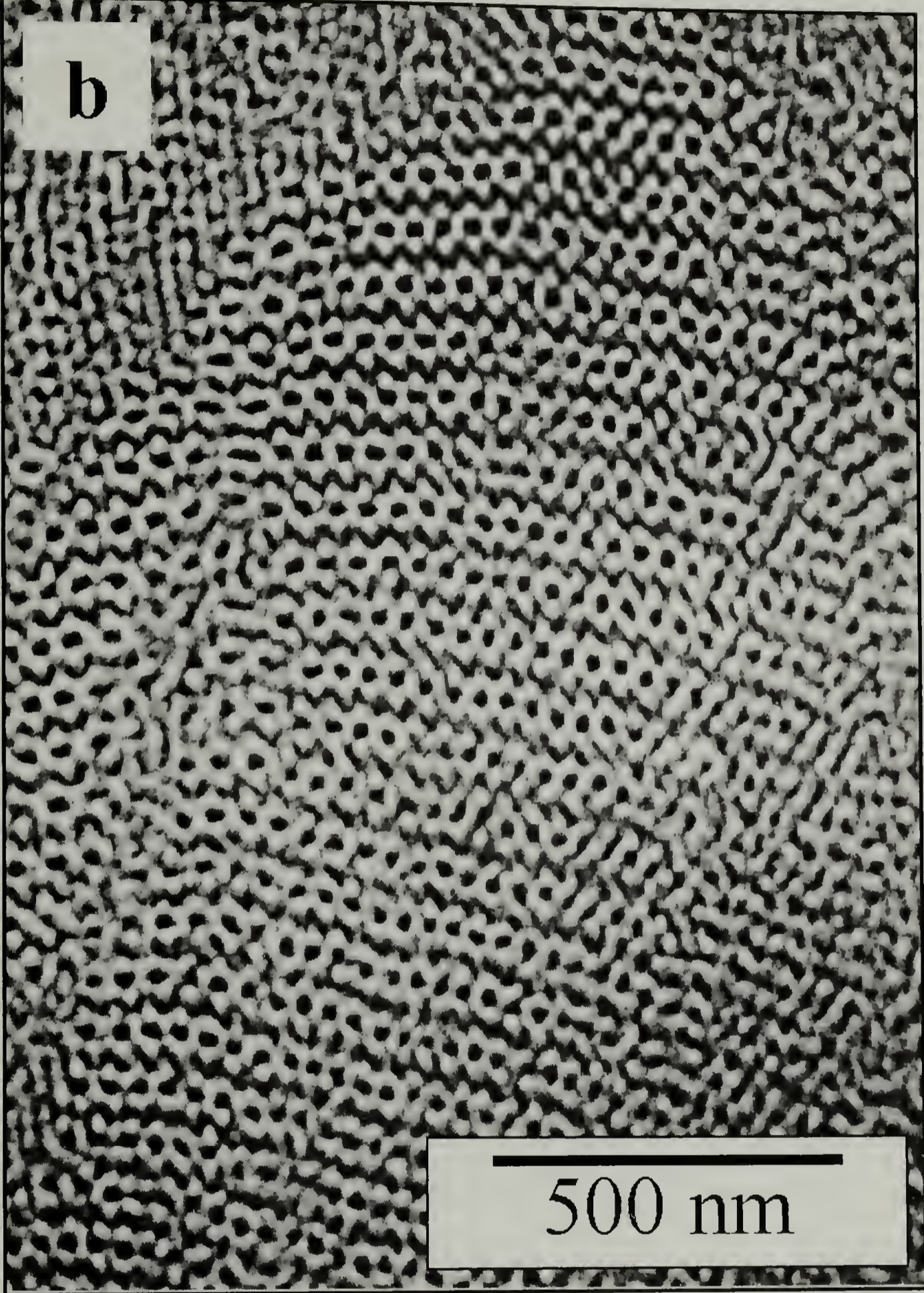Figure 3.11. Log(I) vs. q SAXS patterns for the IX68 blend series. The ratios q_n/q^* of the scattering vector of each peak to the scattering vector of the primary peak are indicated.

a
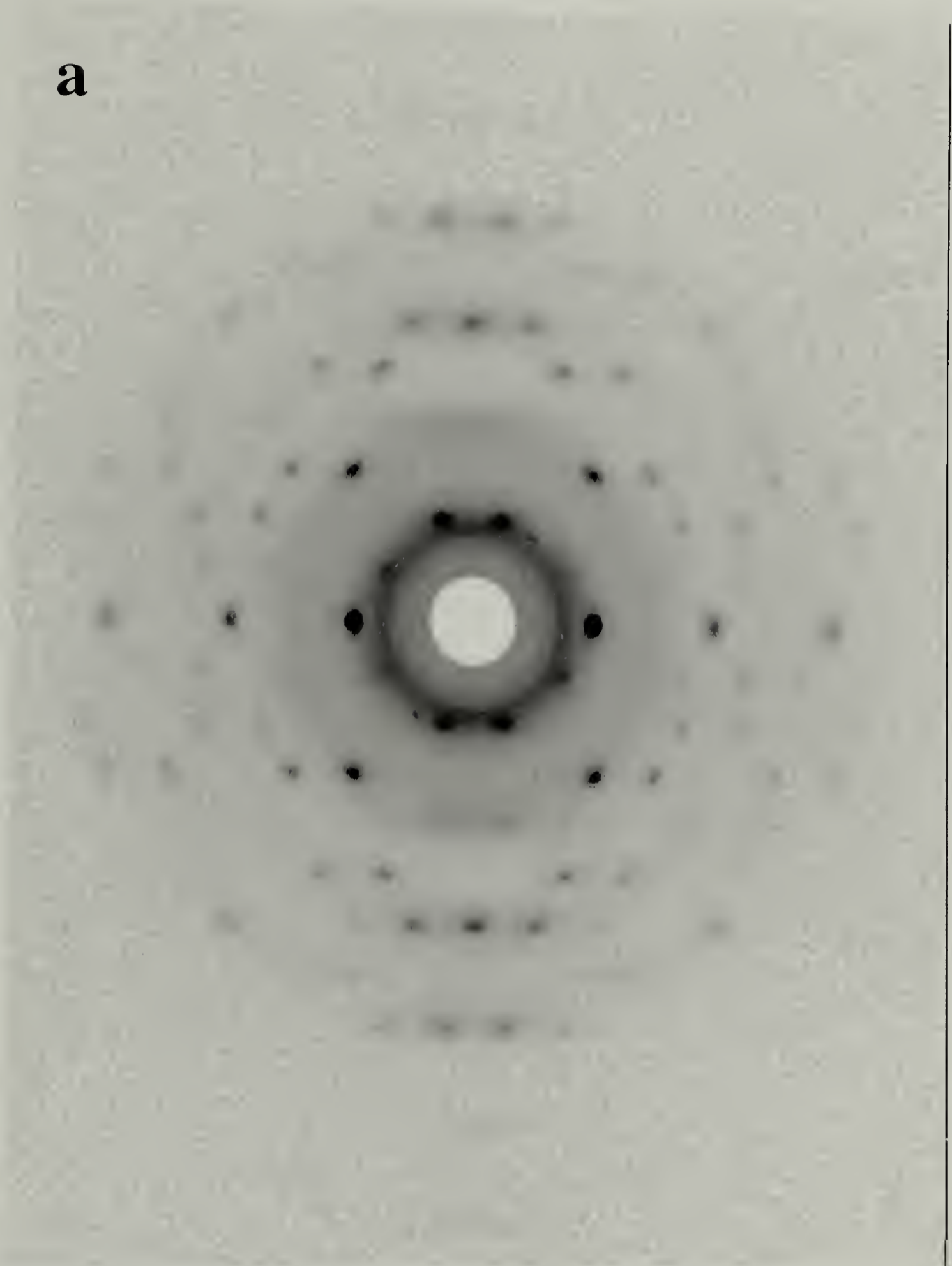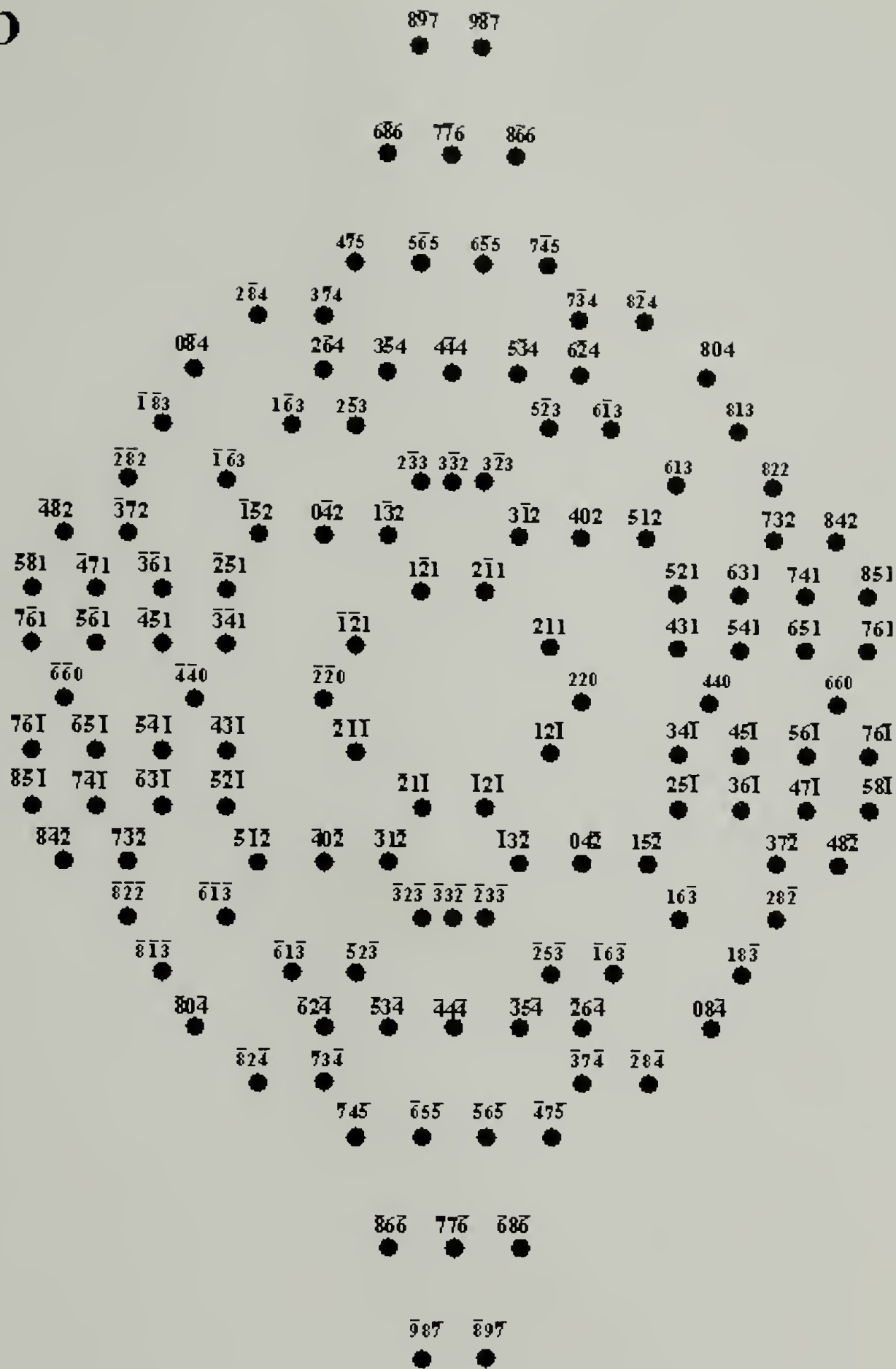
Figure 3.12. Two dimensional single crystal SAXS pattern of IX35-30 gyroid structure (a) pattern (b) indexed schematic.
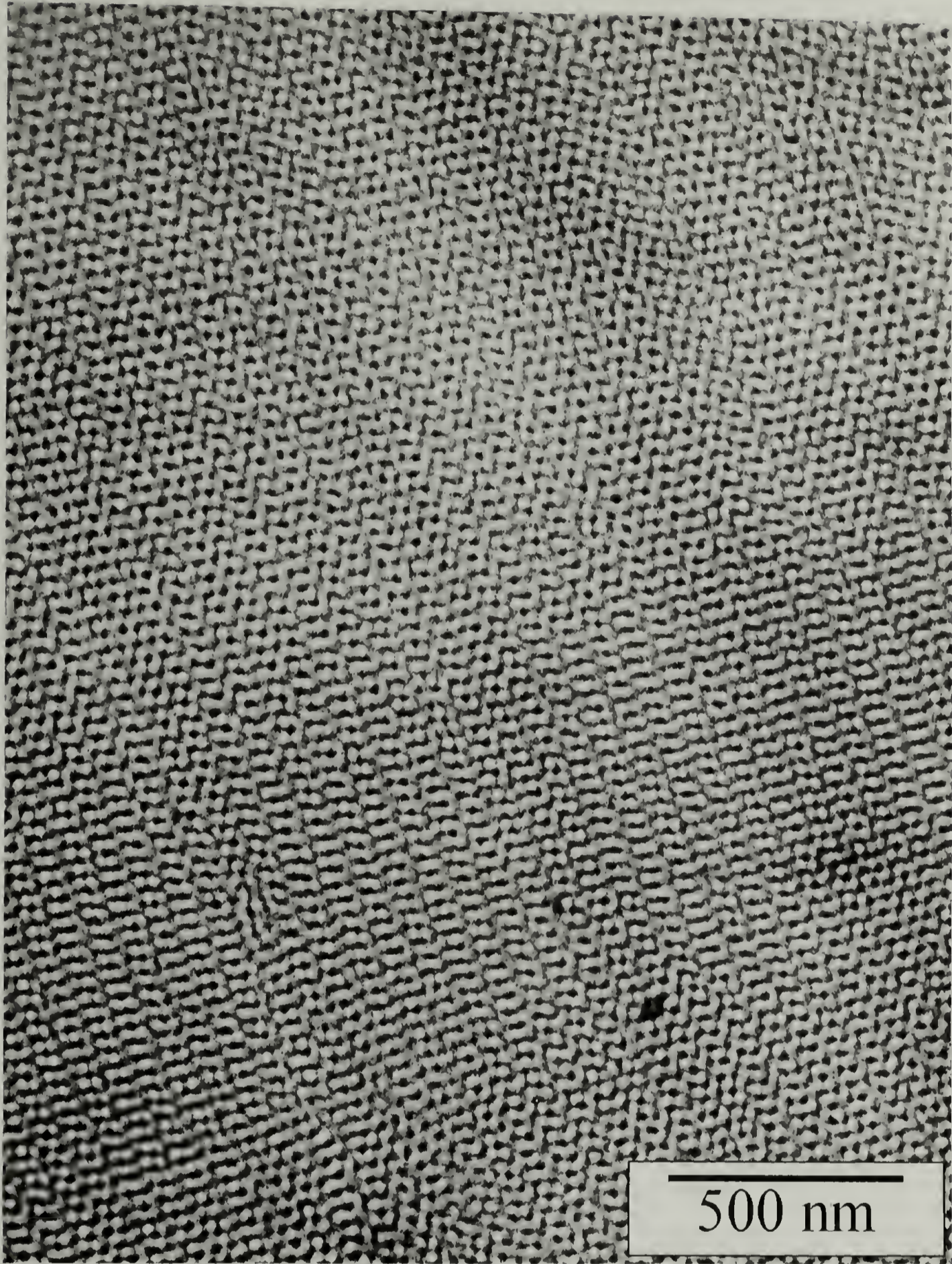
Figure 3.13.   TEM of IX35-32.
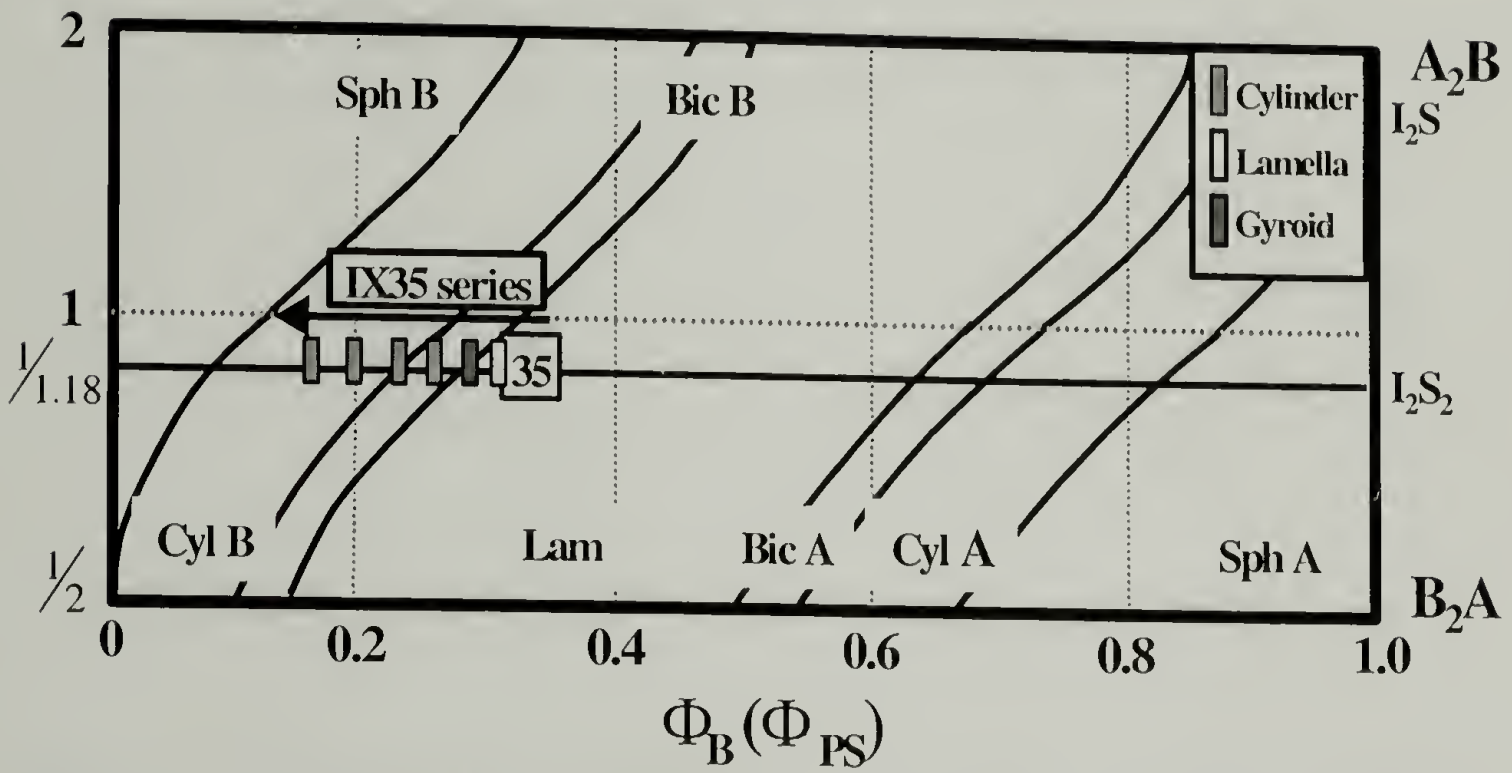
Figure 3.14.   Blend series IX35 mapped onto the theoretical morphology diagram.

CHAPTER 4

MORPHOLOGICAL BEHAVIOR I₅S MIKTOARM STAR BLOCK COPOLYMERS:PACKING CONSTRAINTS ON MORPHOLOGY AND DISCONTINUOUS CHEVRON TILT GRAIN BOUNDARIES

4.1   Abstract

A morphological study of three I_5S six-arm miktoarm star block copolymers and one I_5-S-I_5 dumbbell shaped graft block copolymer is presented. The miktoarm stars are comprised of five arms of polyisoprene (PI) and one arm of polystyrene (PS) joined together at a single junction point; the dumbbell shaped graft block copolymer is comprised of five arms of PI on each end of a single connecting block of PS. The strong segregation limit theory for the morphological behavior of miktoarm stars, predicts that these materials should form spherical morphologies, but only lamellar and cylindrical morphologies were observed by TEM and SAXS. These results are similar to previously reported discrepancies between experimentally observed morphological behaviors of miktoarm stars and the predictions of the theory. Previous work has attributed the discrepancies to the neglect of the effect of the multifunctional junction points on calculated free energies. The current results suggest that in addition to this, geometrical packing constraints prevent the formation of morphologies such as spheres and cylinders in highly asymmetric miktoarm stars in which the minor volume fraction component would need to occupy the matrix phase. Finally, unusual *broken chevron* tilt grain boundary morphologies were observed in a lamellar I_5S material. We attribute

106

these new structures to the asymmetric energy penalties for interfacial bending which result from the molecular asymmetry of the miktoarm stars.

4.2   Introduction

Branched and grafted molecular architectures have been shown to be an additional factor (in addition to volume fraction and degree of segregation) which affects the morphological behavior of block copolymers. Guided by the predictions of a mean field theory derived by Milner[11,83] for the morphological behavior of A_nB_m-type, miktoarm star block copolymers, work has focused on molecules with an array of architectures including A_2B stars,[1,7,87-89] A_3B stars,[90] A_nB_n stars,[9,10,105] A_5B stars[8] and multigraft architectures, which may be considered to be linear combinations of miktoarm stars.[3,106,107] These studies have borne out the predictions of the model in general, but have revealed systematic discrepancies. In the current study we further examine I_5S miktoarm star block copolymers, and an I_5-S-I_5 material; the molecular architectures of these materials are illustrated in Figure 4.1. I_5S stars have five arms of PI and one arm of PS per molecule, joined to each other at a single junction point. The dumbbell shaped I_5-S-I_5 molecule is comprised of five arms of PI on each end of a connecting block of PS. These materials equal the highest architectural asymmetries investigated thus far.[8]

The morphology of I_5S miktoarm stars is predicted by the Milner theory, which is strictly applicable only in the strong segregation limit. For architecturally and conformationally asymmetric block copolymer stars of type A_nB_m, the theory predicts

107

morphology as a function of B component volume fraction, ϕ_B, and a molecular asymmetry parameter, $\varepsilon = (n_A/n_B)(l_A/l_B)^{1/2}$. Here, n_A and n_B are the numbers of arms of block materials A and B, and $l_i = (V_i/R_i^2) = v_i/b_i^2$. V_i and R_i are the volume and radius of gyration of one arm of polymer i, while v_i is the segmental volume and b_i the statistical segment length of component i. Using segmental volumes of 132 $\mathring{A}^3$ (PI) and 176 $\mathring{A}^3$ (PS) and statistical segment lengths of 6.8 $\mathring{A}$ (PI) and 6.9 $\mathring{A}$ (PS), an ε of 4.4 is calculated for these materials.[108,109] The samples characterized have PS volume fractions of 0.58 (I_5S-58), 0.46(I_5S-46), 0.37(I_5S-37), and 0.66 (I_5-S-I_5-66).

4.3   Experimental

Three I_5S miktoarm stars of PI and PS were synthesized using anionic polymerization and controlled chlorosilane chemistry. The synthesis of the A_5B and A_5-B-A_5 type nonlinear block copolymers has been described in detail elsewhere.[110] All manipulations were performed in glass reactors under high vacuum. The reactors were previously washed with benzene solution of n-butyllithium and rinsed with benzene. Benzene was the solvent for all polymerizations and linking reactions. The PS and PI arms were synthesized separately using sec-butyllithium as initiator and then linked together with the hexafunctional chlorosilane 1,2-bis-trichlorosilylethane (Si_2Cl_6). The key synthetic step for I_5S was the preparation of PS-Si_2Cl_5, from PS-Li and Si_2Cl_6. For I_5-S-I_5 the critical step is the preparation of (PI)$_5$-Si_2Cl, from PI-Li and Si_2Cl_6. The I_5S and I_5-S-I_5 architectures were obtained by reaction of PI-Li with PS-Si_2Cl_5, and of α,ω-dilithium PS with (PI)$_5$-Si_2Cl respectively.

Table 4.1 lists the molecular characteristics of each sample. Membrane osmometry (MO) was performed in toluene at 35°C. Size-exclusion chromatography (SEC) with both refractive index and UV detectors (λ = 262 nm) was performed in tetrahydrofuran at 30°C on individual PI and PS arms prior to silane coupling as well as on the overall miktoarm architectures. Vapor pressure osmometry (VPO) was performed in toluene at 50°C. Proton nuclear magnetic resonance (^{1}H-NMR) was used to determine the weight fraction of PS in each sample. Finally, the weight fraction of PS in each sample was calculated by dividing the PS arm M_n, as measured by SEC, by the total M_n of the star, $M_n(\mu) = 5 \cdot (M_n(PI)) + M_n(PS)$. PS volume fraction was calculated for each sample using the mass fraction of PS measured by ^{1}H-NMR and bulk densities.[111]

Bulk films were cast from 4 weight percent solutions in toluene, a nonselective solvent for PI and PS.[112] Films approximately 2 mm thick were formed by allowing the solvent to evaporate slowly over a period of two weeks. The films were let stand at room temperature and atmospheric pressure for an additional week, then placed under vacuum at room temperature for one week to remove any residual solvent from the bulk material. The samples were subsequently annealed under vacuum for one week at 120°C. The samples were then cooled under vacuum to room temperature over a period of several hours.

Sample morphology was characterized using a combination of transmission electron microscopy (TEM) and small-angle X-ray scattering (SAXS). To prepare thin sections for microscopy, a Leica Ultracut UCT microtome equipped with a Leica EM

FCS cryogenic sample chamber operated at –110°C was used to cut sections approximately 500 Å in thickness. The sections were collected on TEM grids and stained four hours in OsO_4 vapor. A JEOL 100CX TEM, operated at an accelerating voltage of 100 kV, was used to image the stained sections. SAXS data were collected at the Advanced Polymers Beamline (X27C), located at the National Synchrotron Light Source at Brookhaven National Labs (BNL), Upton, NY. Two-dimensional scattering patterns were collected on Fujitsu image plates, then read by a Fujitsu BAS 2000 image plate reader. Custom software at BNL was used to subtract background noise and perform circular averaging. Data were collected for a wavelength of 1.307 Å and a camera length of 1410 mm.

4.4   Results

The results of the morphological characterization for the three I_5S materials are listed in Table 4.1. Circularly averaged, I vs. q SAXS data for all three I_5S samples as well as the I_5-S-I_5 sample are shown in Figure 4.2. The excellent long-range order exhibited by these samples is indicated by multiple higher order reflections. The $q_n/q*$ ratio of $1, \sqrt{3}, \sqrt{4}, \sqrt{7}, \sqrt{9}, \sqrt{12}, \sqrt{19}$ ...indicate that I_5S-37 and I_5S-46 form hexagonal morphologies. Here $q*$ is the scattering vector of the lowest angle primary scattering peak and q_n is the series of all scattering vectors for which peaks are observed. For I_5S-58 and I_5-S-I_5-66 the scattering vectors of the peaks occurring at integral multiples of $q*$ indicating a lamellar morphology. A two-dimensional SAXS pattern collected for sample I_5S-46 is shown in Figure 4.3. The remarkable long-range order of this sample results in up to 9 orders of single crystal-like reflections. Usually, single crystal-like

110

long-range order is achieved by melt state shear alignment[113,114] or roll-cast [115,116] and is seldom achieved simply by solvent casting. From the SAXS data, the lamellar long periods of I_5S-58 and I_5-S-I_5-66 were found to be 49.7±0.5 nm and 45.2±0.5 nm, respectively. The scattering vector ratios found from the SAXS on I_5S-46 and I_5S-37 were consistent with cylinders on a hexagonal lattice with (100) spacing of 52.1±0.5 nm and 47.0±0.5 nm, respectively. Shown in Figure 4.4 shows representative TEM micrographs, which confirm that I_5S-58 and I_5-S-I_5-66 form lamellar morphologies, and I_5S-46, and I_5S-37 form cylindrical morphologies..

4.5   Discussion

If we considered the dumbbell shaped I_5-S-I_5 as a combination of two I_5S miktoarm stars, an approach used by several studies of multigraft block copolymer architectures,[3,106,107] the I_5-S-I_5-66 should have similar morphology to that of an I_5S with polystyrene volume fraction of 66%, and an overall molecular weight of 101,500 g/mol. According to the previous study of Beyer, Gido, and co-workers[8] I_5S star block copolymers with 66% PS volume fraction should form a lamella morphology, in agreement with the observed lamella morphology of I_5-S-I_5-66. The previous study reported a lamellar spacing of 42.7±0.5 nm for an I_5S-60 block copolymer sample with 0.60 PS volume fraction and a molecular weight of 128,000 g/mol (PS arm molecular weight of 76,000 g/mol and PI molecular weight of 10,400 g/mol per arm). The I_5S unit of the I_5-S-I_5 sample has a PS arm molecular weight of 54,000 g/mol and PI arms molecular weight of 7,400 g/mol, both are smaller than that of I_5S-60. Interestingly, the

111

I_5-S-I_5-66 sample has a lamellar spacing of 45.2±0.5 nm, which is larger than that of I_5S-60. The previous study[8] also reported the lamellar spacing of I_5S-67 with total molecular weight of 152,000 g/mol (106,000 g/mol for the PS arm and 9,700g/mol for each PI arm) to be 47.9±0.5 nm. At basically the same composition the I_5S-67 sample has 50% greater molecular weight than the corresponding half of the I_5-S-I_5-66 architecture, yet its lamellar spacing is only 6% larger. These comparisons indicate that the two junction point structure of I_5-S-I_5-66 results in a larger domain spacing than its respective I_5S structural unit.

The three I_5S samples characterized in this paper are plotted on the morphology diagram in Figure 4.5 along with data from samples from four previous works involving A_2B, A_3B, A_2B_2 and A_5B miktoarm star block copolymers[8,9,87,90]. Those samples found to have morphological behavior differing from their theoretically predicted morphologies are shaded. This figure reveals an increase in the frequency of discrepancies between predicted and observed behaviors with increasing molecular asymmetry. As indicated in Figure 4.5, the theory predicts that the three I_5S samples of this study should form spheres. Sample I_5S-58 is found experimentally to form a lamellar morphology and both samples I_5S-46 and I_5S-37 are found to form cylinders of PS. This discrepancy is in agreement with the general trend observed in prior studies.

As with previous studies, samples that disagree with theoretical predictions exhibit morphologies that should occur at lower ε for a given ϕ_B, or at a higher ϕ_B for a given ε. For example, Beyer, Gido and co-workers[8] found that their I_5S-60 sample formed lamellae instead of the predicted cylinder of PS. While ε for I_5S-60 was

112

calculated to be approximately 4.4, for the same volume fraction, lamellae occur at a maximum of $\varepsilon \approx 3.0$. Alternately, for $\varepsilon = 4.4$, cylinders are predicted to occur for ϕ_B greater than 0.59, but are observed at ϕ_B of 0.37. If similar comparisons are made for all the samples that disagree with the theory, one finds that the overestimation of morphological shift increases with asymmetry; slight discrepancies at low values of ε become greater as asymmetry increases. This is represented graphically in Figure 4.5, which shows a plot of $\Delta\varepsilon$ as a function of increasing ε, where $\Delta\varepsilon$ is the negative shift in ε required to bring a sample into agreement with the diagram. The I_5S-37 sample, for example, would have $\Delta\varepsilon$ of 4.4 - 2.5 = 1.9. Plotted as a function of ε, the maximum of $\Delta\varepsilon$ increases with ε. These trends can only be represented approximately given the limited experimental data available, i.e. the data points available do not necessarily represent the limits of the discrepancy between theory and experiment at each value of ε.

Recently, Gido and co-workers[9,106] and others[117,118] have postulated that discrepancies between the Milner theory and experimental results, as illustrated in Figures 4.5 and 4.6, are a result of additional chain stretching inherent in the miktoarm star architecture due to crowding of multiple arms linked to a single junction point. Our current data suggests that, as architectural asymmetry (arm number asymmetry) becomes large, geometric packing constraints also exert an important influence on morphology. Milner's calculation was based on the assumption of a rounded Wigner-Seitz cell surrounding each domain.[11] In order for cylindrical and spherical domains to fill space they must occupy true, space filling polyhedral Wigner-Seitz cells and deform

113

to fill the corners of these cells.[83,119]   Therefore, the energies calculated with the rounded cell approximation (upon which Figure 4.5 is based) represent lower bounds. When the volume fraction of the component, which forms the core of the cylinder or sphere, is small (as in diblock copolymers), packing problems are not very important. However, as the molecule becomes more and more asymmetric, the volume fraction of the multi-arm component on the convex side of the interface may decrease to the point where it approaches the volume fraction of the interstitial space in a close packing of spheres.   For example, at $\varepsilon = 5$ and $\phi = 0.6$, the morphology diagram predicts a spherical morphology with the 0.6 volume fraction component inside the spheres and only 0.4 volume fraction in the matrix between spheres.   However, the maximum volume fraction that solid spheres in a bcc packing can occupy is only 0.65.   Real spherical block copolymer domains will not be able to achieve or even closely approach the solid contact limit for packing density of the domain cores, due to the severe conformational distortions which would be required for the corona blocks.   Thus we expect that geometric packing limits will prevent increasing shifts to higher ϕ of the true experimentally determined order-order transition lines in Figure 4.5 as ε becomes large.   A similar geometric packing limit will also apply to the cylindrical morphology. At these limits the order-order transitions will become vertical lines on the morphology diagram.   On Figure 4.5, we have sketched the approximate positions, based on experimental data, of geometrical packing limits for spherical and cylindrical morphologies.

In the lamella forming sample, I$_5$S-58, unusual chevron tilt grain boundary morphologies were observed, as shown in Figure 4.6. Previous experimental[120-123] and theoretical studies[124,125] of symmetric tilt grain boundaries in diblock copolymers have reported chevron tilt boundaries, as illustrated in Figure 4.7, in which lamellar layers retain their continuity while bending cooperatively in a narrowly defined boundary region. Figure 4.6 shows what we will call broken chevrons that occur in the I$_5$S material. In Figure 4.6a, the lamellae on both sides of the boundary terminate at the boundary in rows of semicylindrical end caps similar to those observed in T-junction tilt boundaries.[120,126] In Figure 4.6b, some lamellae terminate at the boundary in semicylindrical end caps and additionally individual complete cylinders occupy the symmetry plane of the chevron boundary. We will call this type of boundary a broken chevron with cylinders. Previous work[120,124,125] showed that at high tilt angles the lamella forming a chevron boundary develop protrusions parallel to the plane of the boundary resulting in Ω and extended-Ω variants of the chevron. The protrusions are necessary in order to fill space to constant density in the plane of the chevron grain boundary at high tilt angles. Figure 4.6c shows that the I$_5$S material forms a broken form of the Ω-boundary with additional cylindrical domains in the plane of the boundary. Recently Qiao and Winey[123] have published TEM images of Ω-boundaries in diblock copolymers formed in sheared samples which also contain some cylindrical domains localized in the plane of the boundaries. Unlike Figure 4.6c, the lamellae involved in Winey's chevrons remain continuous across the grain boundaries.

115

We postulate that the discontinuous nature of chevron tilt grain boundaries in I$_5$S-58 results from an asymmetry in the energy penalties for interfacial bending due to the asymmetry inherent in the I$_5$S molecular architecture. At 0.58 PS volume fraction this material forms flat lamellar interfaces at equilibrium. However, bending of these interfaces is necessary to form a chevron tilt grain boundary. As shown in Figure 4.9a, the standard chevron boundary involves equal degrees of interfacial curvature both toward and away from the five-arm PI side of the interface. Due to crowding inherent in packing five arms of PI on the same side of the interface and the fact that curving the interface toward the PI side will exacerbate chain stretching resulting from this crowding, it may be energetically more costly to bend the interfaces toward the PI domains than toward the PS domains in an I$_5$S architecture. By replacing the standard cheveron structure with a broken or discontinuous structure as illustrated in Figure 4.9b, it is possible to achieve the required tilt reorientation using only interfacial curvatures which put the five PI arms on the convex side of the interface. In order to do this, however, it is necessary to produce higher interfacial curvatures capable of generating semicylindrical end-caps on lamellae and isolated cylinders in the grain boundary plane. For this reason the broken chevron structures are only observed at relatively high tilt angles. For instance the tilt angles of the broken chevrons in Figure 4.7 a and b are about 90°. Presumably, as tilt angle increases a transition occurs from continuous to discontinuous chevron structure at the point where the energy penalty for the highly unfavorable bending toward the five PI arms (Figure 4.9a) first exceeds the energy to form cylinders and cylindrical caps with the five PI arms on the convex side of the interfaces (Figure 4.9b).

4.6   Conclusions

As seen in prior studies, the Milner theory for the morphology of miktoarm star block copolymers exhibits a systematic tendency to overestimate the effect of architectural asymmetry on morphology. This tendency becomes exaggerated with increasing asymmetry as in the I_5S samples of this study. Here we report a vertical straightening of the order-order transition lines in the morphology diagram at high ε due to packing constraints inherent in placing a relatively small volume fraction material in the matrix around microphase separated domains. New discontinuous chevron tilt grain boundary morphologies were observed in a lamella forming I_5S material. The discontinuity of these boundaries is thought to result from asymmetric energy penalties for bending of the lamellar interfaces. It may be more energetically costly to curve interface toward the five arm per molecule PI side of the interface than toward the single arm per molecule PS side of the interface.

Table 4.1.　　Molecular and morphological characterization information for the three I_5S miktoarm stars and the dumbbell shaped I_5-S-I_5 graft block copolymer.

			I_5-S-I_5-66	I_5S-58	I_5S-46	I_5S-37
PS arm	Mn (g/mol)	MO	118000	105000	78000	53000
	M_w/M_n	SEC	1.07	1.03	1.04	1.03
PI arm	Mn (g/mol)	MO	7400	16300	16300	16300
	M_w/M_n	SEC	1.04	1.03	1.03	1.03
Overall	Mn (g/mol)	MO	203000	180000	162000	133000
	Mw (g/mol)	LALLS	223000	193000	173000	141000
	M_w/M_n	SEC	1.09	1.01.07	1.07	1.06
	Mass % PS	^{1}H-NMR	69	61	49	40
	Mass % PS	UV/SEC	67	60	47	37
	Mass % PS	calc	65	58	48	40
	Vol % PS		66.1	57.8	45.6	36.8
	$2\pi / q^*$ (± 0.5 nm)		45.2	49.7	52.1	47.0
	Predicted Morphology		Lamella	Sphere	Sphere	Sphere
	Observed Morpholody		Lamella	Lamella	Cylinder	Cylinder
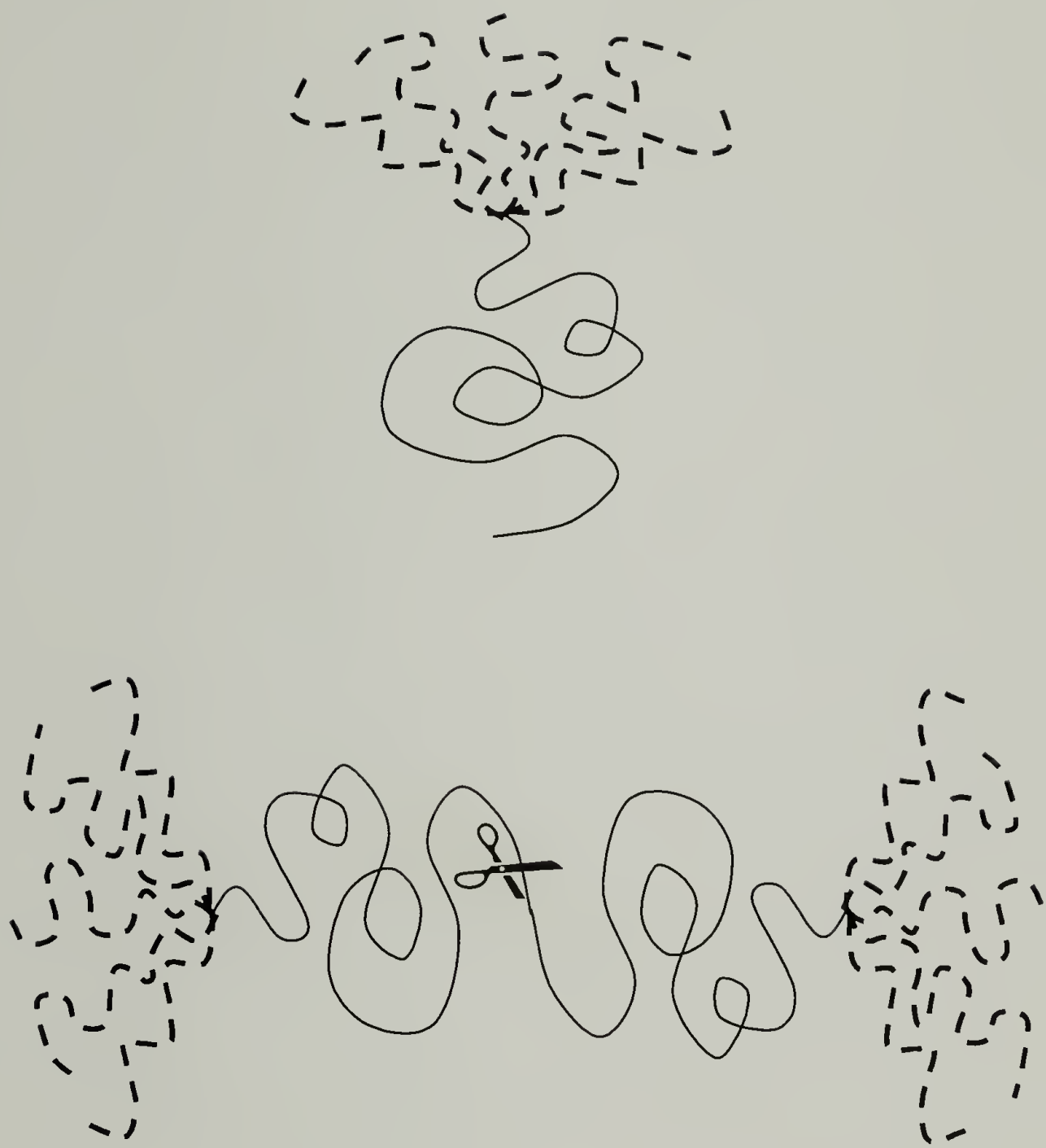
Figure 4.1.   Illustration of the molecular architecture of an I_5S miktoarm star block copolymer and dumbbell shaped I_5-S-I_5 graft block copolymer.
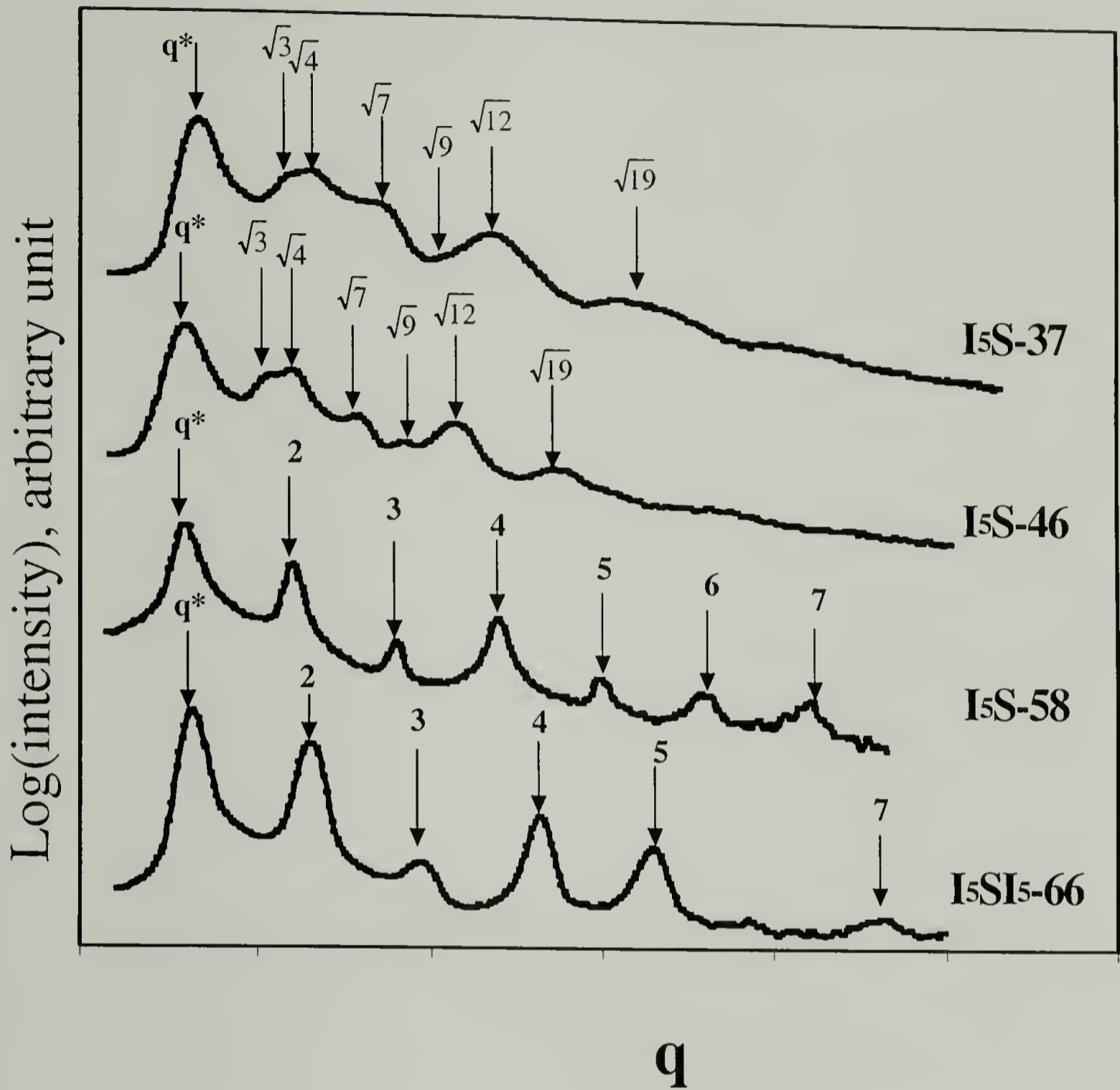
Figure 4.2.　　log(I) vs. q SAXS data for the I_5S and the I_5-S-I_5 samples.
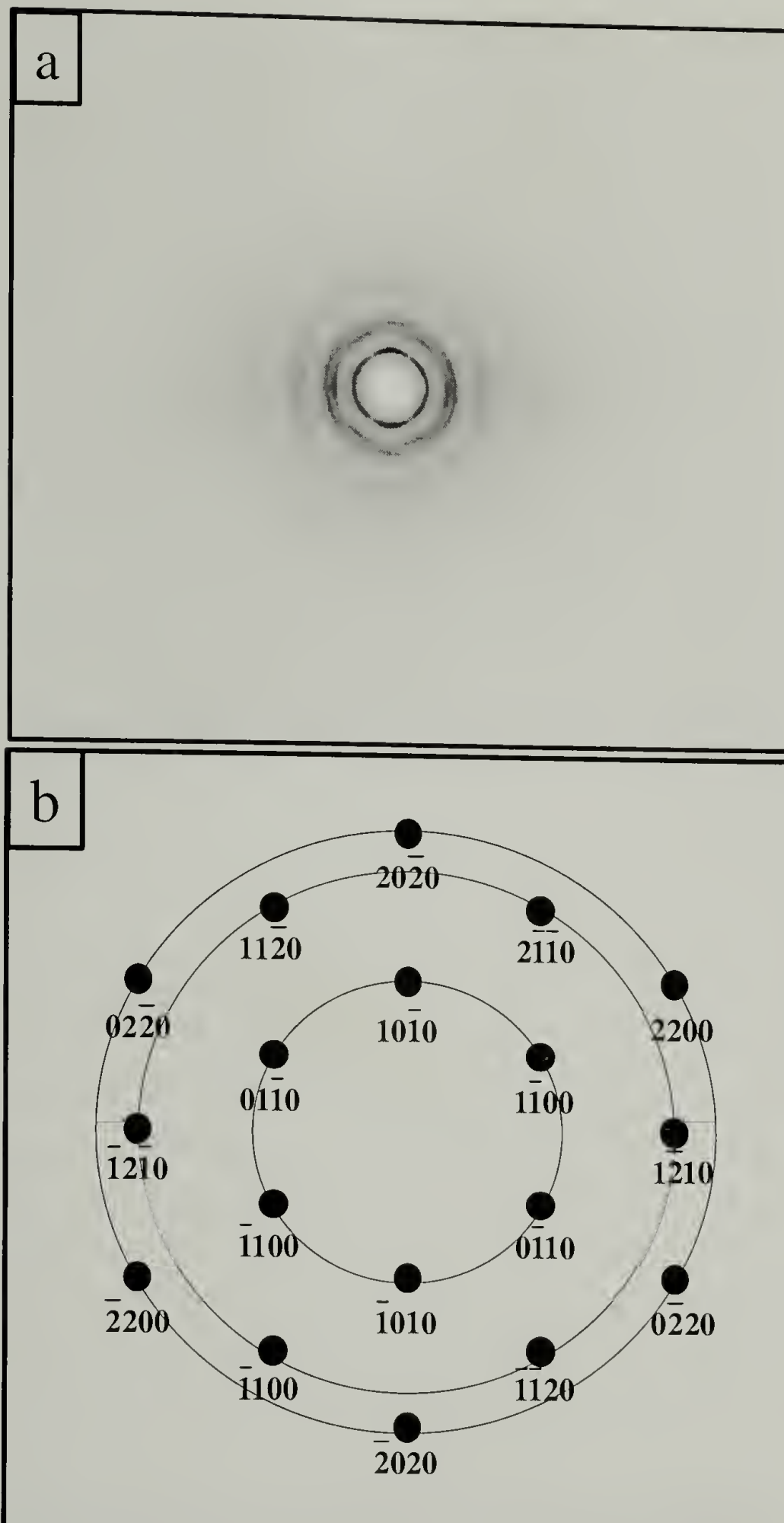
Figure 4.3. Two-dimensional SAXS for sample I₅S-46: (a) data, (b) indexed schematic.

121

500 nm

500 nm

500 nm

124
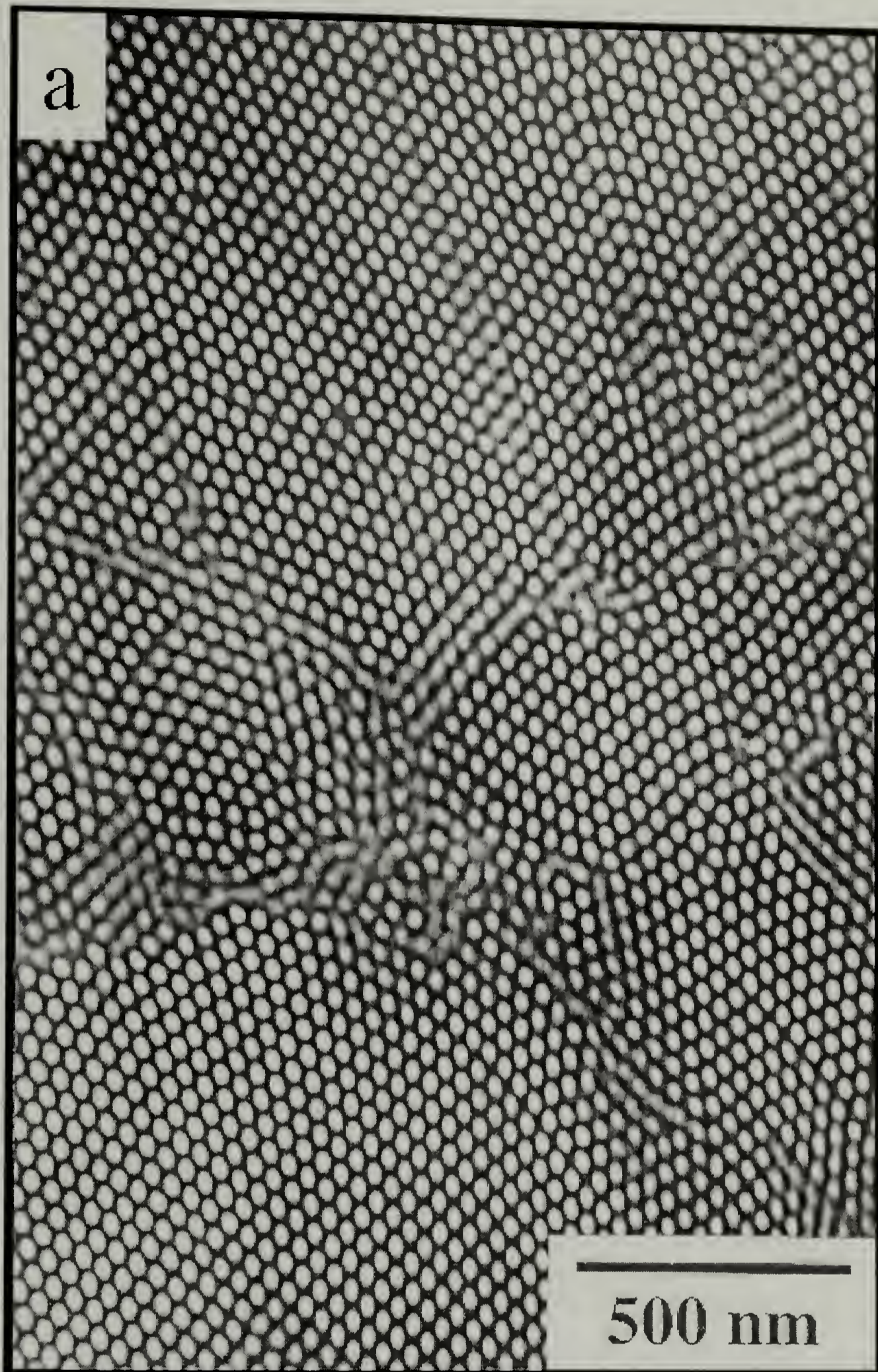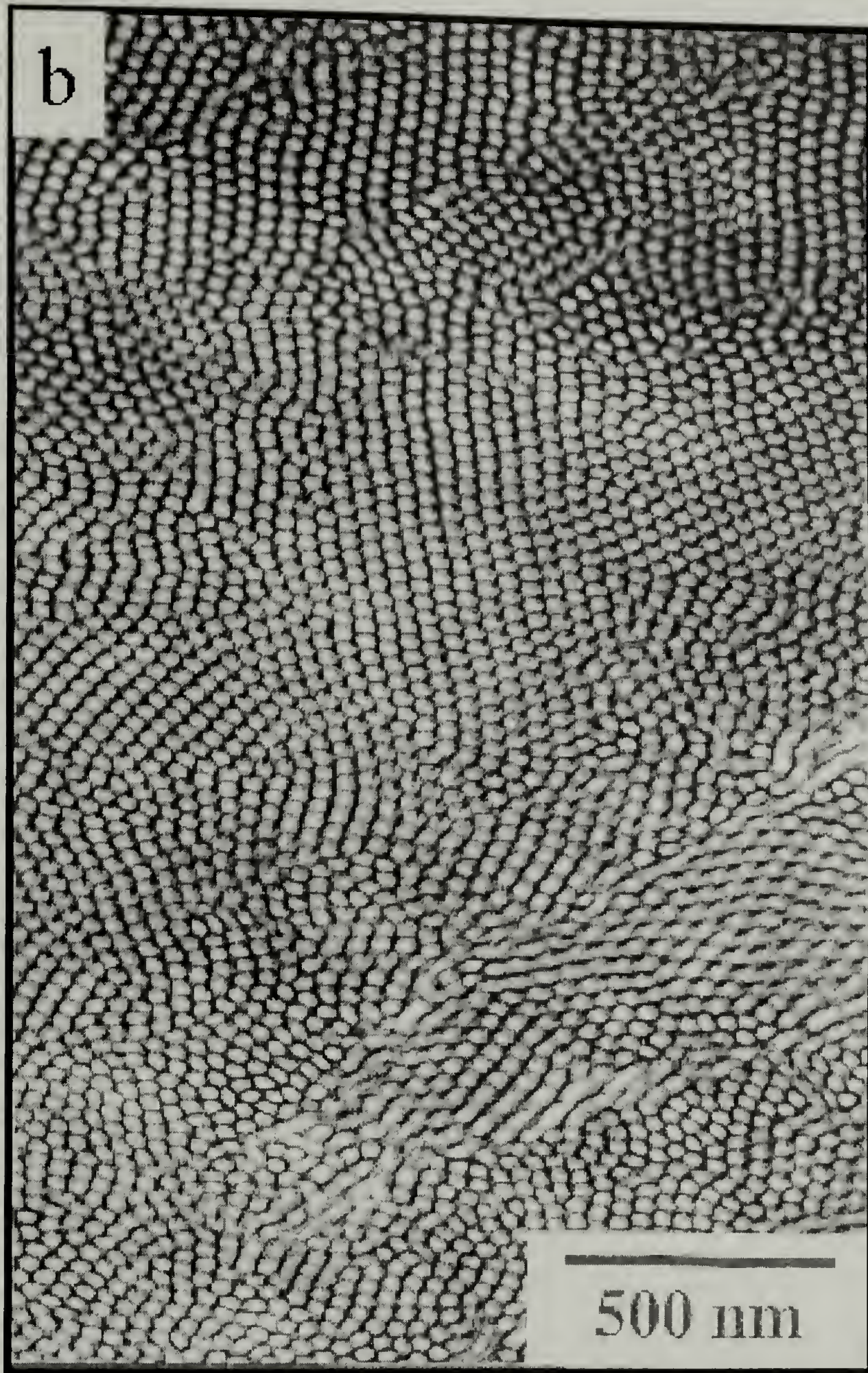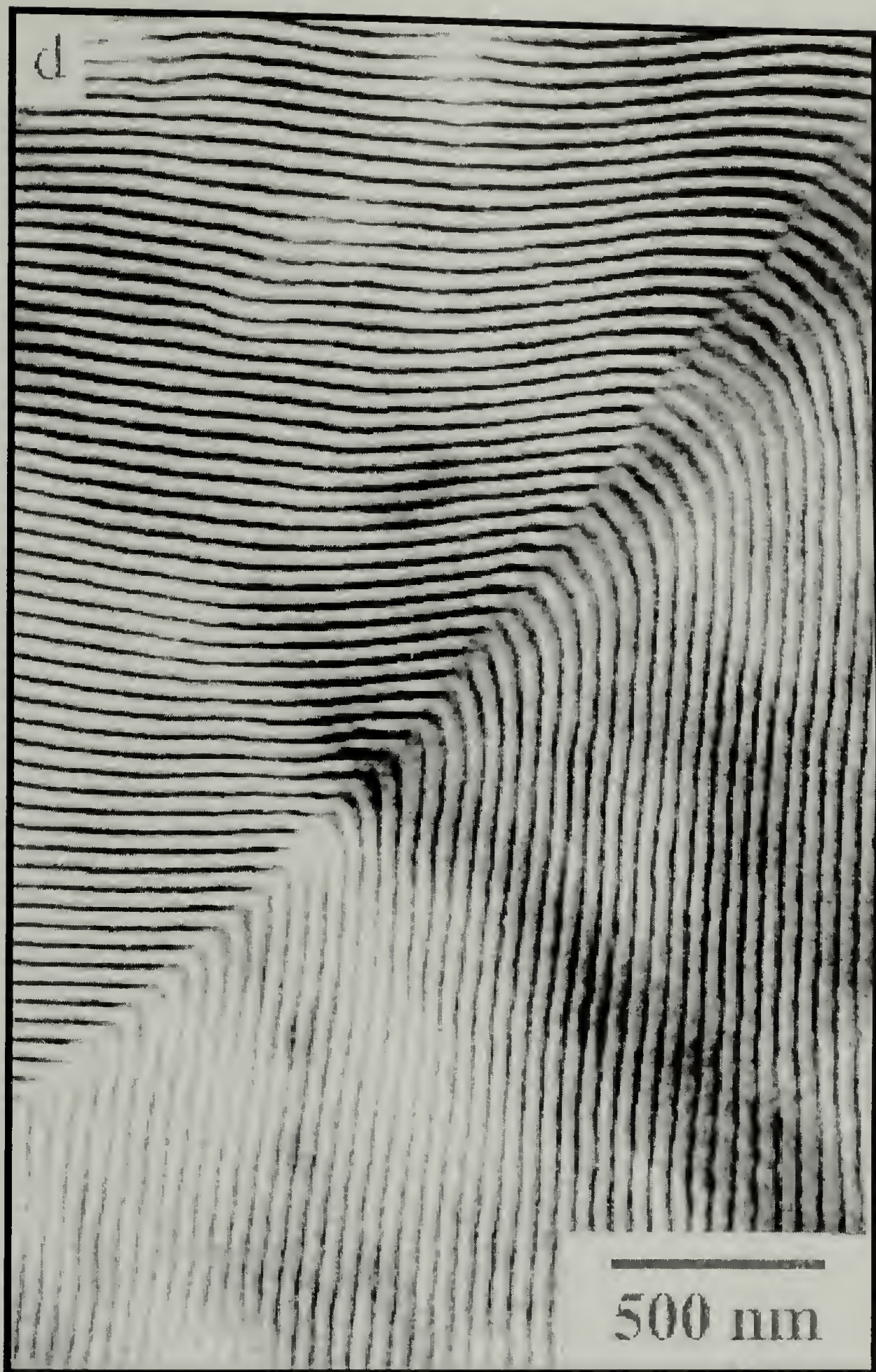
Figure 4.4.   TEM micrographs of I_5S and I_5-S-I_5 samples (a) I_5S-46, (b) I_5S-37, (c) I_5S-58 and (d) I_5-S-I_5-66.

125
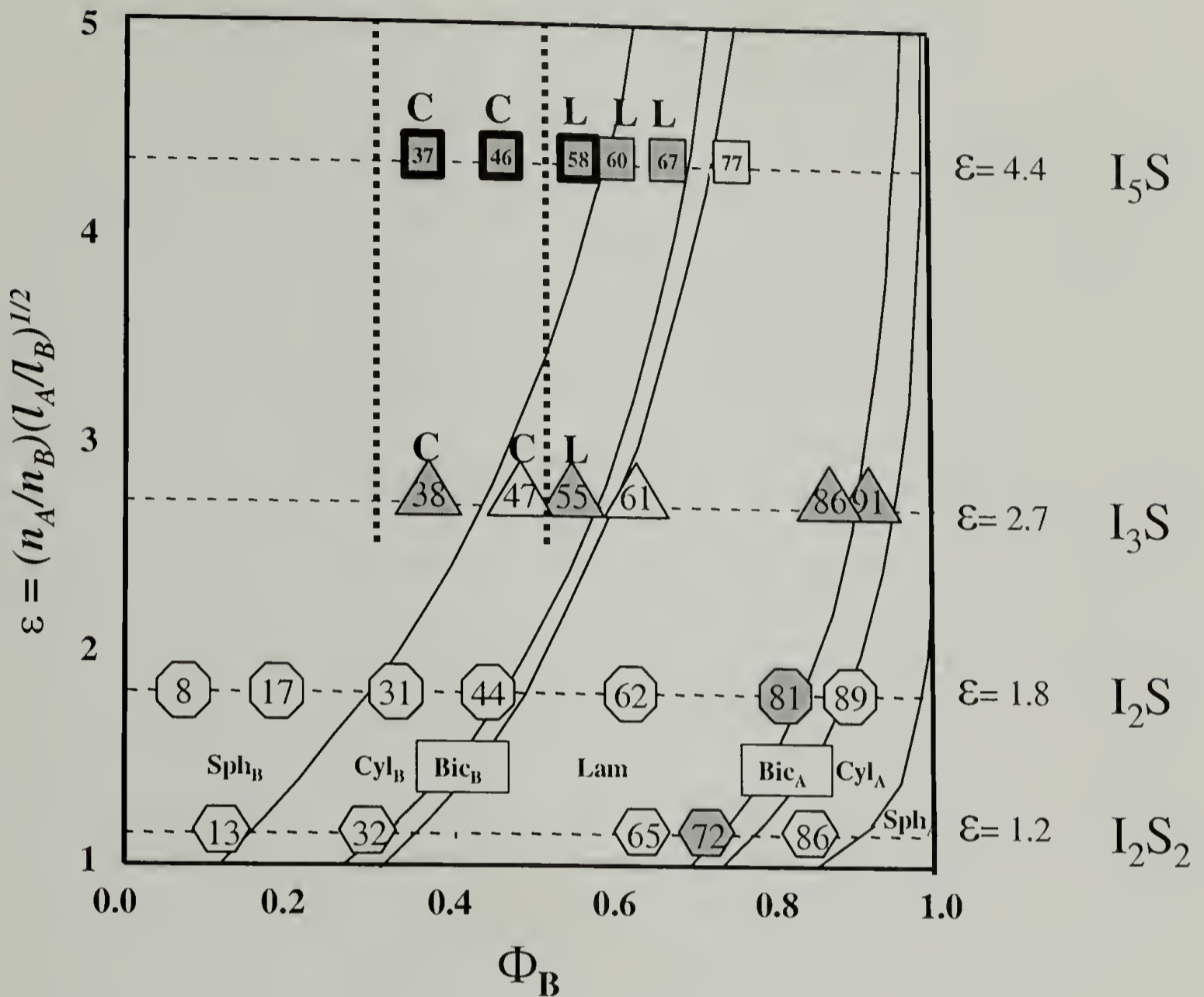
Figure 4.5. The morphology diagram generated by the Milner model. Morphology is given for the volume fraction of the B component, ϕ_B, and molecular asymmetry, ε. The A_5B stars are represented by squares while A_2B stars are represented by circles, A_3B stars by triangles, and A_2B_2 stars by pentagons. Shaded symbols indicate samples whose morphologies disagree with that predicted by theory. Boldly outlined symbols indicate samples characterized in this study.
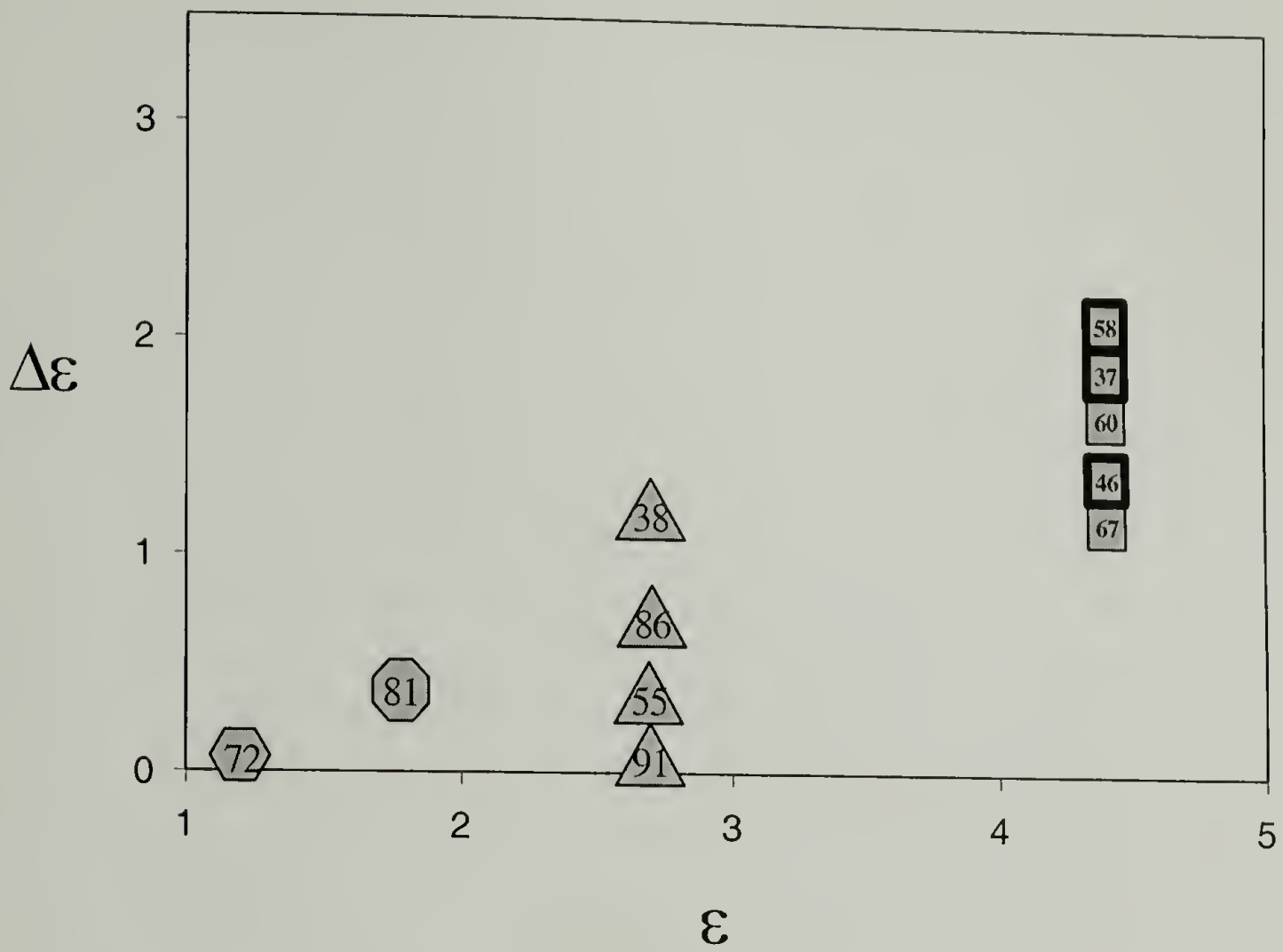
Figure 4.6.   Values of Δε for samples exhibiting morphologies other than those predicted by theory, as a function of ε, for the data shown in Figure 4.5. Boldly outlined symbols indicate samples characterized in this study.

300 nm

128
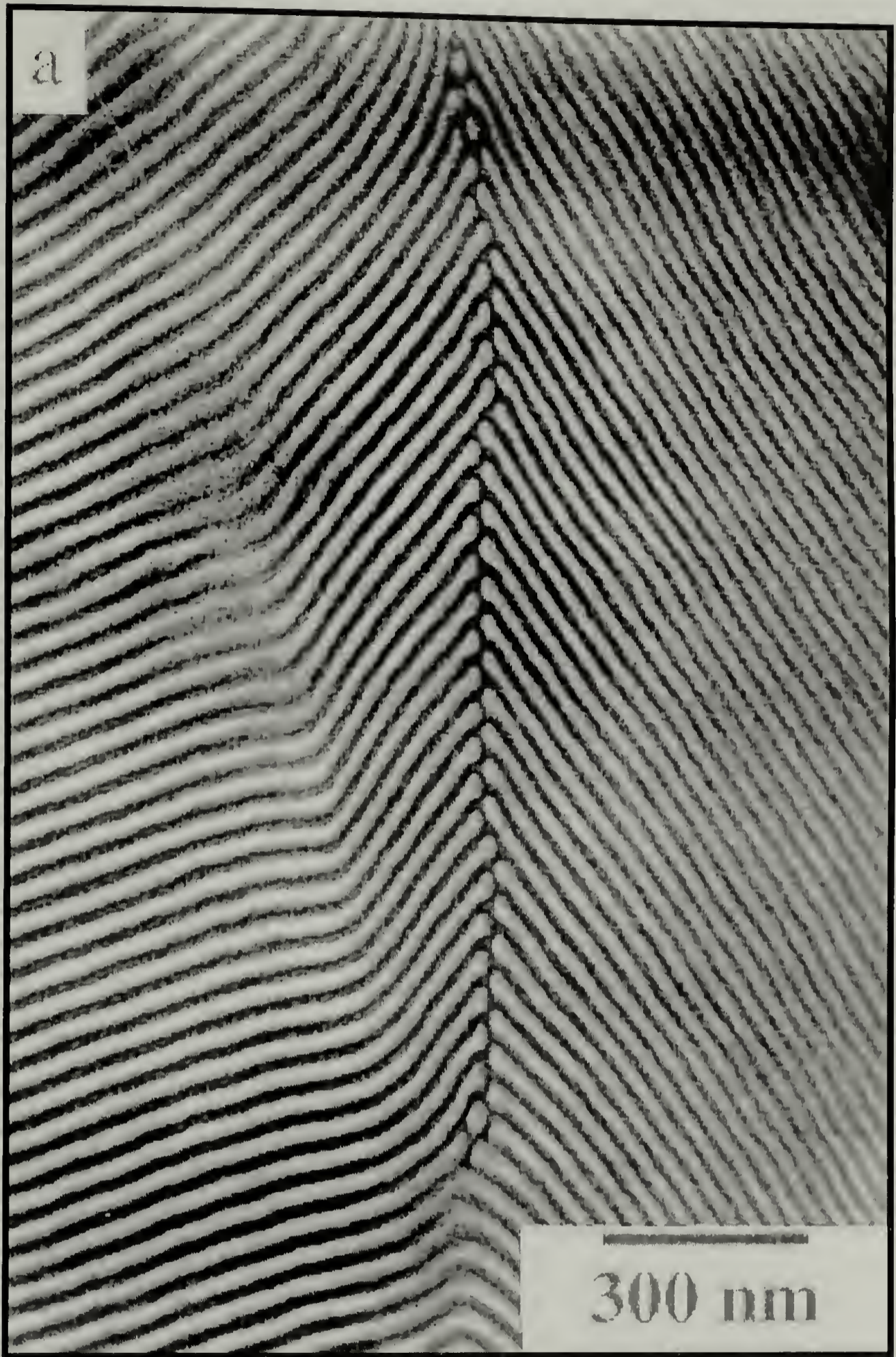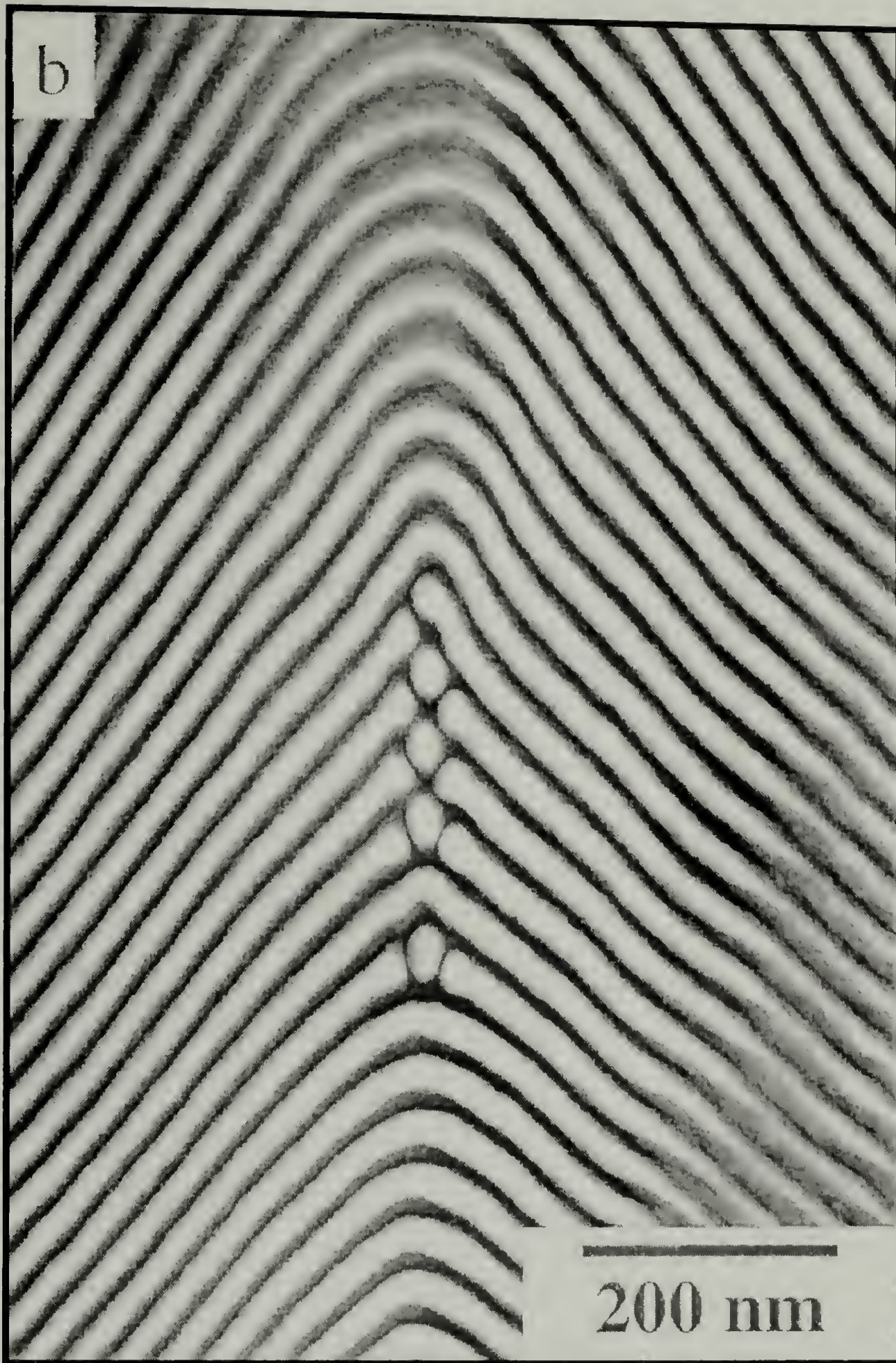
Figure 4.7.   I₅S-58 Symmetric tilt grain boundaries (a) broken chevron, (b) broken chevron with cylinders, (c) broken Ω with cylinder.

130
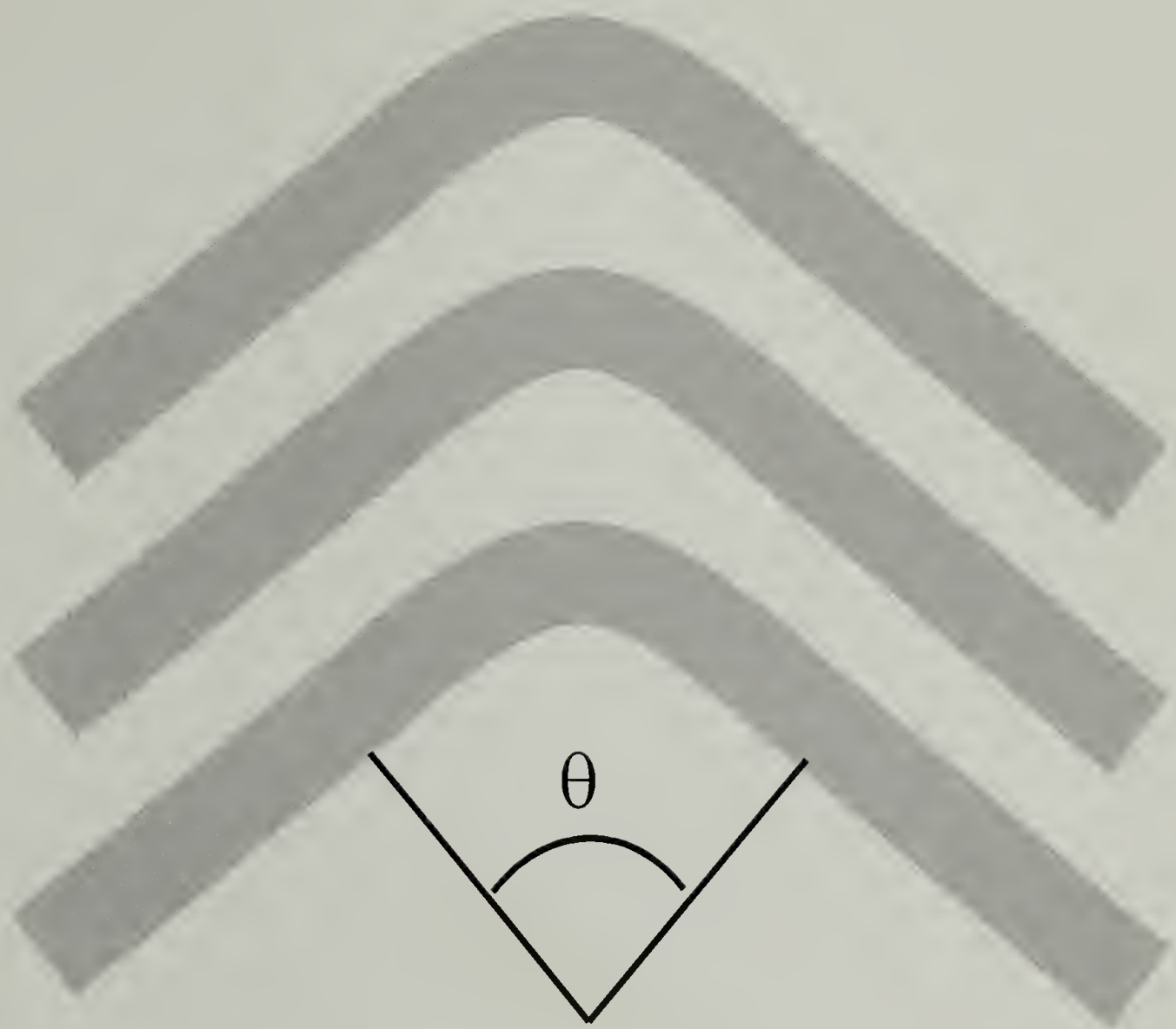
Figure 4.8.   Schematic of commonly observed chevron tilt boundaries.
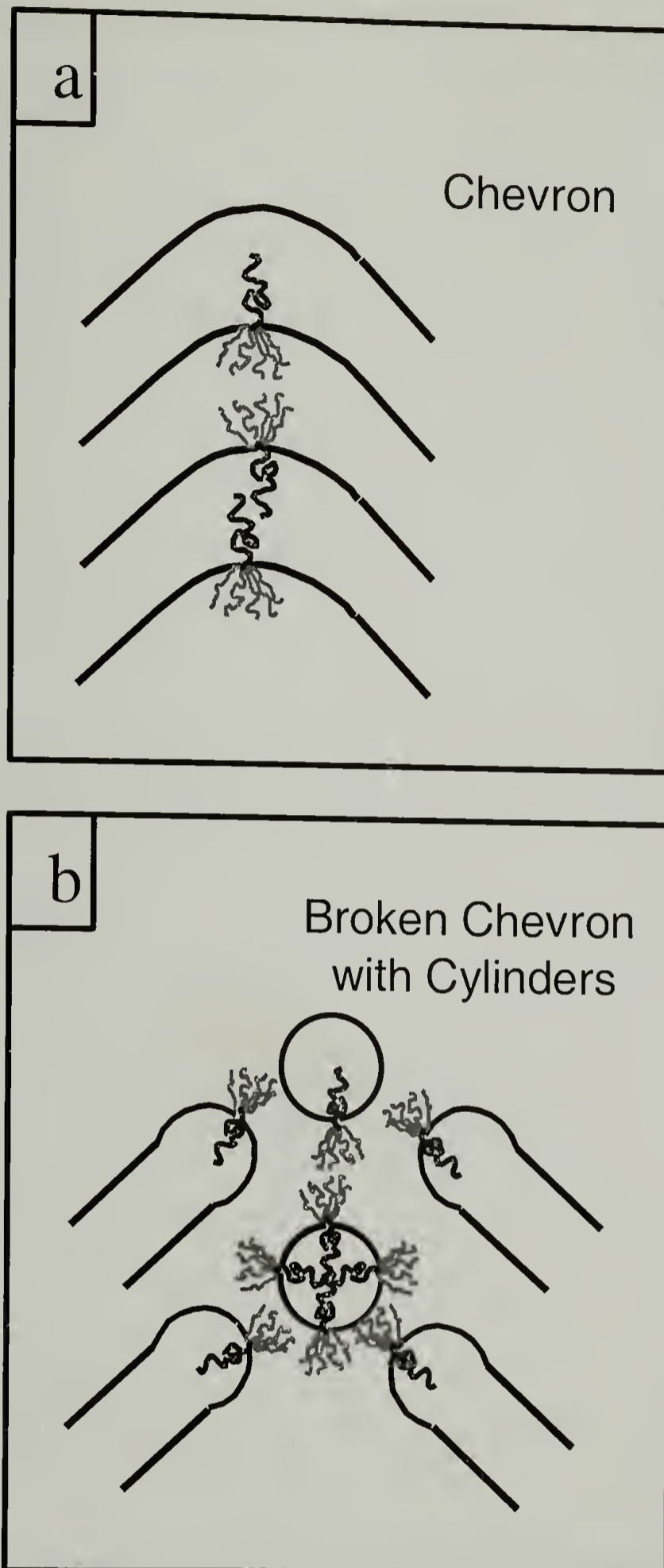
Figure 4.9. (a) illustration of chevron tilt boundaries for I_5S samples, (b) illustration of broken or discontinuous chevron tilt boundaries for I_5S samples.

CHAPTER 5

MORPHOLOGICAL TRANSFORMATION FROM LAMELLA TO CYLINDER

5.1   Abstract

Casting from selective solvent cyclohexane, *mikto*arm star block copolymer I₃S-86 forms kinetically trapped, quasi-stable lamella morphology. I₃S-86 has three polyisoprene arms and one polystyrene arm connected at a single junction point. Heated above Tg, the selective solvent cast I₃S-86 transforms from the kinetically trapped lamella morphology towards its stable cylinder morphology. The slow dynamics of the high molecular weight, non-linear I₃S-86 block copolymer enable us to study the irreversible morphology transformation from lamella to cylinder at different intermediate stages. TEM analysis of these stages indicates that the perforated lamella morphology is an intermediate stage during lamella to cylinder transformation, and that the series of transformations from lamella to perforated lamella then to disordered worm structure occur within the original lamella planes.

5.2   Introduction

Selective solvent can be used to control block copolymers' morphologies.[2,32,44,103] Thermal annealing of these kinetically trapped morphologies can provide us information about the path of transformations among these morphologies. Branched and grafted molecular architectures also have been shown to be an additional

133

factor (in addition to volume fraction and degree of segregation) which affects the morphological behavior of block copolymers. Guided by the predictions of a mean field theory derived by Milner[11,83] for the morphological behavior of A_nB_m-type, miktoarm star block copolymers, work has focused on molecules with an array of molecular architectures including A_2B stars and their homopolymer blends,[1,7,54,87-90] A_3B stars,[90] A_nB_n stars and their blends with homopolymers,[9,10,105,127] A_5B stars,[8,102] multigraft architectures.[3,106,107] Branched architecture also slow down the dynamics of polymers. Both kinetic and thermodynamics play an important role on the morphologies of block copolymer systems. In this study, selective solvent and the slow dynamic of an I_3S *mikto*arm star block copolymer enable us to study the details of lamella to cylinder transformation.

The I_3S *mikto*arm star block copolymer used in the study consists of three equal length arms of polyisoprene (PI), and one arm of polystyrene (PS), linked at a common junction point. The molecular architectures of this material are illustrated in Figure 5.1. The M_n of PI arm is 7,600 g/mol; the M_n of PS arm is 180,000 g/mol; the total M_n of the I_3S molecule is 204,000 g/mol. This particular I_3S material was calculated to have 86% PS in volume and is referred to as I_3S-86. Milner's model predicted this sample to form a lamella morphology, however, a previous experimental study found the sample to form PI cylinder morphology.[90]

Hexagonally perforated lamellae, which resemble the cantenoid-lamellar structure derived by periodic area-minimizing surfaces calculations,[48] were also observed recently in linear diblock systems[35,37-39,46,49-52] in a narrow volume fraction

134

region between HEX and LAM and in block copolymer / homopolymer blends.[22,53,54] Controversy exists regarding some structure details of the perforated lamella structure and the stability of the morphology. Both ABC stacking of the hexagonally perforated layers[38,52] and a combination of an ABC and AB stacking[39] were suggested for the perforated lamellar morphology. Regarding the stability of the morphology. The experimental studies by Hajduk *et.al.* suggest that perforated lamella is an unstable morphology involved in lamella to Gyroid transition. However, in a recent study by Yang, Gido and coworkers, perforated lamella was observed in a solvent cast blend sample of graft block copolymer and homopolymer, and the morphology persisted during thermal annealing. These observations suggest that perforated lamella can be stable or meta-stable. Using the methods of Semenov[55] to estimate the free energy of perforated lamella in the strong segregation limit, Fredrickson[56] showed that the perforated lamella is metastable with respect of cylinders and lamella at $\phi=0.35$. Qi and Wang[57-59] showed that the perforated lamellae appear as a "pseudostable" morphology during the lamellar to cylinder transition. However, this prediction has not been proved experimentally.

5.3   Experimental

The detailed synthesis and molecular characterization of the sample was reported previously.[90] Bulk samples were prepared by dissolving the block copolymer in solution (5 weight percent) and then slowly evaporating the solvent over two weeks. Two solvents with different affinities for the two block materials were used: toluene, a non-selective solvent; cyclohexane, a selective solvent for PI. After getting solid cast

films with approximately 1mm thickness, residue solvent was further removed from these films by holding them at room temperature in a vacuum oven for two weeks. Then, the samples were annealed in a vacuum oven at various temperatures and for various lengths of time.

The morphologies were characterized by transmission electron microscopy (TEM). To prepare thin sections for microscopy, a Leica Ultracut UCT microtome equipped with a Leica EM FCS cryogenic sample chamber operated at $-110^{\circ}C$ was used to cut sections approximately 500 Å in thickness. The sections were collected on TEM grids and stained four hours in OsO_4 vapor. The PI microdomains are preferentially stained by OsO_4, rendering them dark relative to PS microdomains due to mass-thickness contrast in the TEM. A JEOL 100CX TEM, operated at an accelerating voltage of 100 kV, was used to image the stained sections.

5.4   Results

I_3S-86-A: Sample Cast From Toluene and annealed at $120^{\circ}C$ for two weeks.

After cast from toluene, a neutral solvent, I_3S-86 forms ordered cylinder morphology (TEM micrograph no shown). This morphology persists during thermal annealing at $130^{\circ}C$ for 2 weeks (TEM micrograph no shown). This observation agrees with a previous study by Hadjichristidis and coworkers.[90]

I_3S-86-B: Sample Cast From Cyclohexane.

When cast from cyclohexane, a selective solvent for polyisoprene, I_3S-86 forms lamella morphology. A TEM micrograph of the lamella morphology is shown in Figure 5.2a. Because cyclohexane is selective for polyisoprene, it increases the effective volume fraction of polyisoprene and the block copolymer system form lamella morphology in concentrated solution. As the solvent evaporates, the I_3S material reaches its Tg and lost the mobility to rearrange itself into its stable morphologies, and the lamella morphology is kinetically trapped.

I_3S-86-C: Sample I_2S-89-B annealed at 110°C for 3 days.

After annealing I_2S-89-B at 110 °C for 3 days the morphology of cyclohexane cast I_3S-86 showed some interesting changes. A typical TEM micrograph is shown in Figure 5.2b. In the image, we can still see the structure feature of alternating PS PI layer. However, the dark PI layers were perforated by PS materials as indicated by the white "holes" in the dark PI layers.

I_3S-86-D: Sample I_3S-86-C further annealed at 120°C for 7 days.

After annealing the sample I_3S-86-C at 120°C for a week, further structural evolution was observed. A TEM Tilting series of this sample is shown in Figure 5.3. From the TEM micrographs, we can see, after tilting 20 degree around the indicated tilting axis, the perforated structures near the center of Figure 5.3a becomes a regular side projection of perforated lamella, which is an indication that the basic alternating PS PI layer structure is still maintained, the perforation process continues in the PI layers. The TEM micrographs also showed that the general sizes of the PS perforations in the PI layers of I_3S-86-D are bigger than that of the I_3S-86-C. Due to the high PS

137

volume fraction of 0.86, the PI material adopts a mesh-like structure surrounding PS perforations. The PS perforation is generally hexagonally distributed in the PI layers.

I₃S-86-E: Sample I₃S-86-D further annealed at 140 °C for one week.

The PI mesh structure further changed during the annealing. A TEM Tilting series of this sample is shown in Figure 5.4. Figure 5.4a is a typical TEM micrograph of I₃S-86- E. It shows an irregular PI mesh structure. That indicates that the relative regular PI mesh structure in *I₃S-86-D* is partially broken during the annealing. However, after tilting the area in microscope along the tilt axis for 40 degrees, we still observe that all the dark material (PI) still occurs within a plane. The basic structure of alternating PI PS layers is still maintained, although the PI material in "PI layer" is a actually disordered mesh, perforated by PS material. This indicates the breakup of the PI mesh structure is still in plane.

I₃S-86-F: Sample I₃S-86-E further annealed at 160 °C for 3 days.

After annealing *I₃S-86-E* at 160 °C for 3 days, the PI mesh structures further break up. A TEM Tilting series of this sample is shown in Figure 5.5. Figure 5.5a is a typical TEM micrograph of I₃S-86-F. It shows that most polyisoprene material form disordered and worm-like structures. Some worms connect with each other. The interconnected disordered mesh network observed in *I₃S-86-F* further breaks up during the annealing at 160°C. Figure 5.5b is the TEM micrograph after we tile the area in Figure 5.5a along the indicated tilting axis for 30 degrees in microscope. It still shows the dark PI material occurs in lines in the image, which indicates that the worm-like

structure formed by the PI material is still in-plane. However, the transformation is not clear cut, TEM projections similar to that of I_3S-86-E are also observed in microscope.

I_3S-86-G: Sample I_3S-86-F further annealed at 180 °C for 3 days.

After annealing I_3S-86-E at 180 °C for 3 days, the material forms ordered cylinder morphology. A TEM micrograph of this sample is shown in Figure 5.6. This morphology is as same as the morphology of I_3S-86-A.

5.5   Discussion

In melt entangled state, the branched architecture slows down the dynamic of star-branched polymer dramatically.[128] In this experimental study, the slow kinetics of the high molecular weight non-linear polymer enable us to track the morphology transformations in detail. Agree with the previous study,[90] the sample I_3S-86 form cylinder morphology after casting from neutral solvent, and the morphology is stable during annealing, which indicates that cylinder morphology is the stable morphology for I_3S-86.

Casting from cyclohexane, a selective solvent for PI, I_3S-86-B forms regular lamella morphology. This morphology is kinetically trapped and is not stable when heated above T_g. During thermal annealing, the unstable lamella morphology goes though a series of changes towards its stable morphology. In Figure 5.7, we summarize the morphology transformations based on the TEM observations. First, PS perforated PI plane hexagonally, the perforation increase in size and the PI layers form mesh

139

structures. During further annealing at higher temperature, the mesh structures gradually break up, from the regular mesh structure first and then to irregular mesh structure and finally to disorder worms. All these transformations occur within the original lamella planes. After annealing at 180°C for 3 days, the material form ordered cylinder morphology, which is the same morphology as the toluene cast I₃S-86.

The experiment observation clearly demonstrated that perforated lamella is an intermediate stage during lamella to cylinder transformations. This observation is supplement to the previous results showing that perforated lamella is long-lived non-equilibrium morphology involved in lamella to Gyroid transition,[35,49] and is in agreement with the theoretical prediction of Qi and Wang.[57-59] However, the fact that perforated lamella occurs during the transitions from lamella to cylinder or from lamella to gyroid does not rule out that perforated lamella can be stable or meta-stable at certain compositions. As shown in a recent study of Yang, Gido and coworkers, perforated lamella was found simply by solvent casting of a blend sample, which consists of graft block copolymer and homopolymer, and was found stable during thermal annealing.

5.6   Conclusions

Morphology transition from cylinders to lamellae was studied via TEM. It was found that lamella morphology is not stable in the selective solvent cast I₃S-86, and it transforms into its thermodynamically stable lamellae on annealing. The transition turned out to occur though a series of in-plane transformations: perforated lamella, PI

140

mesh, and PI worms. This study shows that perforated lamella not only involves in the lamella to Gyroid transitions [35,37-39,46,49,50] but also in lamella to cylinder transitions.

Figure 5.1.   Illustration of the molecular architecture of an I_3S miktoarm star block copolymer.   The I_3S star is comprised of three PI arms and one PS arm joined at a single junction point.
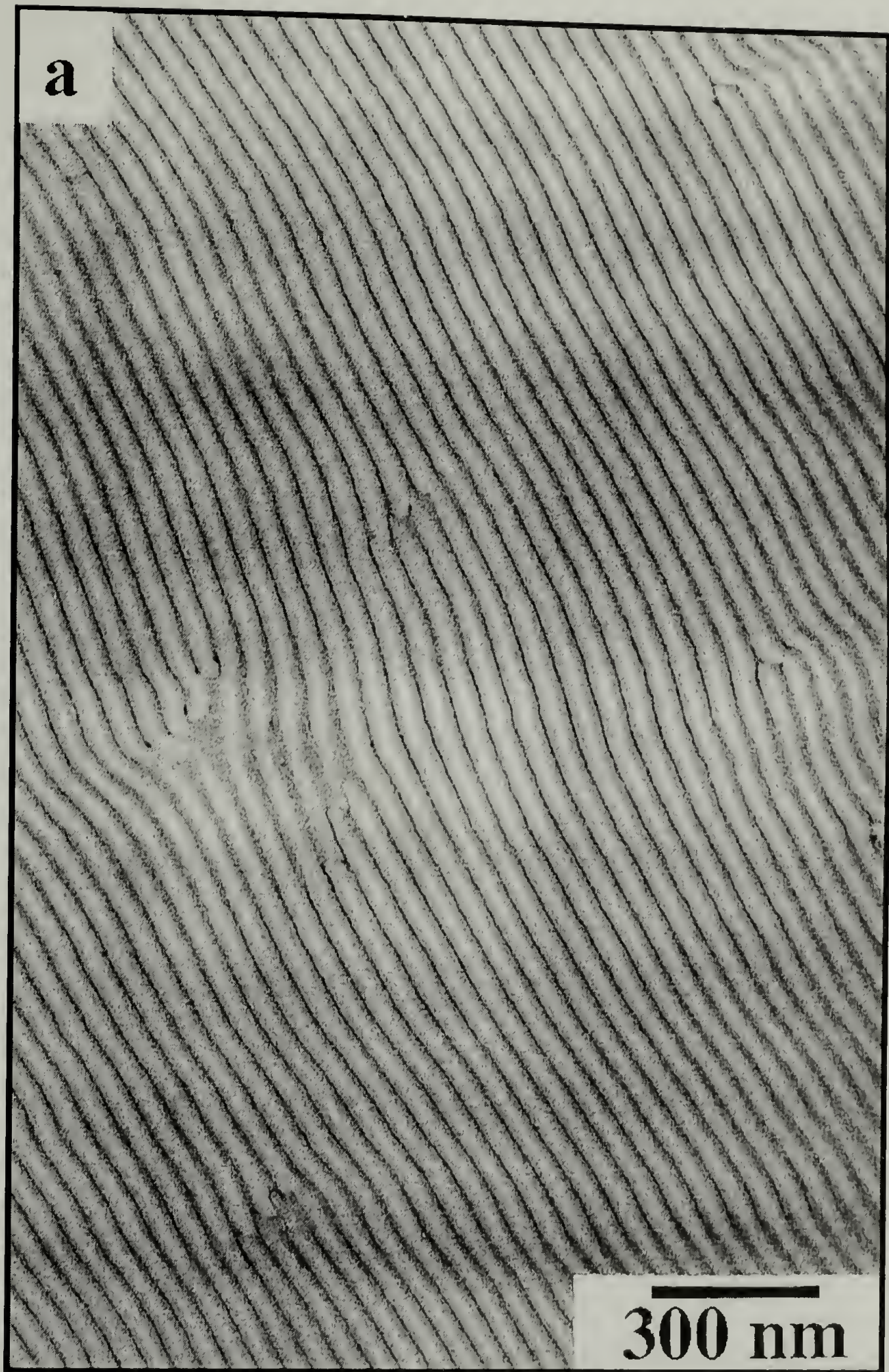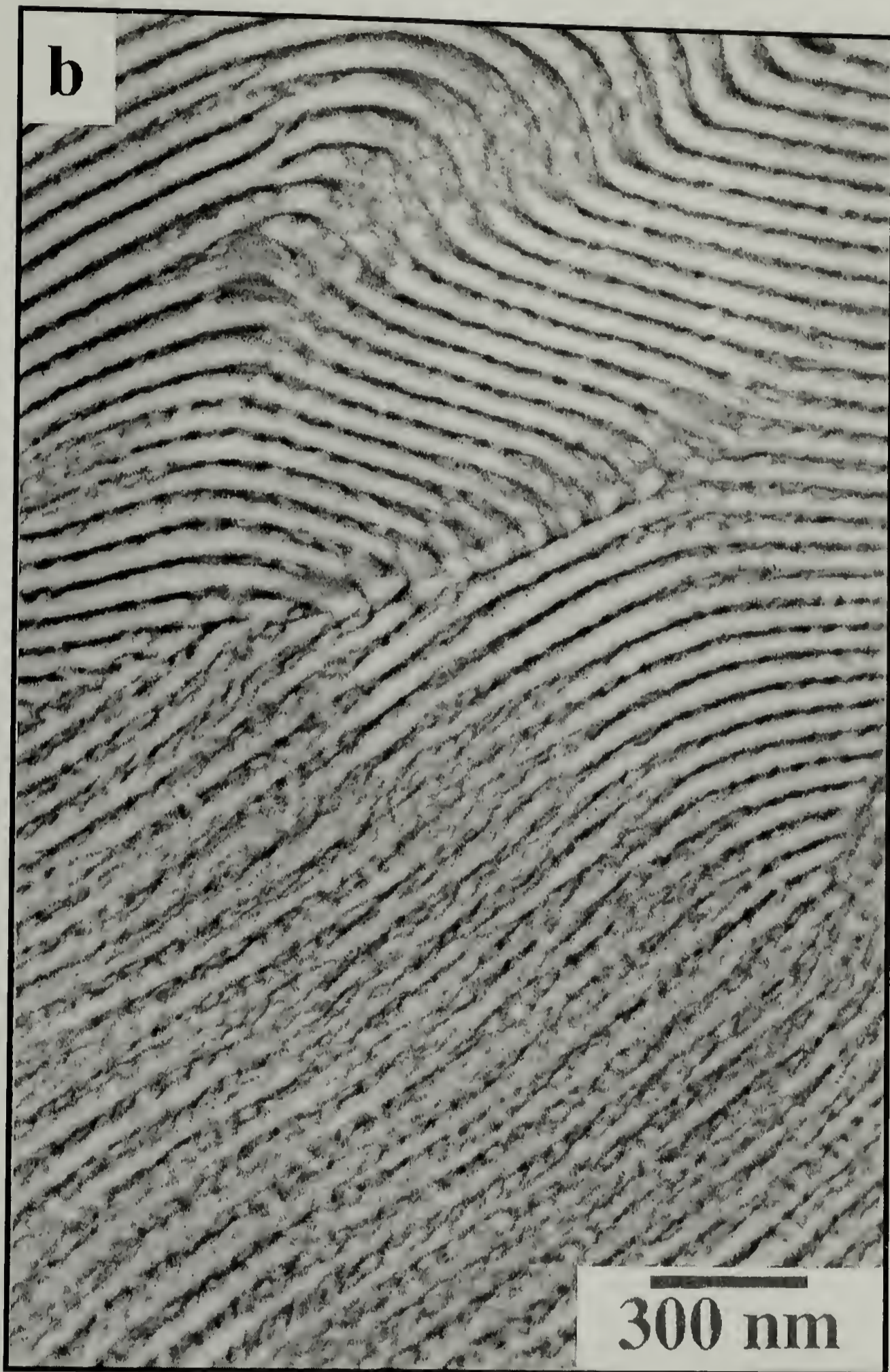
Figure 5.2. TEM micrographs of I₃S-86-B and I₃S-86-C: (a) I₃S-86-B; (b) I₃S-86-C.

144
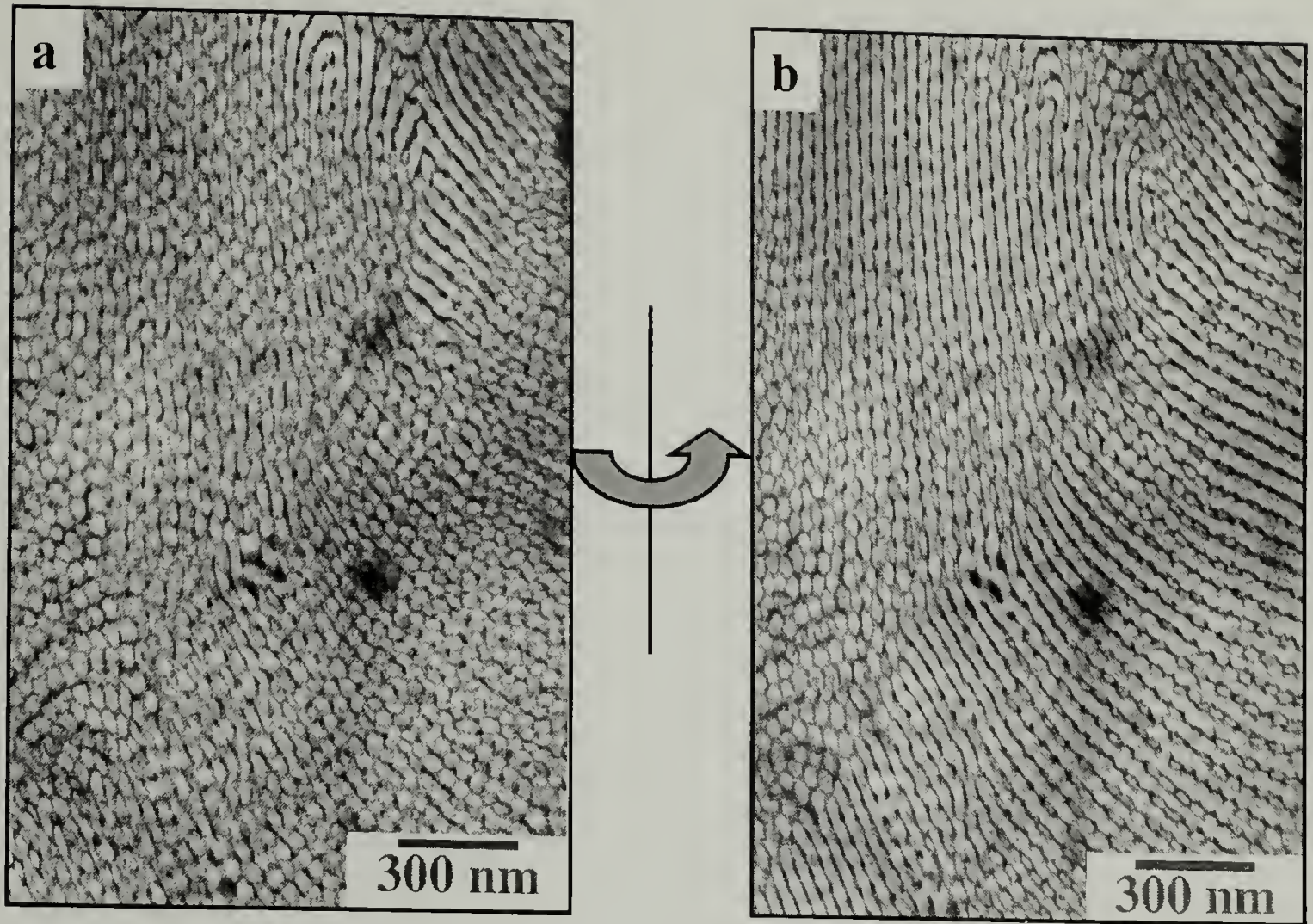
Figure 5.3.   TEM tilt series of I₃S-86-D (a) 0° tilt. (b) 20° tilt about axis indicated.
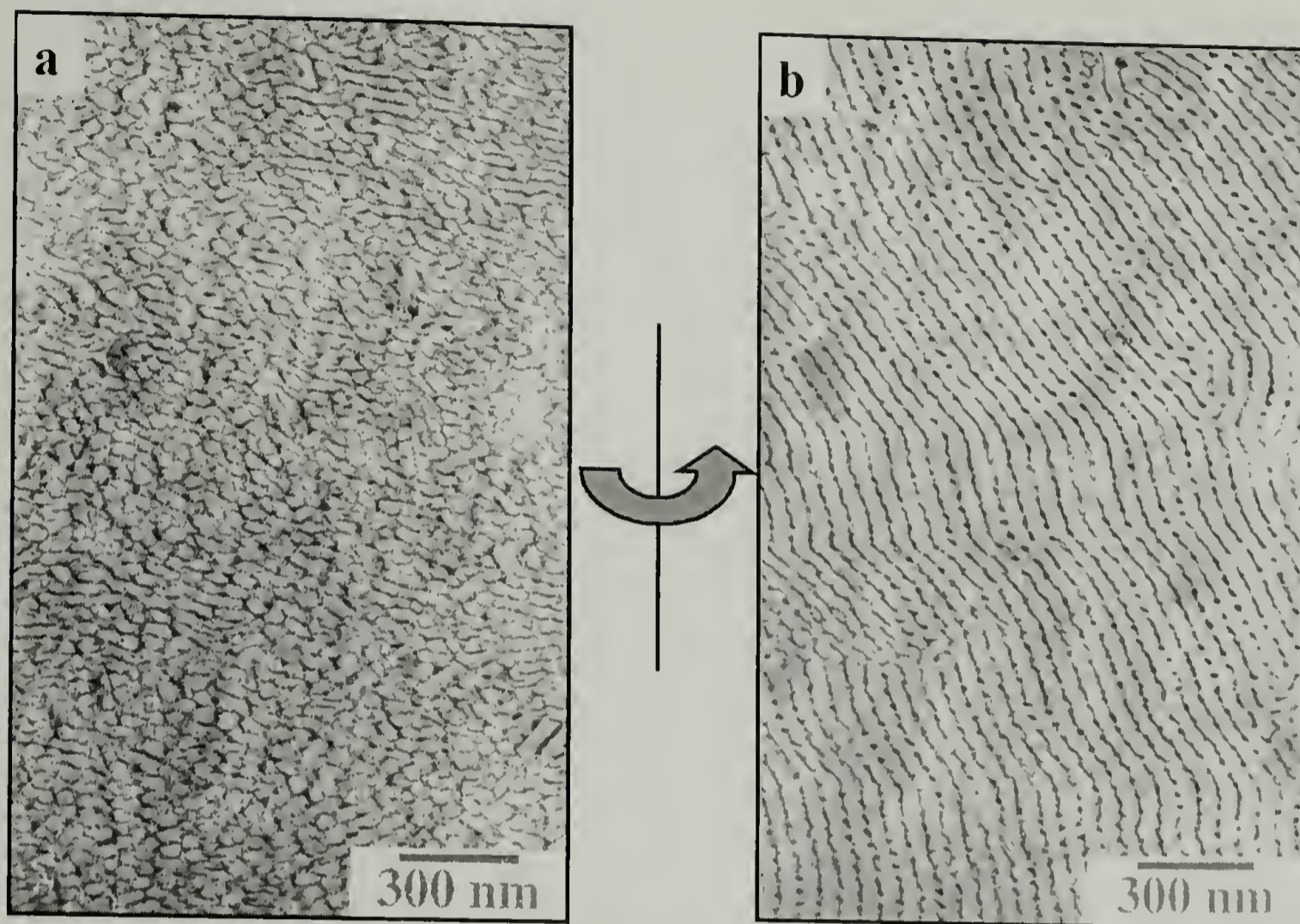
Figure 5.4.   TEM tilt series of I₃S-86-E. (a) 0° tilt.   (b) 40° tilt about axis indicated.
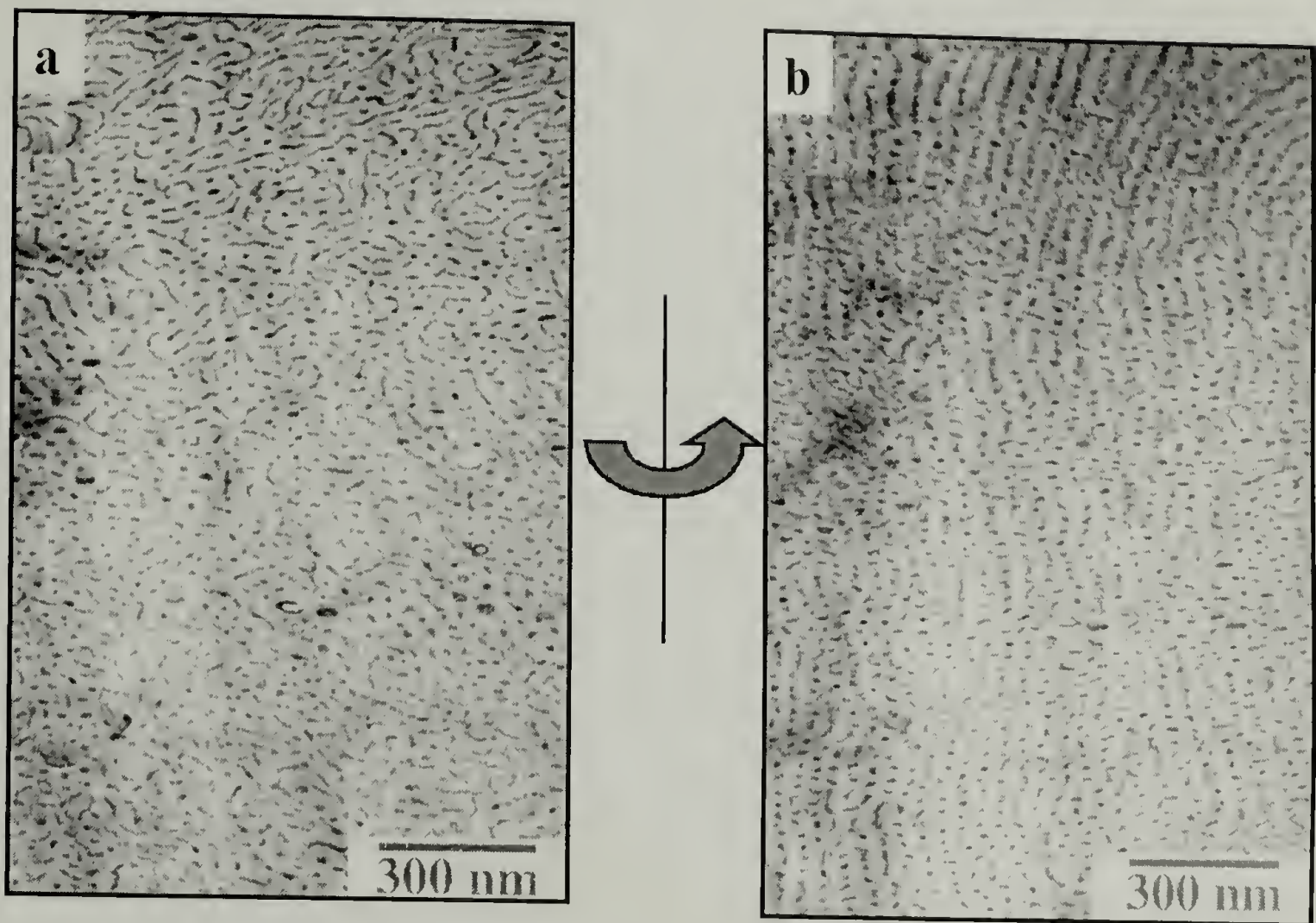
Figure 5.5.   TEM tilt series of I₃S-86-F. (a) 0° tilt.   (b) 30° tilt about axis indicated.
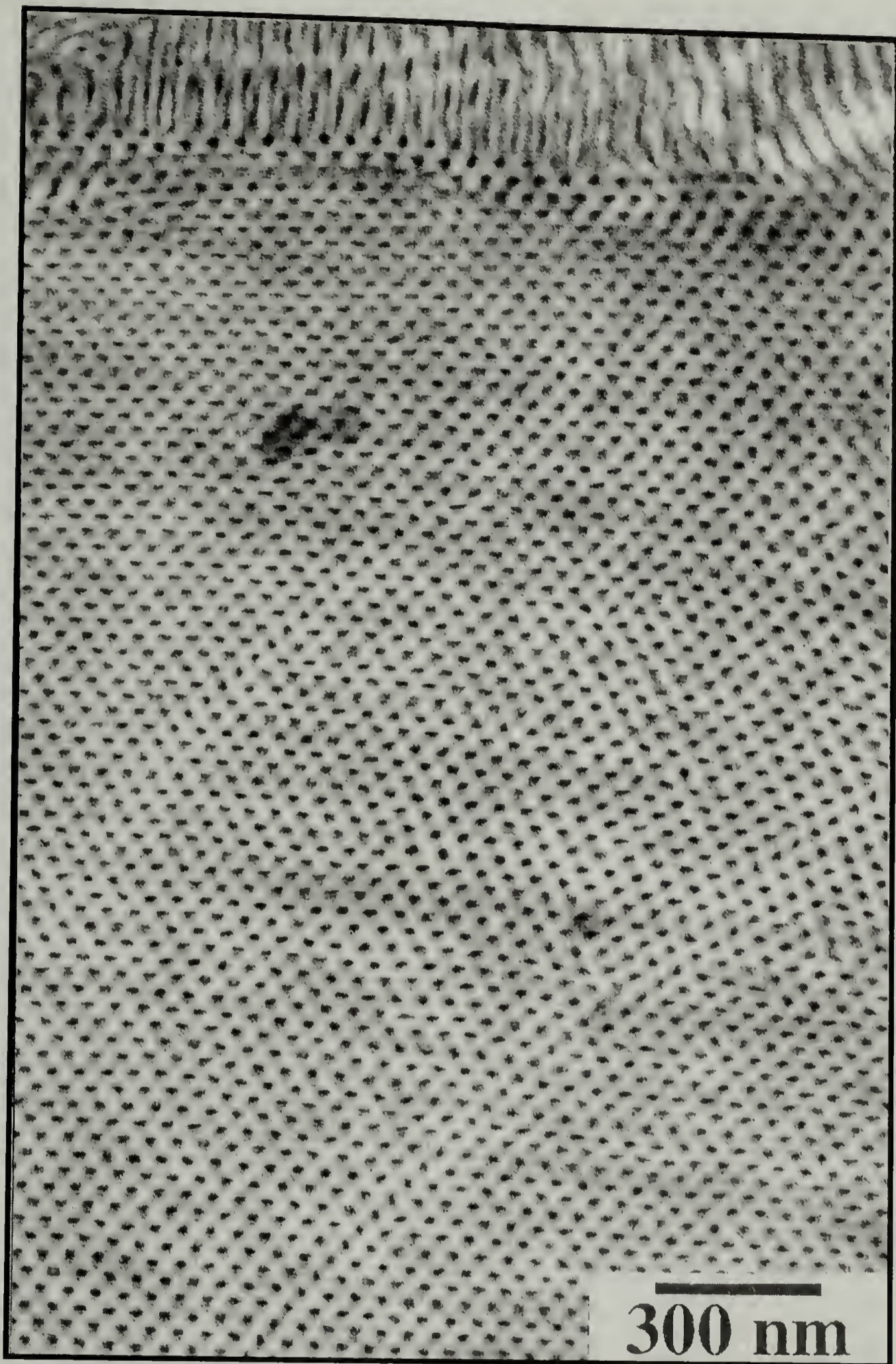
Figure 5.6.   TEM micrographs of I₃S-86-G.

148
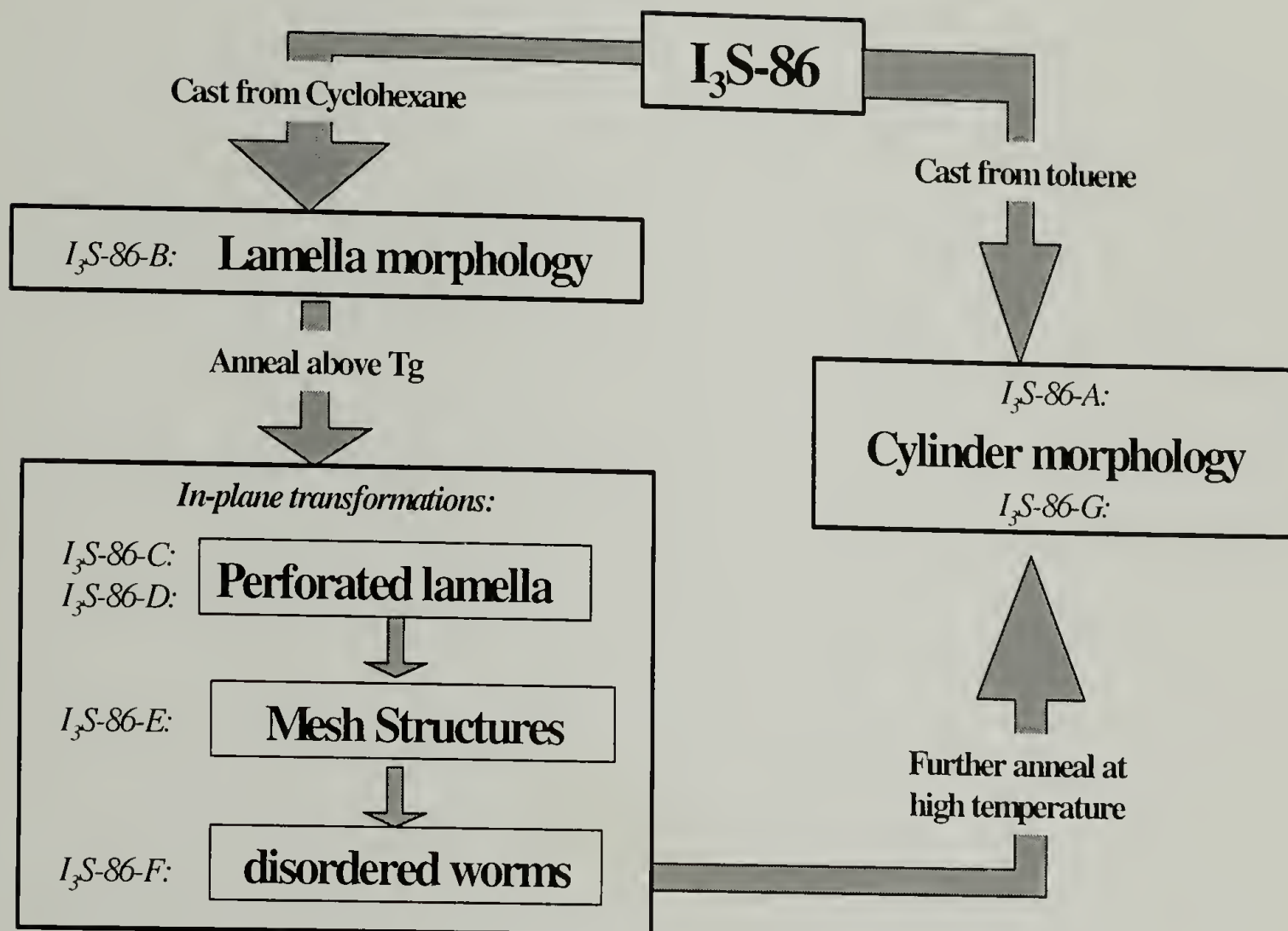
Figure 5.7.   Morphology transformation sequence schematic for the lamella to cylinder transformation of I₃S-86.

CHAPTER 6

CONCLUSIONS AND FUTURE WORK

6.1   The Milner Model and the broken tilt lamella grain boundaries.

Although the Milner model had been proven to be generally correct in its predictions for the morphological behavior of miktoarm stars with relatively low asymmetry parameters, two important points of contention had arisen by the start of this work. The first issue was what was the true morphology transformation volume fraction at high asymmetry parameter and how well it agreed with the Milner's model. The second issue that had arisen was what is the reason for the observed increase of discrepancies between the theoretically predicted miktoarm star block copolymer morphology and the experimental observation as the molecules become more asymmetric.

Our study in I_5S miktoarm stars indicated that the disagreement between the theoretically calculated morphology transition volume fraction and the experiment observed morphology transition volume fraction is very significant at high asymmetry parameter. Based on the data, we proposed that as architectural asymmetry (arm number asymmetry) becomes large, geometric packing constraints also exert an important influence on morphology. Milner's calculation was based on the assumption of a rounded Wigner-Seitz cell surrounding each domain.[11] In order for cylindrical and spherical domains to fill space, they must occupy true, space filling polyhedral Wigner-Seitz cells and deform to fill the corners of these cells.[83,119] Therefore, the

150

energies calculated with the rounded cell approximation (upon which Figure 4.5 is based) represent lower bounds. When the volume fraction of the component, which forms the core of the cylinder or sphere, is small (as in diblock copolymers), packing problems are not very important. However, as the molecule becomes more and more asymmetric, the volume fraction of the multi-arm component on the convex side of the interface may decrease to the point where it approaches the volume fraction of the interstitial space in a close packing of sphere. Thus we expect that geometric packing limits will prevent increasing shifts to higher ϕ of the true experimentally determined order-order transition lines in Figure 4.5 as ε becomes large. A similar geometric packing limit will also apply to the cylindrical morphology. At these limits the order-order transitions will become vertical lines on the morphology diagram. On Figure 4.5, we have sketched the approximate positions, based on experimental data, of geometrical packing limits for spherical and cylindrical morphologies.

In the lamella forming sample, I_5S-58, unusual chevron tilt grain boundary morphologies were observed, as shown in Figure 4.6. We postulate that the discontinuous nature of chevron tilt grain boundaries in I_5S-58 results from an asymmetry in the energy penalties for interfacial bending due to the asymmetry inherent in the I_5S molecular architecture. Due to crowding inherent in packing five arms of PI on the same side of the interface and the fact that curving the interface toward the PI side will exacerbate chain stretching resulting from this crowding, it may be energetically more costly to bend the interfaces toward the PI domains than toward the PS domains in an I_5S architecture. By replacing the standard cheveron structure with a broken or discontinuous structure as illustrated in Figure 4.9b, it is possible to achieve the required

151

tilt reorientation using only interfacial curvatures which put the five PI arms on the convex side of the interface. In order to do this, however, it is necessary to produce higher interfacial curvatures capable of generating semicylindrical end-caps on lamellae and isolated cylinders in the grain boundary plane.

6.1.1 Proposed Research

The results of these studies of miktoarm star morphological behavior lead to several interesting questions. First, regarding the effect of the geometric constriction, we sketched the approximate geometric limit position for sphere morphology based on the available experiment data. However, only six I_5S and six I_3S samples with lamella and cylinder morphologies have been examined. To get accurate value of the geometric limit for spheres, more I_5S and I_3S samples with lower PS volume fraction should be studied.

Another question concerning the geometric limits is the whether these I_3S and I_5S samples have reached these limit or they are just approaching these limit. To get accurate geometric limits for sphere and cylinder, a study of a series of much more asymmetric miktoarm star block copolymers molecules (I_nS nπ 5) should be performed.

A third interesting question which arises from this study is the defect structures resulted from the specific asymmetric molecular architecture. An analysis of these boundaries based on the bending energy of the asymmetric molecular architecture was given. From the observation in Microscope, the broken chevron structures are usually observed at relatively high tilt angles. However, quantitative analyses have not been

152

done. It will be interesting to further investigate the formation of discontinuous grain boundaries quantitatively in terms of tilt angle.

6.2 Investigation of morphology transformations using selective solvent approach.

Selective solvent can be used to control block copolymers' morphologies.[2,32,44,103] Thermal annealing of these kinetically trapped morphologies can provide us information about the path of transformations among these morphologies. This experimental study showed that the lamella to cylinder transition goes though a series of in-plane transformations: perforated lamella, PI mesh, and PI worms. These transformations indicate perforated lamella not only involves in the lamella to Gyroid transitions [35,37-39,46,49,50] but also in lamella to cylinder transitions.

6.2.1 Proposed research

As discussed in the 1st chapter, selective solvent approach provides many advantages and flexibilities in studying morphology transformations, which makes many interesting studies possible.

Due to the high MW of the polymer and resulting broad peak in SAXS, scattering method are not used. This study is based solely on microscopy evidence. Since TEM analysis only an limited portion of a sample, it is difficult to extract statistical results, like the dynamics of the transformation and its relation with MW, molecular architecture, temperature, etc, just from electron microscopy evidence.. Since scattering methods interact with a larger volume, they provide data with good statistical confidence.

153

However, to get high quality scattering date about the in plane transformation and out of plane transformations, it is important to get aligned unstable lamella morphology at the first step. Since the desired lamella morphology is a kinetically trapped, unstable morphology, the typical method, melt state shear alignment is not applicable. To achieve this purpose, a novel roll caster, as shown in Figure 6.1, has been designed and constructed. Roll caster was developed in Thomas group to solvent cast block copolymer into globally oriented morphology.[115,116] If we combine this idea with selective solvent, it is possible to cast block copolymer into unstable oriented morphologies. For our purpose, the designed roll caster has the following improvements over the reported roll casters.

1   The 4-pulley system design uses only one motor, which is compact and accurate in rotation speed control.

2   By rotating the wing-nut to adjust the distance between two cylinders, the thickness of the film can be controlled.

3   The curved bottom of the new design is material efficient, which is suitable for casting small amount of materials.

4   All Teflon construction makes it easy to retrieve the sample and to clean the instrument.

Using selective solvent, it is possible get kinetically trapped, yet globally oriented structures which facilitate the study irreversible morphology transformations.

Another interesting topic arise from this study is structure-property relationship. Previous study investigating the effects of morphology over properties was obtained by

extrapolations. Since many factors, like total molecular weight, molecular weight of the plastic block, molecular weight of the rubber block, volume fraction, annealing conditions, etc, all affect block copolymer properties, the extrapolations to relate morphology with properties are not accurate.. However, using selective solvent approach, we can obtain different morphologies with exactly same materials, thus we will be able to obtain precise information on morphology-properties relationship.

6.3   Morphology of Miktoarm star block copolymer / homopolymer blends.

Here, we use well-defined A_2B, A_2B_2 star shaped block copolymer, which are the structure units of more complex graft block copolymer systems,[3,4,6,31] as the model systems to study the effects of molecular architecture on graft block copolymer / homopolymer blends.   The first type, I_2S block copolymers, which have 2 low polydispersity (PDI) polyisoprene arms and one low PDI polystyrene arm joint at a single junction point, has an asymmetry, non-linear molecular architecture.[2,87]   Previously reported linear diblock copolymer / homopolymer blend systems showed that the order-order transitions (OOTs) occur at about the same volume fractions as in pure linear diblock copolymers.   The OOT occurs at the same volume fraction regardless of the direction from which it is approached, i.e. blending homopolymer A with a diblock which forms A cylinders in a B matrix to push it toward lamella or blending B homopolymer with a lamellar diblock to push it back toward cylinders.[17,18,20]   This study shows that when blending a homopolymer with an I_2S block copolymer that the OOTs split so that they occur at different volume fractions depending upon whether they are approached by blending homopolymer into the two arm or the one arm side of the block copolymer

155

interface. Perforated lamellar morphology is obtained in a blend of homopolystyrene (hPS) and a lamella forming single graft block copolymer, and it is found stable to thermal annealing.

The second type, I_2S_2 block copolymers, which have 2 low PDI polyisoprene arms and two low PDI polystyrene arms joint at a single junction point, has an symmetry, non-linear molecular architecture.[9] Although I_2S_2 block copolymers have symmetry molecular architecture, their blends with homopolymer also show strong shifts in the order-order transition volume fractions. Inverted phase is also observed in one of the blends with high homopolymer concentration. A slow co-casting procedure was developed to get single crystal structure of Gyroid morphology. The amazing scattering patterns provide the best evidence for Gyroid morphology observed so far.

6.3.1 Proposed Research

Using a slow casting procedure, one of the blends form amazingly ordered Gyroid structure. The scattering pattern proved the $Ia\bar{3}d$ symmetry of the structure. However, the inter-material dividing surface of Gyroid structure has not been well defined. The excellent SAXS data provides opportunities to illustrate the detail of the structure.

Another interesting question arising from the study is the relation between casting condition and long-range orders. As discussed above, though slow casting, a couple gyroid samples formed "single crystal" like long-range order. Perfect single crystals are usually observed in atom and molecular level self-assemblies with each consisting of materials perfectly the same. In nano-scale self-assemblies, the repeat unit usually

156

consists of hundreds to tens of thousands of atoms and the component molecules are not necessarily identical. Fluctuations and defects lead to imperfections and prevent the formation of large single crystal. All the cylinder or lamella blend samples are processed at the same conditions, but none of them have nearly the same degree of ordering as the Gyroid samples. This observation implies the defects structure in the inter-penetration network of Gyroid have relatively higher energies or kinetically easier to eliminate than that of lamella and cylinder morphologies. Achieving long-range order in nano-scale material is very important for many potential applications, like photonic material, nanoreactors, etc. A further study of the casting condition and the resulting long-range order or block copolymer and block copolymer / homopolymer blend systems will be very interesting.
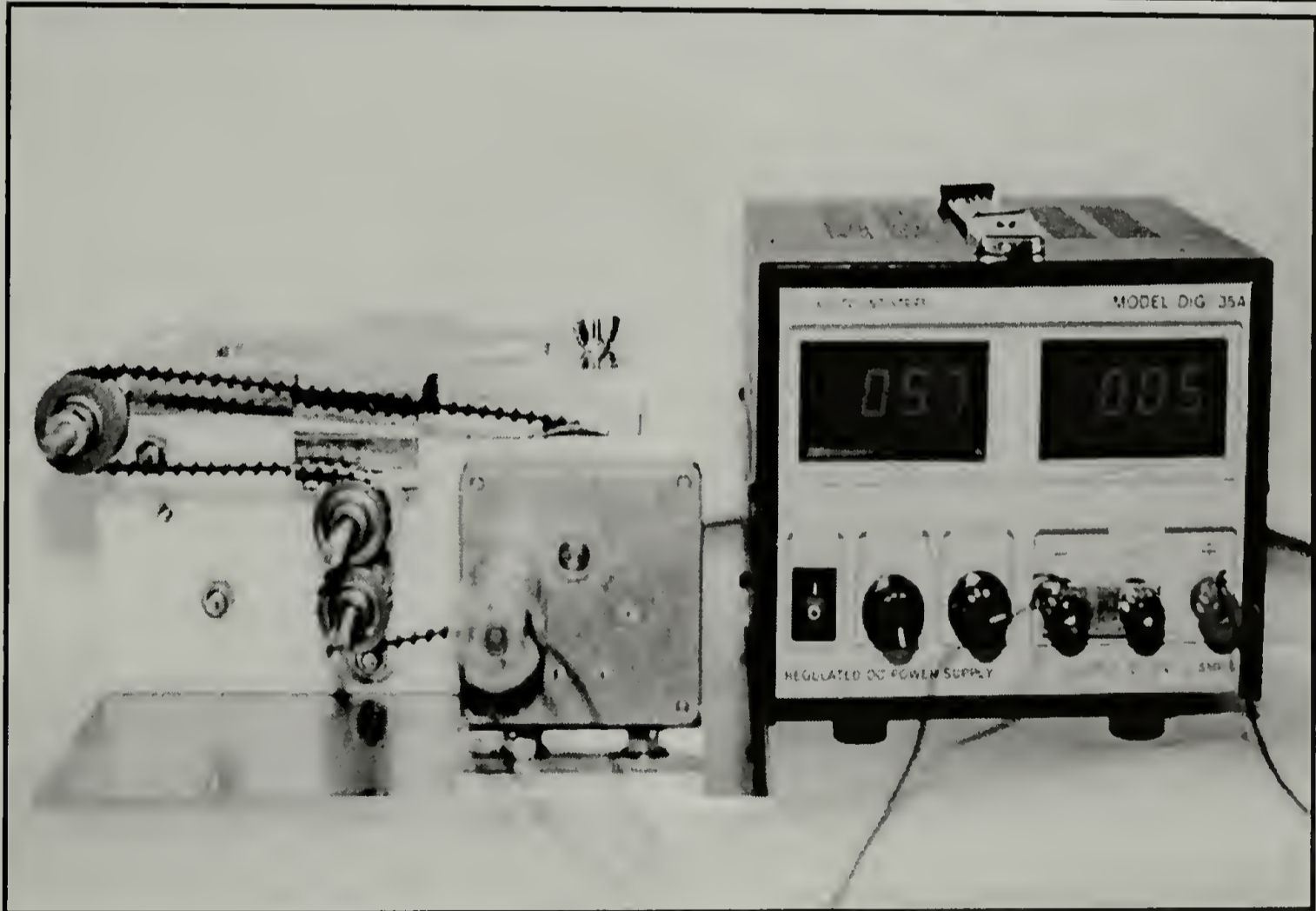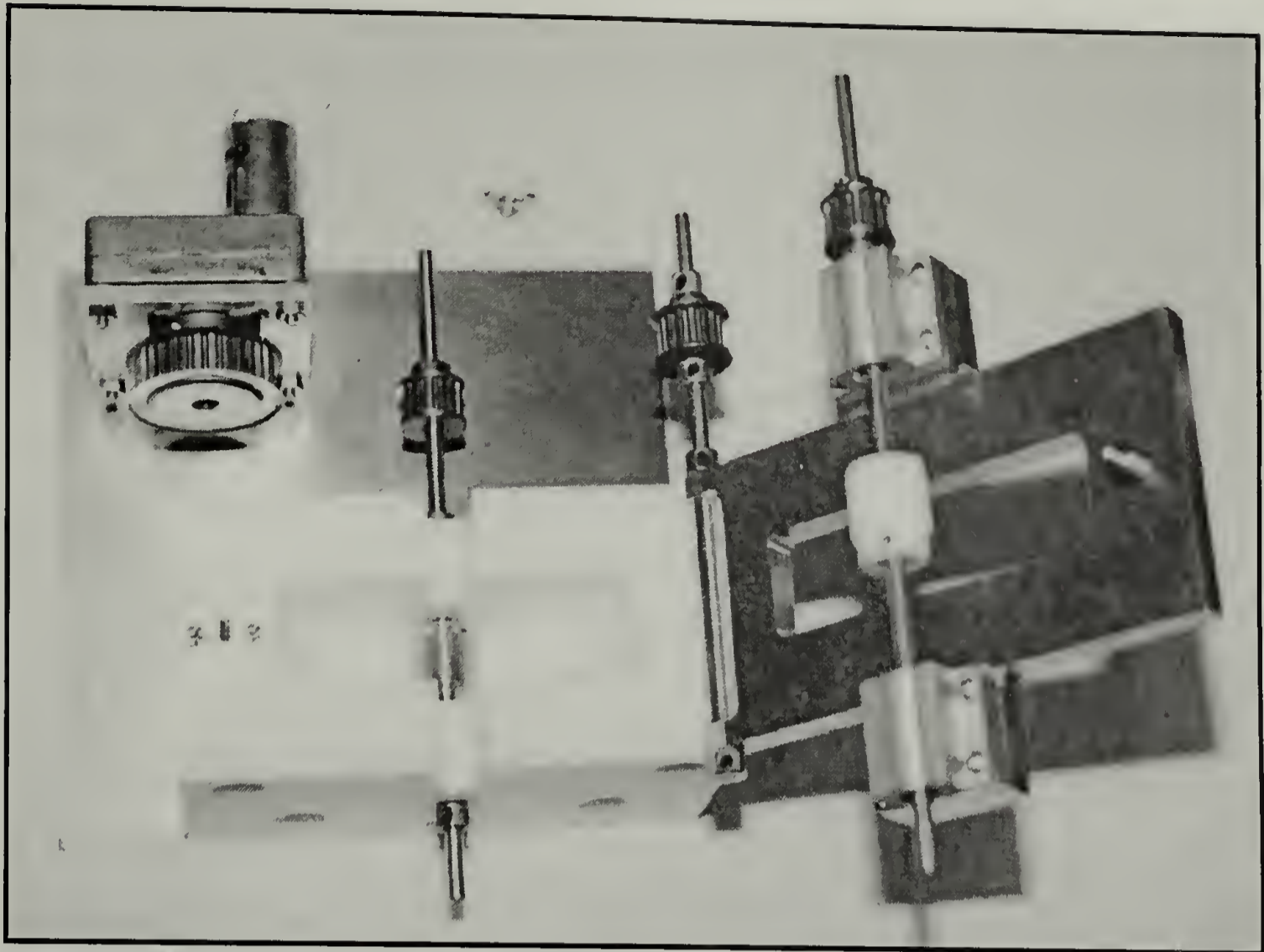
Figure 6.1.   Top view and side view of the "roll caster".

BIBLIOGRAPHY

1) Hadjichristidis, N.; Iatrou, H.; Behal, S. K.; Chludzinski, J. J.; Disko, M. M.; Garner, R. T.; Liang, K. S.; Lohse, D. J.; Milner, S. T. *Macromolecules* **1993**, *26*, 5812-5815.

2) Pochan, D. J.; Gido, S. P.; Pispas, S.; Mays, J. W. *Macromolecules* **1996**, *29*, 5099.

3) Lee, C.; Gido, S. P.; Poulos, Y.; Hadjichristidis, N.; Beck Tan, N.; Trevino, S. F.; Mays, J. W. *Journal of Chemical Physics* **1997**, *107*, 6460.

4) Lee, C.; Gido, S. P.; Poulos, Y.; Hadjichristidis, N.; Beck Tan, N.; Trevino, S. F.; Mays, J. W. *Polymer* **1997**, *39*, 4631-4638.

5) Lee, C.; Gido, S. P.; Pitsikalis, M.; Mays, J. W.; Beck Tan, N.; Trevino, S. F.; Hadjichristidis, N. *Macromolecules* **1997**, *30*, 3732-3738.

6) Lee, C. "The Morphological Behavior of Model Graft Copolymers," University of Massachusetts, 1998

7) Matsushita, Y.; Noda, I. *Macromolecular Symposia* **1996**, *106*, 251-257.

8) Beyer, F. L.; Gido, S. P.; Veils, G.; Hadjichristidis, N.; Tan, N. B. *Macromolecules* **1999**, *32*, 6604-6607.

9) Beyer, F. L.; Gido, S. P.; Uhrig, D.; Mays, J. W.; Tan, N. B.; Trevino, S. F. *Journal of Polymer Science* **1999**, *37*, 3392-3400.

10) Beyer, F. L.; Gido, S. P.; Poulos, Y.; Avgeropoulos, A.; Hadjichristidis, N. *Macromolecules* **1997**, *30*, 2373.

11) Milner, S. T. *Macromolecules* **1994**, *27*, 2333.

12) Tselikas, Y.; Hadjichristidis, N.; Lescanec, R. L.; Honeker, C. C.; Wohlgemuth, M.; Thomas, E. L. *Macromolecules* **1996**, *29*, 3390.

13) Koizumi, S.; Hasegawa, H.; Hashimoto, T. *Macromolecules* **1994**, *27*, 6532-6540.

14) Hashimoto, T.; Tanaka, H.; Hasegawa, H. *Macromolecules* **1990**, *23*, 4378-4386.

15) Tanaka, H.; Hasegawa, H.; Hashimoto, T. *Macromolecules* **1991**, *24*, 240.

16) Tanaka, H.; Hashimoto, T. *Macromolecules* **1991**, *24*, 5713.

17) Winey, K. I.; Thomas, E. L.; Fetters, L. J. *Macromolecules* **1992**, *25*, 2645.

18) Winey, K. I.; Thomas, E. L.; Fetters, L. J. *Journal of Chemical Physics* **1991**, *95*, 9367.

19) Winey, K. I.; Thomas, E. L.; Fetters, L. J. *Macromolecules* **1991**, *24*, 6128-6188.

20) Winey, K. I.; Thomas, E. L.; Fetters, L. J. *Macromolecules* **1992**, *25*, 422.

21) Bates, F. S.; Maurer, W.; Lodge, T. P.; Schulz, M. F.; Matsen, M. W. *Physical Review Letters* **1995**, *75*, 4429-4432.

22) Disko, M. M.; Liang, K. S.; Behal, S. K.; Roe, R. J.; Jeon, K. J. *Macromolecules* **1993**, *26*, 2983-2986.

23) Norman, D. A.; Kane, L.; White, S. A.; Smith, S. D.; Spontak, R. J. *Journal of Material Science Letters* **1998**, *17*, 545-549.

24) Laurer, J. H.; Hajduk, D. A.; Dreckotter, S.; Smith, S. D.; Spontak, R. J. *Macromolecules* **1998**, *31*, 7546-7549.

25) Lesance, R. L.; Fetters, L. J.; Thomas, E. L. *Macromolecules* **1998**, *31*, 1680-1685.

26) Braun, D.; Fischer, M.; Hellmann, G. P. *Polymer* **1996**, *37*, 3871.

27) Amorim, M. C. V.; Oliveira, C. M. F.; Tavares, M. I. B. *J. Appl. Polym. Sci.* **1996**, *61*, 2245.

28) Feng, H.; Tian, J.; Ye, C. *J. Appl. Polym. Sci.* **1996**, *61*, 2265.

29) Yanagase, A.; Ito, M.; Yamamoto, N.; Ishikawa, M. *J. Appl. Polym. Sci.* **1996**, *60*, 87.

30) Miyata, T.; Takagi, T.; Uragami, T. *Macromolecules* **1996**, *29*, 7787.

31) Beyer, F. L.; Gido, S. P.; Buschl, C.; Iatrou, H.; Uhrig, D.; Mays, J. W.; Chang, M. Y.; Garetz, B. A.; Balsara, N. P.; Beck Tan, N.; Hadjichristidis, N. *Macromolecules* **2000**, *33*, 2039-2048.

32) Sakurai, S.; Kawada, H.; Hashimoto, T.; Fetters, L. J. *Macromolecules* **1993**, *26*, 5796.

33) Sakurai, S.; Hashimoto, T.; Fetters, L. J. *Macromolecules* **1996**, *29*, 5769.

34) Hajduk, D. A.; Gruner, S. M.; Rangarajan, P.; Register, R. A.; Fetters, L. J.; Honeker, C.; Albalak, R. J.; Thomas, E. L. *Macromolecules* **1994**, *27*, 490.

35) Hajduk, D. A.; Ho, R.-M.; Hillimyer, M. A.; Bates, F. S.; Almdal, K. *J. Phys. Chem. B* **1998**, 1356-1363.

36) Hajduk, D. A.; Harper, P. E.; Gruner, S. M.; Honeker, C. C.; Thomas, E. L.; Fetters, L. J. *Macromoles* **1995**, *28*, 2570-2573.

37)Khandpur, A. K.; Forster, S.; Bates, F. S. *Macromolecules* **1995**, *28*, 8796-8806.

38)Förster, S.; Khandpur, A. K.; Zhao, J.; Bates, F. S.; Hamley, I. W.; Ryan, A. J.; Bras, W. *Macromolecules* **1994**, *27*, 6922.

39)Vigilid, M. E.; Almdal, K.; Mortensen, K.; Hamley, I. W.; Fairclough, J. P. A.; Ryan, A. J. *Macromolecules* **1998**, *31*, 5702-5716.

40)Almdal, K.; Koppi, K. A.; Bates, F. S.; Mortensen, K. *Macromolecules* **1992**, *25*, 1743-1751.

41)Atkins, P. W. *Physical Chemistry*; 5th ed.; W. H. Freeman and Company: New York, 1994.

42)Bates, F. S.; Fredrickson, G. H. In *Annual Review of Physical Chemistry*; Strauss, H. L., Babcock, G. T., Moore, C. B., Eds., 1990; Vol. 41, p 525.

43)Fredrickson, G. H.; Bates, F. S. *Annual Review of Materials Science Polymers* **1996**, *26*.

44)Thomas, E. L.; Alward, D. B.; Kinning, D. J.; Martin, D. C.; Handlin, D. L., Jr.; Fetters, L. J. *Macromolecules* **1986**, *19*, 2197.

45)Hasegawa, H.; Tanaka, H.; Yamasaki, K.; Hashimoto, T. *Macromolecules* **1987**, *20*, 1651.

46)Hajduk, D. A.; Harper, P. E.; Gruner, S. M.; Honeker, C. C.; Kim, G.; Thomas, E. L.; Fetters, L. J. *Macromolecules* **1994**, *27*, 4063.

47)Zhao, J.; Majumdar, B.; Schulz, M. F.; Bates, F. S.; Almdal, K.; Mortensen, K.; Hajduk, D. A.; Gruner, S. M. *Macromolecules* **1996**, *29*, 1204-1215.

48)Thomas, E. L.; Anderson, D. M.; Henkee, C. S.; Hoffman, D. *Nature* **1988**, *334*, 598-601.

49)Hajduk, D. A.; Takenouchi, H.; Hillmyer, M. A.; Bates, F. S.; Vigild, M. E.; Almdal, K. *Macromolecules* **1997**, *30*, 3788-3795.

50)Hamley, I. W.; Gehlsen, M. D.; Khandpur, A. K.; Koppi, K. A.; Rosedale, J. H.; Schulz, M. F.; Bates, F. S.; Almdal, K.; Mortensen, K. *J. Phys. 2 France* **1994**, *4*, 2161-2186.

51)Burger, C.; Micha, M. A.; Oestereich, S.; S.Forster; Antonietti, M. *Europhysics letters* **1998**, *42*, 425-429.

52)Ahn, J.-H.; Zin, W.-C. *Macromolecules* **2000**, *33*, 641-644.

53)Hashimoto, T.; Koizumi, S.; Hasegawa, H.; Izumitani, T.; Hyde, S. T. *Macromolecules* **1992**, *25*, 1443-1439.

54) Yang, L.; Gido, S. P.; Mays, J. W.; Pispas, S.; Hadjichristidis, N. *Macromolecules* **2001**, *34*, 4235-4243.

55) Semenov, A. N. *Soviet Physics JETP* **1985**, *61*, 733.

56) Fredrickson, G. H. *Macromolecules* **1991**, *24*, 3456.

57) Qi, S.; Wang, Z.-G. *Physical review letters* **1996**, *76*, 1679-1682.

58) Qi, S.; Wang, Z.-G. *Physical Review E* **1997**, *55*, 1682-1697.

59) Qi, S.; Wang, Z.-G. *Macromolecules* **1997**, *30*, 4491-4497.

60) Matsen, M. W.; Bates, F. S. *Macromolecules* **1996**, *29*, 1091.

61) Young, R. J.; Lovell, P. A. *Introduction to Polymers*; 2nd ed.; Chapman & Hall: New York, 1991.

62) Helfand, E.; Tagami, Y. *Journal of Chemical Physics* **1972**, *57*, 1812-1813.

63) Helfand, E.; Tagami, Y. *Journal of Chemical Physics* **1972**, *56*, 3592-3601.

64) Helfand, E. *Journal of Chemical Physics* **1975**, *62*, 999-1005.

65) Helfand, E. *Macromolecules* **1975**, *8*, 552-556.

66) Helfand, E. *Accounts of Chemical Research* **1975**, *8*, 295-299.

67) Helfand, E. *Journal of Chemical Physics* **1975**, *63*, 2192-2198.

68) Helfand, E.; Sapse, A. M. *Journal of Chemical Physics* **1975**, *62*, 1327-1331.

69) Helfand, E.; Wasserman, Z. R. *Macromolecules* **1976**, *9*, 879.

70) Helfand, E.; Wasserman, Z. R. *Polymer Engineering and Science* **1977**, *17*, 582.

71) Helfand, E.; Wasserman, Z. R. *Macromolecules* **1978**, *11*, 960-966.

72) Helfand, E.; Wasserman, Z. R. *Macromolecules* **1980**, *13*, 994-998.

73) Leibler, L. *Macromolecules* **1980**, *13*, 1602.

74) Schulz, M. F.; Bates, F. S.; Almdal, K.; Mortensen, K. *Physical Review Letters* **1994**, *73*, 86-89.

75) Milner, S. T.; Witten, T. A. *Journal de Physique* **1988**, *49*, 1951.

76) Milner, S. T.; Witten, T. A.; Cates, M. E. *Macromolecules* **1988**, *21*, 2610.

77) Milner, S. T.; Witten, T. A.; Cates, M. E. *Europhysics Letters* **1988**, *5*, 413-418.

78) Milner, S. T.; Wang, Z. G.; Witten, T. A. *Macromolecules* **1989**, *22*, 489.

79) Milner, S. T.; Witten, T. A.; Cates, M. E. *Macromolecules* **1989**, *22*, 853.

80) Milner, S. T. *J. Chem. Soc. Faraday Trans.* **1990**, *86*, 1349-1353.

81) Milner, S. T. *Science* **1991**, *251*, 905.

82) Milner, S. T. *Journal of Polymer Science: Part B: Polymer Physics* **1994**, *32*, 2743-2755.

83) Olmsted, P. D.; Milner, S. T. *Macromolecules* **1998**, *31*, 4011-4022.

84) Olmsted, P. D.; Milner, S. T. *Physical Review Letters* **1994**, *72*, 936.

85) Matsen, M. W.; Bates, F. S. *Macromoles* **1996**, *29*, 7641-7644.

86) Matsen, M. W.; Bates, F. S. *Journal of Polymer Science Pt. B: Polymer Physics* **1997**, *35*, 945-952.

87) Pochan, D. J.; Gido, S. P.; Pispas, S.; Mays, J. W.; Ryan, A. J.; Fairclough, J. P. A.; Hamley, I. W.; Terrill, N. J. *Macromolecules* **1996**, *29*, 5091-5098.

88) Pochan, D. J.; Gido, S. P.; Zhou, J.; Mays, J. W.; Whitmore, M.; Ryan, A. J. *Journal of Polymer Science, Polymer Physics* **1997**, *35*, 2629-2643.

89) Gido, S. P.; Lee, C.; Pochan, D. J.; Pispas, S.; Mays, J. W.; Hadjichristidis, N. *Macromolecules* **1996**, *29*, 7022.

90) Tselikas, Y.; Iatrou, H.; Hadjichristidis, N.; Liang, K. S.; Mohanty, K.; Lohse, D. J. *J. Chem. Phys.* **1996**, *105*, 2456.

91) Shull, K. R.; Winey, K. I. *Macromolecules* **1992**, *25*, 2637.

92) Laverdure, K.; Gido, S. P.; Pispas, S.; Mays, J. W. *In preparation.*

93) Oster, G.; Riley, D. P. *Acta Crystyllographica* **1952**, *5*, 272-276.

94) Oster, G.; Riley, D. P. *Acta Crystallographica* **1952**, *5*, 1-6.

95) Matsen, M. W. *Macromolecules* **1995**, *28*, 5765-5773.

96) Zhu, Y.; Gido, S. P. *In preparation.*

97) Kinning, D. J.; Winey, K. I.; Thomas, E. L. *Macromolecules* **1988**, *21*, 3502-3506.

98) Bates, F. S.; Berney, C. V.; Cohen, R. E. *Macromolecules* **1983**, *16*, 1101.

99)Alward, D. B.; Kinning, D. J.; Thomas, E. L. *macromolecules* **1986**, *19*, 215-224.

100)Herman, D. S.; Kinning, D. J.; Thomas, E. L.; Fetters, L. J. *Macromolecules* **1987**, *20*, 2940-2942.

101)Iatrou, H.; Hadjichristidis, N. *Macromolecules* **1993**, *26*, 2479-2484.

102)Yang, L.; Hong, S.; Gido, S. P.; Veils, G.; Hadjichristidis, N. *in press* *Macromolecules* **2001**.

103)Hanley, K. J.; Lodge, T. P.; Huang, C.-I. *Macromolecules* **2000**, *33*, 5918-5931.

104)Crystallography, I. U. o. *Internation Tables For X-Ray Crystallography*; 2nd Edition ed.; Birmingham, Eng.:, 1965.

105)Turner, C. M.; Sheller, N. B.; Foster, M. D.; Lee, B.; Corona-Galvin, S.; Quirk, R. P.; Annis, B.; Lin, J.-S. *Macromolecules* **1998**, *31*, 4372-4375.

106)Lee, C.; Gido, S. P.; Poulos, Y.; Hadjichristidis, N.; Beck Tan, N.; Trevino, S. F.; Mays, J. W. *Polymer* **1998**, *39*, 4631-4638.

107)Xenidou, M.; Beyer, F. L.; Gido, S. P.; Hadjichristidis, N.; Beck Tan, N. *Macromolecules* **1998**, *31*, 7659-7667.

108)Gehlsen, M. D.; Bates, F. S. *Macromolecules* **1994**, *27*, 3611.

109)Lin, C. C.; Jonnalagadda, S. V.; Kesani, P. K.; Dai, H. J.; Balsara, N. P. *Macromolecules* **1994**, *27*, 7769-7780.

110)Velis, G.; Hadjichristidis, N. *Macromolecules* **1999**, *32*, 534-536.

111)*Polymer Handbook*; 3rd ed.; Wiley-Interscience: New York, 1989.

112)Cowie, J. M. G. In *Developments in Block Copolymers - 1*; Goodman, I., Ed.; Applied Science Publishers: New York, 1982; pp 1-38.

113)Keller, A.; Odell, J. A. *Processing, Structure and Properties of Block Copolymer*; Elsevier Applied Science: New York, 1985.

114)Hadziioannou, G.; Mathis, A.; Skoulios, A. *Colloid and Polymer Science* **1979**, *257*, 22.

115)Albalak, R. J.; Thomas, E. L. *Journal of Polymer Science, Polym. Phys. Ed.* **1993**, *31*, 37.

116)Albalak, R. J.; Thomas, E. L. *Journal of Polymer Science, Polym. Phys. Ed.* **1994**, *32*, 341.

117)Grayer, V.; Dormidontova, E. E.; Hadziioannou, G.; Tsitsilianis, C. *Macromolecules* **2000**, *33*, 6330-6339.

118)Matsen, M. W.; Gardiner, J. M. *J. Chem. Phys* **2000**, *113*, 1673-1676.

119)Gido, S. P.; Schwark, D. W.; Thomas, E. L.; Goncalves, M. *Macromolecules* **1993**, *26*, 2636.

120)Gido, S. P.; Thomas, E. L. *Macromolecules* **1994**, *27*, 6137.

121)Polis, D. L.; Winey, K. I. *Macromolecules* **1996**, *29*, 8180-8187.

122)Polis, D. L.; Winey, K. I. *Macromolecules* **1998**, *31*, 3617-3625.

123)Qiao, L.; Winey, K. I. *Macromolecules* **2000**, *33*, 851-856.

124)Matsen, M. W. *J. Chem. Phys.* **1997**, *107*, 8110-8119.

125)Netz, R. R.; Andelman, D.; Schick, M. *Phys. Rev. Lett.* **1997**, *79*, 1058-1061.

126)Burgaz, E.; P.Gido, S. *Macromolecules* **2000**, *33*, 8739-8745.

127)Yang, L.; Hong, S.; Gido, S. P.; Uhrig, D.; Mays, J. W. *Submitted to Macromolecules* **2001**.

128)McLeish, T. C. B.; Milner, S. T. *Advances in Polymer Science* **1999**, *143*, 195-256.